
***Ab initio* based study of
magneto-chemo-structural coupling in
complex alloys**

Der Fakultät für Physik der
Universität Duisburg-Essen
vorgelegte Dissertation zum Erwerb eines
Doktors für Naturwissenschaften

von

Omkar Gopalkrishna Hegde

aus

Honnavar, India

Gutachter: Prof. Dr. Jörg Neugebauer
Gutachterin: Prof. Dr. Rossitza Pentcheva
Prüfer: PD Dr. Markus Gruner
Vorsitzender: Prof. Dr. Michael Farle

Tag der Disputation: 02 February 2022

DuEPublico

Duisburg-Essen Publications online

UNIVERSITÄT
DUISBURG
ESSEN

Offen im Denken

ub | universitäts
bibliothek

Diese Dissertation wird via DuEPublico, dem Dokumenten- und Publikationsserver der Universität Duisburg-Essen, zur Verfügung gestellt und liegt auch als Print-Version vor.

DOI: 10.17185/duepublico/75411

URN: urn:nbn:de:hbz:465-20220223-122411-1

Alle Rechte vorbehalten.

Abstract

Lattice imperfections (or defects) are ubiquitous in materials. Understanding the properties of various defects is crucial to improve materials' performance. In magnetic materials, as it is shown in this work, complicated interactions between the structural aspects of defects and magnetism are present. While comprehending these interactions at the atomic scale is highly relevant, the theoretical treatment of high-temperature paramagnetic (magnetically disordered) states, in particular, poses serious challenges. In the present thesis, a new, efficient first-principles method is introduced for the accurate computation of atomic relaxations in magnetically disordered systems with defects. The method is based on the spin-space averaging technique, and is general by construction, i.e., it is applicable to any magnetically disordered system with defects.

Firstly, the strength of the method is benchmarked for the vacancy defect in body-centered cubic (bcc) Fe by computing vacancy formation and migration energies. The impact of proper atomic relaxations is found to be significant and is compared with other approximate schemes, followed by a discussion on the influence of thermal expansion.

In the following stage, the relaxation method is applied to address vacancy-mediated diffusion in the dilute FeMn system, which is decisive for steels' performance. Mn is found to diffuse very fast relative to Fe in the ferromagnetic state and much slower in the paramagnetic state. The presence of Mn is shown to reduce the acceleration of diffusion coefficients across the magnetic order-disorder transition. These findings are linked to the strong impact of disordering on chemical interactions.

Further, the remarkable impact of magnetic states on the Mn segregation behavior at the grain boundaries is presented. A new phenomenon, where the grain boundary and bulk simultaneously exist in different magnetic states, is brought forward. Throughout the discussion, interplays of structure, chemistry and magnetism are identified. The effect of Mn segregation and vacancy formation on grain boundary decohesion is presented.

Finally, the discussions on the influence of structure, chemistry on magnetic properties are furthered by studying twin boundaries in MnAl permanent magnets. Magnetic domains undergo remarkable changes in the presence of twin boundaries, and the underlying mechanisms are linked to magnetocrystalline anisotropy energies and domain wall energies.

Zusammenfassung

Störungen der Kristallstruktur sind in Materialien allgegenwärtig. Das Verständnis der Eigenschaften verschiedener Defekte ist dabei entscheidend, um die Leistungsfähigkeit dieser Materialien zu verbessern. In magnetischen Materialien gibt es komplizierte Wechselwirkungen zwischen den strukturellen Aspekten von Defekten und dem Magnetismus. Während das Verständnis dieser Wechselwirkungen auf atomarer Ebene von großer Bedeutung ist, stellt insbesondere die theoretische Behandlung paramagnetischer (magnetisch ungeordneter) Hochtemperaturzustände eine große Herausforderung dar. In der vorliegenden Arbeit wird eine neue, effiziente First-Principles-Methode zur genauen Berechnung atomarer Relaxationen in magnetisch ungeordneten Systemen mit Defekten vorgestellt. Das Verfahren basiert auf der SSA-Technik (engl.: Spin-Space-Averaging) und ist von seiner Struktur her so allgemein, dass es auf jedes magnetisch ungeordnete System mit Defekten anwendbar ist.

Zunächst wird die Stärke der Methode für den Leerstellendefekt in kubisch-raumzentriertem (bcc) Fe durch Berechnung der Leerstellenbildung und der Migrationsenergien demonstriert. Der Einfluss der richtigen atomaren Relaxation ist signifikant und wird mit anderen Näherungsverfahren verglichen, gefolgt von einer Diskussion über den Einfluss der thermischen Ausdehnung.

Im folgenden Schritt wird die Relaxationsmethode angewendet, um die Leerstellengetriebene Diffusion im verdünnten FeMn-System zu behandeln, die für die Leistungsfähigkeit von Stählen entscheidend ist. Mn diffundiert relativ zu Fe im ferromagnetischen Zustand sehr schnell und im paramagnetischen Zustand viel langsamer. Es wird gezeigt, dass die Anwesenheit von Mn die Beschleunigung der Diffusionskoeffizienten beim Übergang von magnetischer Ordnung zu Unordnung reduziert. Diese Ergebnisse sind mit einem starken Einfluss von Unordnung auf chemische Wechselwirkungen verbunden.

Weiterhin wird der bemerkenswerte Einfluss magnetischer Zustände auf das Mn Segregationsverhalten an den Korngrenzen dargestellt. Ein neues Phänomen, bei dem Korngrenze und Volumen gleichzeitig in verschiedenen magnetischen Zuständen existieren, wird vorgestellt. Während der Diskussion werden Wechselwirkungen von Struktur, Chemie und Magnetismus identifiziert. Der Effekt der Mn-Segregation und der Leerstellenbildung auf die Dekohäsion der Korngrenzen wird dargestellt.

Schließlich werden die Diskussionen über den Einfluss von Struktur und Chemie auf magnetische Eigenschaften durch die Untersuchung von Zwillingsgrenzen in MnAl Permanentmagneten erweitert. Magnetische Domänen unterliegen bemerkenswerten Veränderungen bei der Anwesenheit von Zwillingsgrenzen, und die zugrundeliegenden Mechanismen sind mit magnetokristallinen Anisotropieenergien und Domänenwandenergien verbunden.

Contents

Abstract	iii
Zusammenfassung	iv
1 Introduction	1
2 Theoretical methods	7
2.1 Density-functional theory	7
2.1.1 Schrödinger equation and Born-Oppenheimer approximation	7
2.1.2 Electron density	9
2.1.3 Hohenberg-Kohn theorems	9
2.1.4 Kohn-Sham approach	11
2.1.5 Exchange-correlation functionals	11
2.1.6 Pseudopotentials and Projector-Augmented Wave method	13
2.1.7 Spin-polarized DFT	13
2.2 Magnetic disorder	14
2.2.1 Disordered Local Moments and Special Quasirandom Structures	15
2.2.2 Spin constraints	16
2.2.3 Atomic forces and Spin-Space Averaging	18
3 Atomic relaxation method for magnetically disordered materials with defects	21
3.1 Introduction	21
3.2 Generating random magnetic configurations	23
3.3 Protocol for SSA relaxation	24
3.4 Computational details	27
3.5 Results and Discussion	29
3.5.1 Impact of magnetic disorder	29
3.5.2 Impact of atomic relaxations	31
3.5.3 Inclusion of volume expansion	34
3.6 Conclusions	36

4	Impact of magnetism on diffusion of Mn in α-Fe bulk	39
4.1	Introduction	39
4.2	Diffusion coefficients	40
4.2.1	Ruch model	40
4.2.2	Ratio of diffusion coefficients	40
4.2.3	Mixing scheme for the ratio of diffusion coefficients	42
4.3	Computational details	43
4.3.1	DFT based calculations	43
4.3.2	Effective interaction model and tracer diffusion experiments	44
4.4	Results and discussions	44
4.4.1	Vacancy energies	45
4.4.2	Diffusion parameters	48
4.5	Conclusions	52
5	Interplay of structure, chemistry and magnetism at FeMn grain boundaries	55
5.1	Introduction	55
5.2	Computation of grain boundary energetics	56
5.3	Computational details	57
5.4	Results and discussion	59
5.4.1	Grain boundary formation energies	61
5.4.2	Mn segregation energies	64
5.4.3	Vacancy at the grain boundary	72
5.4.4	Grain boundary decohesion	73
5.5	Conclusions	77
6	Influence of twin boundaries on magnetic domains in τ-MnAl	79
6.1	Introduction	79
6.2	Computational and experimental details	80
6.2.1	First-principles calculations	80
6.2.2	Correlative APT-TEM studies	81
6.2.3	Off-axis electron holography	82
6.3	Results and discussion	83
6.3.1	Structural and chemical properties of MnAl twin boundaries	83
6.3.2	Magnetic domains and anisotropies	85
6.4	Conclusions	89
7	Summary and outlook	91

Bibliography	95
Acknowledgments	109
Erklärung	111

List of Figures

1-1	Elongation-tensile strength relation for different kinds of steels. The image is adopted from [1] and [2].	2
3-1	An example of a SQS structure for a $2 \times 2 \times 2$ bcc cell is shown. Note that the actual calculations employ a $3 \times 3 \times 3$ bcc cell.	24
3-2	Schematic picture with the algorithm for the SSA relaxation method. Various tools (Random magnetic configuration generator, DFT code with spin constraint tool, SSA scheme, External structural optimizer, and ART tool for migration barrier calculations) are combined and connected to build the final protocol [3].	25
3-3	Convergence of SSA forces for the first and second nearest-neighbour atoms of the vacancy. The ionic relaxation is stopped when the force on each atom is within $0.015 \text{ eV}/\text{\AA}$, which is marked by the orange dashed line.	28
3-4	Comparison of activation energies, which are the sums of formation energies (lower section of each bar) and migration energies (upper section of each bar), between physically realistic SSA relaxations and other relaxation considerations in the PM state in bcc Fe. Results are shown for the theoretical equilibrium lattice constant ($a = 2.83 \text{ \AA}$) and at a high-temperature lattice constant ($a = 2.87 \text{ \AA}$) close to the Curie temperature [3].	31
3-5	Displacements of nearest-neighbour atoms of the vacancy for different relaxation schemes for the PM state of bcc Fe are shown [3]. Atoms are represented according to local symmetry, and the displacements are linked to the corresponding atoms in the diagrams given in the inset. Blue bars show the displacement in the vacancy state and yellow, green, and orange bars depict the displacements in the transition state.	35
4-1	Migration energies for the $1NN$ jumps of the vacancy (dashed circle) in the vicinity of a solute atom (orange circle). $E_m^{(0)}$ is the self-diffusion migration barrier of the host atom and represents any jump that is not affected by the presence of the solute atom. Arrows represent the directions of atomic jump.	41

4-2	Vacancy formation energies in pure Fe and in the dilute case of Mn in Fe. The vacancy is positioned at $1NN$ distance from Mn in the dilute FeMn system.	45
4-3	Vacancy migration energies for the intermediate temperatures obtained by the Ruch interpolation for the $1NN$ jumps of the vacancy in FeMn [4].	46
4-4	Vacancy activation energies for pure Fe and Mn in Fe.	47
4-5	Self-diffusion coefficient in bcc Fe as a function of temperature, obtained from DFT-SSA. The experimental values from Iijima et al. [5] and Hettich et al. [6] are compared.	48
4-6	Diffusion coefficient of Mn in bcc Fe as a function of temperature, obtained from DFT-SSA, EIM-MC and experimental measurements [4]. EIM-MC are obtained by the collaborators from CEA Saclay and the experimental measurements are conducted by the collaborators from the University of Münster.	49
4-7	Comparison of the diffusion profiles for self-diffusion and Mn diffusion in α -Fe.	50
4-8	Ratio between the Mn diffusion coefficient in bcc Fe and the Fe self-diffusion coefficient [4]. The EIM-MC results are obtained by the collaborators from CEA Saclay and the experimental measurements are conducted by the collaborators from the University of Münster.	51
4-9	Kinetic correlation factors for Fe self-diffusion (f_0 : green line) and Mn diffusion (f_2 : blue lines) [4]. The f_2 kinetic correlation factor determined by considering only the barriers in the FM state is also displayed (orange lines) for comparison and to highlight the impact of magnetic disorder. The EIM-MC results are obtained by the collaborators from CEA Saclay.	52
5-1	$\Sigma 5[001](310)$ grain boundary with different sites labelled. A supercell with 80 atoms is used with an additional layer in the c -axis. Only one atom in each layer (along \mathbf{b} -axis) is labelled, since they are symmetrically equivalent to the other sites in the same layer for the given pure grain boundary.	58
5-2	Convergence of averaged grain boundary ($\Sigma 5[001](310)$) energy in the paramagnetic state with respect to the number of random magnetic configurations.	59
5-3	Magnetic moments of Fe and Mn in bcc Fe bulk and grain boundary, for the ferromagnetic and paramagnetic states. For the paramagnetic state, only the magnitudes of moments are considered.	60
5-4	Local density-of-states (DOS) of a Mn atom in the bulk and grain boundary, along with the DOS of its nearest neighbour Fe atom. The Fermi energy is shifted to 0 eV.	61
5-5	Grain boundary energies for pure Fe and Mn segregated Fe grain boundaries, in both the ferromagnetic and paramagnetic states.	62

5-6	Change in grain boundary energy with increasing magnetic disorder in the supercell, starting from the grain boundary layer until it covers the entire supercell.	63
5-7	Mn segregation energies with respect to different sites (labelled in Fig. 5-1) in the grain boundary supercell, for the ferromagnetic and paramagnetic states.	64
5-8	Effective magnetic interaction parameters at different sites (labelled in Fig. 5-1) in the grain boundary supercell, for the ferromagnetic Fe system. Segregation energies of AFM Fe atom is shown in the second y -axis.	65
5-9	Mn occupancies at different sites (labelled in Fig. 5-1) in the grain boundary supercell, calculated using the ferromagnetic and paramagnetic segregation energies assuming 10% Mn composition in the bulk.	66
5-10	Mn occupancies at different sites (labelled in Fig. 5-1) in the grain boundary supercell, calculated using the ferromagnetic and paramagnetic segregation energies for the same temperature (1050 K) assuming 10% Mn composition in the bulk.	67
5-11	Segregation energies for the second Mn atom when a Mn atom is located at the grain boundary layer (site 1 in Fig. 5-1), for the ferromagnetic and paramagnetic states.	68
5-12	Mean-field Curie temperatures as a function of Mn composition, for both the bulk and grain boundary systems.	70
5-13	Segregation energies and occupancies for the case with the grain boundary in the paramagnetic state and the bulk in the ferromagnetic state. The other two limits are also shown for comparison.	71
5-14	Vacancy formation energies at different grain boundary sites, for the ferromagnetic and paramagnetic states. Bulk values (dashed-dot lines) have been added for the reference.	72
5-15	Stress-strain curves obtained from first-principles tensile tests for pure Fe (green dashed line), Mn substituted at site 1 covering 25% of the grain boundary layer or layer 1 (blue dashed line), Mn at site 2 covering 25% of the layer next to the grain boundary layer (light blue dashed line) and when the entire grain boundary layer is covered by Mn (red dashed line).	74
5-16	Stress-strain curves for the Fe grain boundary with a vacancy in site 1 (black dashed line), site 2 (yellow dashed line). The case of pure Fe without any vacancy has been added for reference.	75

5-17	Stress-strain curve for Fe grain boundary with both Mn and vacancy in the second layer (violet dashed line), compared with the cases of a Mn atom in the second layer, Mn covering the entire grain boundary layer and vacancy in the second layer. Pure Fe case is also added for reference.	76
6-1	Schematic of the off-axis electron holography technique. The figure is generated by the experimental collaborators from FZ Jülich and is adapted from the collaborative work published in Phys. Rev. Materials 5, 064403 (2021) [7].	82
6-2	(a) BSE image of the microstructure, (b) BF- and DF-TEM images of the specimen, (c) BF-TEM image of the area considered for APT study and the APT profile revealing Mn segregation at the twin boundary. The figure is generated by the experimental collaborators from MPIE Düsseldorf and is adapted from the collaborative work published in Phys. Rev. Materials 5, 064403 (2021) [7].	83
6-3	Formation energy convex hull for the bulk and twin structures of τ -MnAl as a function of Mn composition.	84
6-4	Magnetic domain structure of τ -MnAl with higher and lower densities of microtwins. (a), (c), (e) are BF TEM images and (b), (d), (f) are the corresponding projected in-plane magnetic induction maps recorded using off-axis electron holography. The figure is generated by the experimental collaborators from FZ Jülich and is adapted from the collaborative work published in Phys. Rev. Materials 5, 064403 (2021) [7].	86
6-5	Schematic of the the bulk and twin supercells along with the domain walls considered for calculations.	87
6-6	Calculated DWEs and MAEs for the equal- and off-stoichiometric compositions, in both the bulk and twin regions.	88
7-1	Summary of defect types, keywords and schematic diagrams corresponding to each result chapter in the thesis.	93

List of Tables

3-1	Comparison of energy differences (ΔE) and lattice parameters (a (Å)) for the bulk ferromagnetic (FM) and PM states. Different SQSs that are generated by considering different correlation functions are compared for the PM state. ΔE is the energy difference with respect to the FM ground-state at 0 K. $3 \times 3 \times 3$ supercells are considered for the calculations.	24
3-2	First-principles values of activation energy E_a for self-diffusion, the vacancy formation energy E_f and the migration barrier E_m for nearest neighbour vacancy jumps [3] in bcc Fe. For the PM state, energies obtained from different relaxation schemes are compared. The values are presented for the theoretical equilibrium lattice constant $a = 2.83$ Å, if not indicated differently.	30
4-1	The calculated migration energies for the exchanges of the vacancy with nearest neighbour atoms in both the FM and PM states in pure Fe and dilute FeMn system. $E_m^{(0)}$ is the migration barrier for the jump in pure Fe (or any Fe jump that is unaffected by the presence of Mn). $E_m^{(2)}$ is the migration barrier for the Mn jump. $E_m^{(3)}$ and $E_m^{(4)}$ represent the Fe jumps that dissociate and associate Mn-vacancy pair, respectively (Fig. 4-1).	46
5-1	Experimental grain boundary energies (in J/m ²) estimated by Geise et al [8] from the diffusion data in α -Fe, using a semi-empirical approach of Borisov et al. [9].	63
6-1	Calculated anisotropy energies between different axes in the bulk and twin supercells.	87

1 Introduction

Simply put, materials physics involves a thorough understanding of the physical properties of materials at its core. The numerous possibilities for improving materials properties and designing novel materials that arise through materials physics have made the field highly relevant and ever so fascinating. Steels are exemplary structural materials to demonstrate this: known for their strength, durability, recyclability, and low cost, steels have become an integral part of human life. Understandably, this has led to a constant yearning for improved physical properties in steels. However, the incredible complexities of structural, chemical, and magnetic degrees of freedom that prevail in steels serve as bottlenecks to achieve such improvements. On the other hand, the same complexities have captivated physicists and engineers alike [2, 1]. Understanding these phenomena is crucial to ultimately engineer steels with advanced properties, such as the example shown in Fig. 1-1 (adopted from [1] and [2]). As presented in the figure, while the ferritic steels exhibit excellent elongations prior to fracture, they have low ultimate tensile strength, whereas the situation is opposite in the case of martensitic steels. Therefore, the design of advanced steels with transition/twinning induced plasticity (TRIP/TWIP) that show high elongation while maintaining high tensile strength, is of great interest. In order to achieve this, various complex events need to be comprehended at the atomic scale. Of many phenomena that need to be subjected to careful studies in steels, the emergence of a variety of defects, their competition, solute segregation to defects, diffusion, fracture, are some of the important examples. Moreover, thermal treatments during the engineering introduce different magnetic states in these materials, such as the low-temperature ferromagnetic state and high-temperature paramagnetic state, which demand proper considerations. Thus, it is necessary to take the interplay of aforementioned phenomena and magnetism into account, and this forms the crux of the thesis.

Theoretical modelling of the paramagnetic state involves the challenging task of treating complicated interactions of disordered magnetic moments. As such, it is a relatively young field compared to that of chemical disorder [10]. Nevertheless, significant progress has been achieved in treating the magnetic disorder in perfect bulk systems. We discuss some important methods and their relevance with respect to this in chapter 2. The presence of defects brings about additional complications due to their structural complexities, and the

theoretical modelling in this regard is limited in the literature. In particular, the deviations from the bulk ordering that arise due to defects result in atomic relaxations. To capture the atomic relaxations, an accurate computation of the atomic forces is necessary. Among the state-of-the-art methods, density functional theory (DFT) is the most feasible tool to achieve this. The limited number of works available in the literature that deal with defects in the paramagnetic state make severe assumptions regarding atomic relaxations [11, 12, 13, 14]. We introduce a novel method to treat atomic relaxations in magnetically disordered defect systems in chapter 3. The method is benchmarked using a vacancy defect in body-centered cubic (bcc) Fe as a prototype.

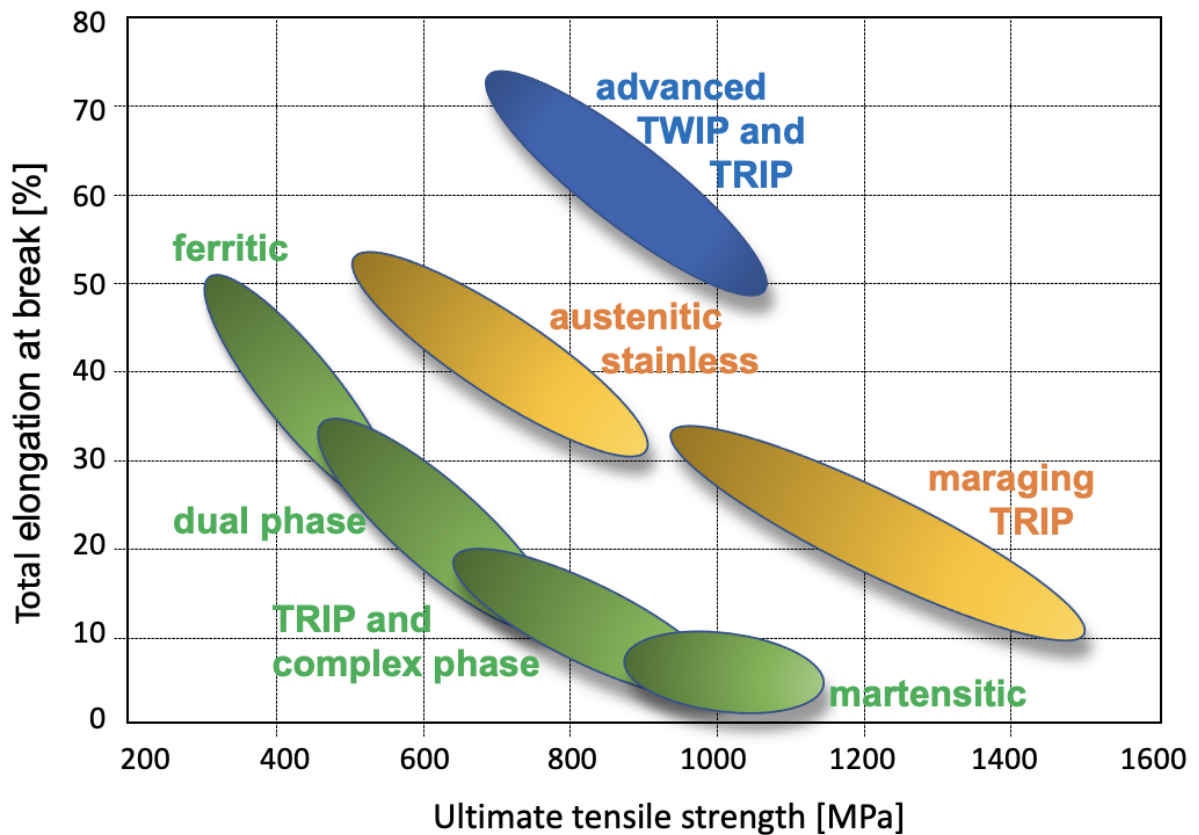


Figure 1-1: Elongation-tensile strength relation for different kinds of steels. The image is adopted from [1] and [2].

FeMn alloys are important constituents of alloy steels, and Mn addition is known to strengthen steels by forming solid solutions in the ferrite. As observed in the phase diagram [15, 16], bcc FeMn is stable up to 5% Mn composition. Computations involving bcc FeMn systems

are known to be cumbersome because of the intricate magnetic interactions between Mn and the Fe matrix [17, 18]. Moreover, vacancy-Mn interplays are ubiquitous in steels, and understanding them is of high interest both theoretically and experimentally. Related to this, the temperature evolution of kinetic properties of Mn in bulk is highly relevant since kinetics determines segregation, precipitation, nucleation, etc., in materials. We try to tackle this by studying vacancy-mediated Mn diffusion in the ferromagnetic and paramagnetic states in chapter 4. The relaxation method developed in chapter 3 is adopted here for the accurate computation of the paramagnetic energies. Among other discussions in the chapter, we discuss the effect of Mn on the distinctive 'kink' or acceleration of diffusion coefficients [19, 20, 21, 22] observed across the magnetic order-disorder transition. During the course of the chapter, we showcase the dominance of magnetic disordering on chemical distinctiveness.

Following the diffusion studies in bulk, we analyse Mn segregation at the grain boundaries in chapter 5. Mn segregation is known to cause grain boundary embrittlement, consequently promoting fracture in steels [23, 24, 25]. Recently, remarkable spinodal decompositions were observed at ferrite (bcc) grain boundaries following Mn segregation [26, 27], which could result in phase transformations from the ferrite (bcc) to austenite (fcc). Therefore, in order to ultimately improve steels' properties, controlled engineering of grain boundaries [24] via a detailed understanding of Mn segregation behaviour is needed at the atomic scale. Various heat treatments are required to achieve such engineering [25], which in turn alter the magnetic state of the system depending on the corresponding temperatures of operation. In this regard, the computational study of the paramagnetic state (i.e., high-temperature, magnetically disordered state) at the grain boundaries is not a trivial task, and is almost non-existent in the literature for steels. Nonetheless, the newly developed relaxation scheme paves an efficient way to tackle this issue. Subsequently, we explore and discuss the structural, chemical, and magnetic interplay at the grain boundaries in both the magnetically ordered and disordered states. Finally, taking the clue from experimental speculations [25] that the vacancies and Mn-vacancy pairs could be pivotal in promoting grain boundary embrittlement, we investigate vacancy formation and perform first-principles tensile tests for different situations at the grain boundary.

Inspired by the impressive structural, chemical, and magnetic interplay at the FeMn grain boundary, we study such coupling, albeit of a different kind, at the twin boundaries in τ -MnAl in chapter 6. τ -MnAl are a class of permanent magnets that have high coercivity, high energy product, and that are hard to demagnetize [28, 29, 30]. The τ phase forms in the Mn composition range of ~ 50 at.% to 60 at.%, and is strongly ferromagnetic. τ -MnAl magnets are recently being considered as alternatives to the high-performing, costly rare-earth-based

magnets and low-performing, cheap ferrites [31, 32]. The experimental Curie temperature (i.e., magnetic order-disorder transition temperature) for τ -MnAl is around 558 K - 653 K [32, 33], and it has been reported that even after heating and keeping the τ -MnAl sample at 473 K for several weeks did not change its magnetic properties substantially [34]. For all these reasons, τ -MnAl deserve significant scientific attention. During the formation of this phase, a large number of twin boundaries occur [35, 36, 37]. Studies involving micromagnetic simulations and Kerr microscopy experiments have shown that the twin boundaries could act as pinning sites for magnetic domains [38, 39], but the connection at the atomic scale remains elusive. As we find in the chapter, these defects bring about dramatic changes in the magnetic properties at the atomic scale that were hitherto unknown. We employ a correlative state-of-the-art theoretical and experimental technique to dissect these findings, which will contribute to the design of these materials with improved magnetic properties.

Thus, beginning with the development of a novel atomic relaxation method for defective magnetically disordered systems in chapter 3, we apply it to reveal vacancy-mediated Mn diffusion properties in bcc FeMn in chapter 4. Following this, we extend the application to the structurally more complex grain boundary defect in chapter 5. Here, we identify structural, chemical, and magnetic couplings, while discussing the highly relevant Mn segregation and subsequent embrittlement. Finally, in the similar spirit, the influence of twin boundaries on magnetic properties in τ -MnAl is presented in chapter 6. In the next chapter, i.e., chapter 2, we the briefly explain the methods adopted to achieve these results.

2 Theoretical methods

2.1 Density-functional theory

Quantum mechanics is necessary to understand the physical properties of materials at the atomic/sub-atomic scale and involves solving the well-known Schrödinger equation. The Schrödinger equation, while having a simple yet beautiful mathematical form, cannot be solved exactly even for materials with more than a few atoms. Therefore, the incredible complexity of many-body interactions at the electronic scale requires certain physically well-justified and meaningful assumptions to reduce the Schrödinger equation to a more tractable form. In this regard, density-functional theory (DFT) has made tremendous progress. Since most of the physical properties of materials are determined by their electronic structure, DFT provides a mathematically rigorous prescription based on electron density to describe the electronic structure of materials from first-principles. Over the last decades, DFT has realized substantial progress in accurately predicting various fundamental physical properties of not only bulk materials, but also systems with point defects, extended defects, surfaces etc.

Since the main results in the thesis are obtained using DFT, a brief overview of the theory is mentioned in the present chapter.

2.1.1 Schrödinger equation and Born-Oppenheimer approximation

The time-independent, non-relativistic Schrödinger equation for a system of N electrons and M nuclei is given as,

$$\hat{H}\Psi(\mathbf{q}, \mathbf{Q}) = E\Psi(\mathbf{q}, \mathbf{Q}) . \quad (2-1)$$

Here, the Hamiltonian \hat{H} contains different kinetic energy and potential energy contributions to the total energy E and can be expressed in atomic units as:

$$\hat{H} = -\frac{1}{2} \sum_{i=1}^N \nabla_i^2 - \frac{1}{2} \sum_{a=1}^M \frac{\nabla_a^2}{M_a} + \sum_{i=1}^N \sum_{j>i}^N \frac{1}{|\mathbf{r}_i - \mathbf{r}_j|} + \sum_{a=1, M}^M \sum_{b>a}^M \frac{Z_a Z_b}{|\mathbf{Q}_a - \mathbf{Q}_b|} - \sum_{i=1}^N \sum_{a=1}^M \frac{Z_a}{|\mathbf{r}_i - \mathbf{Q}_a|} . \quad (2-2)$$

The first term represents the kinetic energy of the electrons and the second term represents the kinetic energy of the nuclei. Here ∇^2 is the Laplace operator and M_a is the mass of nucleus a . The potential part is represented in the last three terms, with the third term describing the repulsive interaction between the electrons and the fourth term describing the repulsive interaction between the nuclei. The last term represents the attractive interaction between the electrons and the nuclei. Z_a, Z_b are the mass numbers of the nuclei a and b respectively. \mathbf{q} collectively represents $3N$ spatial coordinates (\mathbf{r}) and N spin coordinates of the electrons, while \mathbf{Q} describes $3M$ spatial coordinates of the nuclei. Ψ is the wave function of the system.

As discussed before, solving the Schrödinger equation is complicated even for a system with a few atoms. In this regard, certain meaningful assumptions were made by Max Born and Robert Oppenheimer in 1927 to obtain an approximate form of the Hamiltonian in Eq. (2-2), called as the *Born-Oppenheimer approximation* [40]. Within this approximation, since the nucleus is much heavier than the electrons, the nucleus can be considered to be at rest with respect to the electrons. As a consequence, the kinetic energy term for the nuclei in Eq. (2-2) is zero. Further, the nucleus-nucleus repulsive interaction does not vary in space and can be considered to be a constant. Therefore, the electronic part of the Hamiltonian is decoupled from the nucleic part. The resulting electronic Hamiltonian can be written as:

$$\hat{H}_e = -\frac{1}{2} \sum_{i=1}^N \nabla_i^2 + \sum_{i=1}^N \sum_{j>i}^N \frac{1}{|\mathbf{r}_i - \mathbf{r}_j|} - \sum_{i=1}^N \sum_{a=1}^M \frac{Z_a}{|\mathbf{r}_i - \mathbf{Q}_a|}. \quad (2-3)$$

Using the electronic Hamiltonian \hat{H}_e , one can rewrite the Schrödinger equation as:

$$\hat{H}_e \Psi_e = E_e \Psi_e. \quad (2-4)$$

Here, Ψ_e is the electronic wave function and E_e is the electronic part of the total energy E . The nucleic part of the energy E_n consists only of the potential term $\sum_{a=1, Mb>a}^M \sum_{b>a}^M \frac{Z_a Z_b}{|\mathbf{Q}_a - \mathbf{Q}_b|}$ and is a constant as discussed before. Therefore, the total energy is,

$$E = E_e + E_n. \quad (2-5)$$

Despite the aforementioned simplifications, solving the many-body Schrödinger equation remained intractable. Therefore, Hartree (1928) [41] introduced further approximations by assuming the one-electron model where each electron is assumed to be interacting with an averaged field, called as the *mean-field*. In 1930, Fock extended Hartree's model by considering the antisymmetric nature of the Fermionic wave function, known as the *Hartree-Fock method* [42]. The resulting Schrödinger equation is solved iteratively using the *variational*

principle. However, due to the underlying mean-field assumption, the Hartree-Fock method is not very accurate when deviations from this assumption are present.

2.1.2 Electron density

The electron density, $\rho(\mathbf{r})$, can be defined as the number of electrons in a unit-volume at a given point \mathbf{r} in space. Since the square of the wave function $|\Psi_e(\mathbf{q})d\mathbf{q}|^2$ can be regarded as the probability of finding electrons in volume $d\mathbf{q}$, the electron density can be written as:

$$\rho(\mathbf{r}_1) = N \int \dots \int |\Psi_e(\mathbf{q}_1, \dots, \mathbf{q}_i, \dots, \mathbf{q}_N)|^2 ds_1 d\mathbf{q}_2 \dots d\mathbf{q}_i \dots d\mathbf{q}_N, \quad (2-6)$$

where s represents the spin coordinate and $\mathbf{q}_i = (s_i, \mathbf{r}_i)$. It is to be noted that the defined electron density is a multiple integral that provides the probability of finding an electron in the volume element $d\mathbf{r}_1$. By invoking the fact that electrons are indistinguishable, the probability to find any electron is N times the probability to find one electron. Thus,

$$\int \rho(\mathbf{r}_1) d\mathbf{r}_1 = N. \quad (2-7)$$

Therefore, while the wave function is not measurable, the electron density can be measured (for example, from X-ray diffraction experiments) and has a direct physical interpretation. Further, the electron density directly links the wave function to many observable physical properties.

Even before DFT was introduced, the idea to use the electron density as the key variable was attempted as early as in 1927 by Llewellyn Thomas and Enrico Fermi, known as the *Thomas-Fermi model* [43, 44]. Within this model, the kinetic energy and potential energy terms of the Hamiltonian were expressed as functionals of the electron density, thereby expressing the total energy of the ground state as a functional of the electron density. However, the assumption was made without any rigorous proof. In addition, the expression for the kinetic energy was approximated and the exchange and correlation terms were ignored. Because of the aforementioned reasons, the Thomas-Fermi model was inaccurate for many applications.

2.1.3 Hohenberg-Kohn theorems

DFT originated in 1964 with the two theorems put forth by Walter Kohn and Pierre Hohenberg, collectively known as the *Hohenberg-Kohn theorems* [45]. By notating the terms in Eq. (2-3) as

$$\hat{H}_e = \hat{T}_e + \hat{V}_{ee} + \hat{V}_{ext} , \quad (2-8)$$

where, \hat{T}_e is the electron kinetic energy operator, \hat{V}_{ee} is the electron-electron repulsion operator and \hat{V}_{ext} is the external potential due to nucleus-electron attraction. Further, by taking the expectation values with respect to Ψ_e ,

$$\langle \Psi_e | \hat{H}_e | \Psi_e \rangle = \langle \Psi_e | \hat{T}_e | \Psi_e \rangle + \langle \Psi_e | \hat{V}_{ee} | \Psi_e \rangle + \langle \Psi_e | \hat{V}_{ext} | \Psi_e \rangle , \quad (2-9)$$

$$E = T_e + V_{ee} + V_{ext} . \quad (2-10)$$

It is to be noted that the forms of first two terms are universal and independent of the system as they are only dependent on the number of electrons (determined by $\rho(\mathbf{r})$), while the external potential is system dependent.

The first of the two Hohenberg-Kohn theorems states that the external potential (V_{ext}) is a unique functional of the ground-state electron density ($\rho(\mathbf{r})$) and that there exists a one-to-one mapping between them. This relation can be proven by *reductio ad absurdum*. A direct consequence of the theorem is that the Hamiltonian and the total energy are unique functionals of the ground-state electron density. From Eq. (2-10), since the external potential (from the first theorem) and thereby the ground-state energy is a functional of the electron density, one can conclude that T_e and V_{ee} are functionals of the electron density, too. Therefore,

$$E[\rho(\mathbf{r})] = T_e[\rho(\mathbf{r})] + V_{ee}[\rho(\mathbf{r})] + V_{ext}[\rho(\mathbf{r})] . \quad (2-11)$$

The sum of the first two terms $T_e[\rho(\mathbf{r})] + V_{ee}[\rho(\mathbf{r})] = F_{HK}$ has a universal form and is termed as the Hohenberg-Kohn functional, while the external potential is dependent on the system under consideration. If the mathematical form of the Hohenberg-Kohn functional is known, the DFT provides a prescription to solve the Schrödinger equation exactly. However, the search for the form of the functional still continues and is approximated depending on the problem in hand.

The second theorem states that the lowest energy can be achieved as the output only if the ground-state electron density is the input density. Hence, the theorem delivers a powerful way to solve for the true ground-state energy practically, via the variational principle. To summarize, by making the electron density as the central quantity in DFT, the first theorem substantially reduces the dimensionality of the problem (from $3N$ to 3) since it is no longer

dependent on the number of electrons in the system. Finally, the second theorem paves way for the variational principle to solve for the ground-state energy. However, it is to be noted that the exact form of F_{HK} is still unknown. Kohn and Sham addressed the issue in 1965 via the *Kohn-Sham approach* [46].

2.1.4 Kohn-Sham approach

The Kohn-Sham [46] approach focuses on separating the known and unknown parts of F_{HK} , such that all the unknown parts are summed up in one term and that the known part can be determined exactly. Firstly, by decoupling $V_{ee}[\rho(\mathbf{r})]$ as $V_{ee}[\rho(\mathbf{r})] = E_H[\rho(\mathbf{r})] + E_{ncl}[\rho(\mathbf{r})]$ in Eq. (2-11),

$$E[\rho(\mathbf{r})] = T_e[\rho(\mathbf{r})] + E_H[\rho(\mathbf{r})] + E_{ncl}[\rho(\mathbf{r})] + V_{ext}[\rho(\mathbf{r})]. \quad (2-12)$$

Here, $E_H[\rho(\mathbf{r})]$ is known as the Hartree potential, which contains the classical Coulomb interactions and $E_{ncl}[\rho(\mathbf{r})]$ represents the non-classical part of the electron-electron interactions. Next, to provide a more accurate description of the kinetic energy term, Kohn and Sham introduced a set of non-interacting electrons as the reference system and thereby transformed the original many-electrons Schrödinger equation to a set of one-electron Schrödinger equations. In such a fictitious system, the electron density of non-interacting electrons is assumed to be the same as the electron density of the original system with interacting electrons. As a consequence, the kinetic energy of such a fictitious system can be exactly determined. However, it is to be noted that the kinetic energy of the true system of interacting electrons differs from that of the non-interacting system by an unknown term. Such a term is added to $E_{ncl}[\rho(\mathbf{r})]$ and the resulting functional is termed as the exchange-correlation energy. Hence, all the unknowns are collected in the exchange-correlation energy. Therefore,

$$E[\rho(\mathbf{r})] = T_{non-int}[\rho(\mathbf{r})] + E_H[\rho(\mathbf{r})] + E_{XC}[\rho(\mathbf{r})] + V_{ext}[\rho(\mathbf{r})]. \quad (2-13)$$

$T_{non-int}[\rho(\mathbf{r})]$ is the kinetic energy of the fictitious system and $E_{XC}[\rho(\mathbf{r})]$ contains the residual kinetic energy ($T_e - T_{non-int}$) and non-classical electron-electron interactions. Since the exact form of $E_{XC}[\rho(\mathbf{r})]$ is not known, it is approximated by various functionals depending on the material system and the physical quantity of interest.

2.1.5 Exchange-correlation functionals

Different functionals have been introduced to approximate the exchange-correlation potential. Among them, the *local density approximation* (LDA) [47] and *generalized gradient approximation* (GGA) [48] are two of the well-known functionals. A brief overview of LDA

and GGA is summarized as follows:

LDA assumes a uniform electron gas model with constant electron density within each infinitesimal volume of the total volume of the system. While such an assumption is far away from many realistic systems where electron densities vary rapidly in space, it allows for an exact (or very accurate) treatment of the exchange-correlation energy. Within LDA, $E_{XC}[\rho(\mathbf{r})]$ is given as,

$$E_{XC}^{LDA}[\rho(\mathbf{r})] = \int \rho(\mathbf{r})\epsilon_{XC}[\rho(\mathbf{r})]d\mathbf{r} . \quad (2-14)$$

Where, $\epsilon_{XC}[\rho(\mathbf{r})]$ is the exchange-correlation energy per electron in a uniform electron gas with density $\rho(\mathbf{r})$. For spin-polarized systems, a variation of the LDA, known as the local spin-density approximation (LSDA) was introduced. In LSDA, E_{XC} is given as:

$$E_{XC}^{LSDA}[\rho_{\uparrow}(\mathbf{r}), \rho_{\downarrow}(\mathbf{r})] = \int \rho(\mathbf{r})\epsilon_{XC}[\rho_{\uparrow}(\mathbf{r}), \rho_{\downarrow}(\mathbf{r})]d\mathbf{r} , \quad (2-15)$$

with $\rho(\mathbf{r}) = \rho_{\uparrow}(\mathbf{r}) + \rho_{\downarrow}(\mathbf{r})$. In general, the exchange part is overestimated while the correlation part is underestimated in LDA/LSDA. Partly because of the resulting error-cancellation, LDA/LSDA are good approximations for many systems. However, LDA/LSDA fail when the electron density has large spatial variations.

GGA overcomes the aforementioned shortcoming of LDA, by introducing an additional variable: the gradient of the electron density ($\nabla\rho(\mathbf{r})$). $E_{XC}[\rho(\mathbf{r})]$ in GGA attains the following form:

$$E_{XC}^{GGA}[\rho(\mathbf{r})] = \int \rho(\mathbf{r})\epsilon_{XC}[\rho(\mathbf{r}), \nabla\rho(\mathbf{r})]d\mathbf{r} . \quad (2-16)$$

For spin-polarized systems, the spin electron densities and their gradients are considered. In this case, E_{XC} becomes:

$$E_{XC}^{GGA}[\rho_{\uparrow}(\mathbf{r}), \rho_{\downarrow}(\mathbf{r})] = \int f[\rho_{\uparrow}(\mathbf{r}), \rho_{\downarrow}(\mathbf{r}), \nabla\rho_{\uparrow}(\mathbf{r}), \nabla\rho_{\downarrow}(\mathbf{r})]d\mathbf{r} . \quad (2-17)$$

Different forms for $f[\rho_{\uparrow}(\mathbf{r}), \rho_{\downarrow}(\mathbf{r}), \nabla\rho_{\uparrow}(\mathbf{r}), \nabla\rho_{\downarrow}(\mathbf{r})]$ have been proposed in the literature. Some well-known examples are the approximations introduced by Perdew and Wang (PW91) [49] and by Perdew, Burke, and Ernzerhof (PBE) [48]. While GGA gives accurate results for many systems, it is not reliable for strongly correlated systems, semiconductors etc. Further improvements over GGA have been proposed in the literature, of which an example is *meta-GGA* [50], where the Laplacian of the energy density (second order contributions) is taken

into account as an additional variable. GGA-PBE is used in the present thesis, as it is sufficiently accurate for material systems under study.

2.1.6 Pseudopotentials and Projector-Augmented Wave method

In order to increase the computational efficiency of DFT calculations, Heine introduced a pseudopotential approach in 1970 [51]. In this approach, the core electrons are assumed to be frozen, since atomic bonds are mainly formed by the valence electrons. Subsequently, the potential due to nuclei is substituted by an effective potential and the Kohn-Sham equations are solved only for the valence electrons.

Among different pseudopotentials, the projector-augmented wave (PAW) potential proposed by Blöchl (1994) [52] is one of the most commonly used potentials. Mathematically, PAW can be seen as a generalization of the pseudopotential approach and the latter can be obtained naturally from PAW as an approximation. PAW preserves the accuracy of the all-electron potential and simultaneously provides the computational efficiency of the pseudopotential approach. For a deeper understanding, the reader is referred to the seminal paper by Blöchl [*Projector augmented-wave method*, P. E. Blöchl, Phys. Rev. B 50, 17953].

2.1.7 Spin-polarized DFT

The extension of the Hohenberg-Kohn-Sham equations to spin-polarized systems was proposed by Barth and Hadin in 1972 [53]. In this approach, the electron density was replaced by a more general spin density matrix. The spin density matrix $\gamma_{\alpha\beta}(\mathbf{r})$ includes the electron density scalar $\rho(\mathbf{r})$ and magnetization density vector $\mathbf{m}(\mathbf{r})$. $\alpha, \beta = \uparrow, \downarrow$ are the spin variables¹.

$$\gamma_{\alpha\beta}(\mathbf{r}) = \frac{1}{2}(\rho(\mathbf{r})\delta_{\alpha\beta} + m^x(\mathbf{r})\sigma_{\alpha\beta}^x + m^y(\mathbf{r})\sigma_{\alpha\beta}^y + m^z(\mathbf{r})\sigma_{\alpha\beta}^z). \quad (2-18)$$

Here, δ and $\boldsymbol{\sigma} = (\sigma^x, \sigma^y, \sigma^z)$ are the identity and Pauli matrices respectively and are of the order of 2×2 . The Pauli matrices are:

$$\sigma^x = \begin{pmatrix} 0 & 1 \\ 1 & 0 \end{pmatrix} \quad \sigma^y = \begin{pmatrix} 0 & -i \\ i & 0 \end{pmatrix} \quad \sigma^z = \begin{pmatrix} 1 & 0 \\ 0 & -1 \end{pmatrix}. \quad (2-19)$$

¹It is to be noted that the scalar electron densities were used for spin-polarized cases in Eq. (2-17) and Eq. (2-15) for the ease of representation, whereas a general matrix notation for the spin density is adopted in this section.

Instead of the scalar electron density, the spin density is the fundamental variable in spin-polarized DFT. Hence, the Kohn-Sham energy functional can be represented as,

$$E[\gamma_{\alpha\beta}(\mathbf{r})] = T_{non-int}[\gamma_{\alpha\beta}(\mathbf{r})] + E_H[\gamma_{\alpha\beta}(\mathbf{r})] + E_{XC}[\gamma_{\alpha\beta}(\mathbf{r})] + V_{ext}[\gamma_{\alpha\beta}(\mathbf{r})]. \quad (2-20)$$

The above prescription for the spin density matrix to treat magnetism in DFT is applicable to both collinear and non-collinear magnetic systems. In the case of non-collinear magnets, the spin density matrix will have non-zero off-diagonal components, whereas they reduce to zero in the case of collinear magnets (from Eq. (2-18), since m^y , m^x are zero for a collinear system). Further, the form of the Kohn-Sham energy functional remains the same as described by Eq. (2-20), irrespective of the collinear or non-collinear cases.

2.2 Magnetic disorder

Magnetism plays a significant role in determining structural and chemical properties of many materials such as Fe-based alloys. On exposure to real environment conditions, magnetic behaviour, and thereby the physical properties of materials can change. An important example is the change from an ordered magnetic state to a disordered (or paramagnetic) state when a magnetic material is exposed to high temperatures. Therefore, the relevance of understanding such magnetic excitations and their proper treatment is paramount.

Early models to treat magnetism were based either on the local moments model (Heisenberg-like, where electrons are assumed to be localized) or the itinerant electrons model (based on Stoner description) [10]. Further, Moriya introduced a model [54] that treats the local moment model and the itinerant model as limiting cases. Moriya described magnetism based on spin density fluctuations and used the notion of average local moments. In 3d-transition elements like Fe and their alloys, magnetism is determined by itinerant electrons that are strongly localized on atoms and the longitudinal fluctuations survive even above the Curie temperature. Therefore, one can assume that they behave in Heisenberg-like manner. Since Moriya's work, the theoretical understanding of ordered magnetic materials has found substantial progress in condensed matter physics and material science. On the other hand, the study of magnetic disorder is a relatively young scientific field and still needs development of new methods, largely owing to the difficulty in handling complex interactions of random magnetic moments.

Different methods have been introduced to treat magnetic disorder in bulk systems. Since the central idea of the thesis is to develop and apply a computationally efficient yet accurate

method to describe the impact of magnetic disorder on defect properties, only the ingredients used to achieve this goal are described in the current section.

2.2.1 Disordered Local Moments and Special Quasirandom Structures

DFT provides an accurate description of paramagnetic energies and forces that are necessary to describe defect properties. The disordered local moment (DLM) method, introduced by Hubbard [55] and Hasegawa [56], aims at treating magnetic disorder within DFT. DLM considers magnetic moment vectors with finite sizes and random directions that are fixed in space at lattice sites. Hence, a small subset of the infinite configuration space is sampled and the temporal variation of moments are mapped onto the space. However, DFT calculations involving non-collinear magnetic moments are cumbersome and computationally demanding. In this regard, Gyorffy et al. [57] rigorously proved that one can ignore non-collinearity within DLM by assuming complete randomness of moments and forsaking the spin-orbit coupling. DLM can be coupled with single-site approximations such as the coherent-potential approximation (CPA) [57], to calculate paramagnetic energies. However, the CPA method fails to account for atomic relaxations, especially in the presence of defects such as vacancies, grain boundaries etc. where accurate computations of atomic forces are pivotal. The solution to the problem would be to employ the supercell approach, where the configuration space is modelled by a supercell that repeats in space as a consequence of applying periodic boundary conditions.

While DLM establishes that magnetic disorder can be emulated within DFT by performing calculations on a set of configurations with random collinear moments, the question remains as to how to choose such configurations from the huge set of possible candidates within the supercell approach. An efficient way to tackle the issue is to employ special quasirandom structures (SQS), originally demonstrated for chemical disorder by Zunger et al. in 1990 [58]. SQS has been later extended and applied to magnetic disorder successfully. Considering the Heisenberg Hamiltonian for magnetism,

$$H_m = - \sum_{i,j \neq i} J_{ij} \mathbf{e}_i \cdot \mathbf{e}_j , \quad (2-21)$$

where, e_i, e_j are the unit vectors in the same directions as of the magnetic moments at sites i and j respectively. J_{ij} is the magnetic exchange parameter. Considering η^{th} coordination shell, the same equation can be rewritten as:

$$H_m = - \sum_{\eta} J_{\eta} n_{\eta} \langle \phi_{\eta} \rangle . \quad (2-22)$$

Here, j_η is the effective exchange parameter, n_η is the number of atoms and $\langle \phi_\eta \rangle$ is the average spin correlation function in the η^{th} shell respectively. For the fully paramagnetic state, the spin correlation function $\langle \phi_\eta \rangle$ should reduce to:

$$\langle \phi_\eta \rangle = \frac{1}{N} \sum_{i,j \subset \eta} \mathbf{e}_i \cdot \mathbf{e}_j = 0 . \quad (2-23)$$

SQS gives a prescription for a paramagnetic supercell to satisfy Eq. (2-23) for the given H_m . Hence, SQS is an efficient tool to simulate magnetic disorder within supercell based DFT. Computationally, the magnetic structure as given by SQS has to be preserved over the course of DFT calculations, as the spins can flip since disordered magnetic states are unstable. To achieve this, the spins need to be constrained and the constraint scheme needs to be robust, efficient and reliable in determining paramagnetic energies. Such a spin constraint scheme is discussed next.

2.2.2 Spin constraints

Early works on implementing spin constraints within DFT relied on adding penalty contributions to the total energy expression. As a result, computationally demanding convergence tests need to be carried out to reduce the penalty energies, since they can lead to inaccurate total energies. An alternative, computationally robust constraint method [3] based on the PAW formalism implemented by Maximilian Grabowski and Christoph Freysoldt (Max-Planck-Institut für Eisenforschung) is discussed in this section. This tool is tested and applied in the atomic relaxation method [3] developed (discussed in the next chapter) by the author in the present thesis. In general, the total spin moment can be defined as,

$$\mathbf{M}^{tot} = \int d^3\mathbf{r} \mathbf{M}(\mathbf{r}) , \quad (2-24)$$

where $\mathbf{M}(\mathbf{r})$ is the magnetization density,

$$M_p(\mathbf{r}) = \sum_{\alpha\beta} \sigma_{\alpha\beta}^p \sum_n f_n \psi_{n\alpha}^*(\mathbf{r}) \psi_{n\beta}(\mathbf{r}) . \quad (2-25)$$

Here, p corresponds to a Cartesian component, f_n is the occupation number. The rest of the symbols have the same meaning as discussed in earlier sections. The total spin moment Eq. (2-25) is not sufficient to characterize magnetic disorder in the system since local magnetic moments of individual atoms need to be defined. Among different definitions for magnetic moment of an atom that are available in the literature, the PAW based definition allows to enforce constraints to high accuracy. In this formalism, the atomic moment is linked

to the partial-wave within the PAW sphere and is given as,

$$M^a = \sum_{ij\alpha} \chi_\alpha \gamma_{ij}^{a\alpha} \Omega_{ij} , \quad (2-26)$$

where M^a refers to the atomic moment of atom a and χ is the spin sign,

$$\chi_\alpha = \begin{cases} +1 & \text{for } \alpha = \uparrow \\ -1 & \text{for } \alpha = \downarrow \end{cases} . \quad (2-27)$$

Ω_{ij} is an integral defined by the partial-waves within the PAW cut-off radius r^{cut} , and has the dimension of volume -

$$\Omega_{ij} = \int d^3\mathbf{r} \phi_i(\mathbf{r})\phi_j(\mathbf{r})\Theta(r^{cut} - |\mathbf{r} - \mathbf{r}^a|) , \quad (2-28)$$

where Θ is the Heaviside function and $\phi(\mathbf{r})$ is the partial-wave. Since the atomic moments are well-defined in 2-26, spin constraints can be introduced via the standard Lagrange formalism. Therefore, the goal is to find the stationary points of the functional

$$\mathcal{L} = F^{el}[\psi_{\{n\sigma\}}, f_{\{n\sigma\}}] - \sum_a \nu_a (M^a[\psi_{\{n\sigma\}}, f_{\{n\sigma\}}] - M^{a,target}) .$$

Here, $M^{a,target}$ are the target spins, and ν_a the corresponding constraints that enter the equation as Lagrangian multipliers. F^{el} refers to the electronic free energy functional. The stationary points are found by minimizing the functional with respect to Lagrangian parameters, i.e.,

$$\frac{\delta \mathcal{L}}{\delta \langle \psi_n |} = 0 , \quad (2-29)$$

$$\frac{\partial \mathcal{L}}{\partial f_n} = 0 , \text{ and} \quad (2-30)$$

$$\frac{\partial \mathcal{L}}{\partial \nu_a} = 0 . \quad (2-31)$$

Therefore, along with usual constraints ψ_n and f_n , the spin constraints ν enter the Hamiltonian. Consequently, an additional factor or term is added to the Kohn-Sham equation. For a self-consistent algorithm to solve the constrained Kohn-Sham equation, the spin constraints ν should be determined. In order to achieve this, in the first step, an iterative diagonalization is used to solve the constrained Kohn-Sham equation for the given charge density. Using the resulting eigenfunctions and eigenvalues, initial magnetic moments and spin constraints are updated via a conjugate gradient minimization. Finally, corresponding wave functions are

calculated and the new charge density is found out to be used as input for the next iteration in the constrained Kohn-Sham equation.

Within the aforementioned approach, the spin constraint on each atom has a physical meaning since it can be considered as an external magnetic field that drives the atomic moment towards the target moment. To summarize, the approach may be considered as a local projection of the wave function onto a locally reduced basis set. Within this projection, the constraining field then takes the form of a homogeneous magnetic field inside the PAW cut-off sphere.

2.2.3 Atomic forces and Spin-Space Averaging

Atomic forces are fundamental ingredients to compute atomic relaxations. Consequently, the accuracy of various properties (such as phonons, defect energies, diffusion coefficients etc.) depends on the accuracy of forces. In general, sophisticated electronic structure methods such as dynamical mean-field theory (DMFT) cannot compute atomic forces efficiently. On the other hand, empirical approaches like the embedded atom method (EAM) do not capture the magnetic degrees of freedom correctly. In this regard, DFT has proved to be very successful in the accurate and efficient computation of forces in magnetic systems. The Hellmann-Feynman forces as obtained from DFT are *true* forces for magnetically ordered states at low magnetic temperatures. On the other hand, the magnetic degrees of freedom are much faster than the atomic degrees of freedom at high magnetic temperatures, leading to their adiabatic decoupling. Therefore, the atoms do not observe instantaneous forces (or Hellmann-Feynman forces) of any particular magnetic configuration, rather they experience an averaged force of many configurations. Thus, only an average of energies of different magnetic configurations is not sufficient but an average of forces is necessary to capture and characterize magnetic disorder.

The spin-space averaging (SSA) approach introduced by Körmann et al. (2012) [59] is based on the aforementioned idea. The SSA forces are defined as:

$$\mathbf{F}_{SSA}^i = \sum_{K=1,M} p_K \mathbf{F}_K^i, \quad (2-32)$$

where, \mathbf{F}_K^i is the Hellmann-Feynman force on the i^{th} atom in the K^{th} magnetic configuration, M is the total number of magnetic configurations and \mathbf{F}_{SSA}^i is the spin-space averaged force on the i^{th} atom. p_K denotes the Boltzmann weight for the K^{th} magnetic configuration given as $p_K = \exp[-E_K^{BO}/k_B T]/Z$, where E_K^{BO} is the magnetic Born-Oppenheimer energy

for the K^{th} magnetic configuration, k_B is the Boltzmann constant and Z is the magnetic partition sum. For a complete magnetically disordered state, we are interested in the fully paramagnetic limit of $T \rightarrow \infty$, in which all configurations have the same weight $p_K = 1/M$.

3 Atomic relaxation method for magnetically disordered materials with defects

(The main results of the chapter have been published in - *Atomic relaxation around defects in magnetically disordered materials computed by atomic spin constraints within an efficient Lagrange formalism*. Omkar Hegde, Maximilian Grabowski, Xie Zhang, Osamu Waseda, Tilmann Hickel, Christoph Freysoldt, and Jörg Neugebauer, Phys. Rev. B 102, 144101 (2020))

3.1 Introduction

Physical and structural properties of materials differ when they are exposed to different environmental conditions. For example, structural defects such as vacancies emerge at high temperatures. Simultaneously, physical properties such as the magnetic state and entropic excitations of the material change. Therefore, in order to understand effects of structural defects on material characteristics, it is necessary to study their behaviour in the presence of high temperature magnetic state, which is a disordered state in general. Methodologically, the treatment of magnetic disorder is challenging. In addition, the presence of defects adds to the challenge, since the coupling of structural and magnetic degrees of freedom needs to be handled carefully. The coupling affects atomic relaxations that arise from bond breakage due to deviations from ordered structural configuration, and relaxations in turn depend on atomic forces. Thus, atomic forces are fundamental in determining defect properties and their accurate description requires a parameter-free theory.

First-principles density-functional theory (DFT) has been the front runner for such calculations [60]. DFT provides an accurate description of forces at the atomic level, and achieves it within the confines of computational limits. While empirical methods such as embedded atom methods (EAM) do not accurately capture atomic forces, advanced electronic structure methods such as dynamical mean-field theory (DMFT) demand computational efforts that

are impractical to achieve for current standards.

As discussed in chapter 2, many studies have been performed in order to understand bulk properties of magnetically disordered materials [61, 62, 63, 64, 65, 66, 67]. Similarly, DFT has made great progress in understanding defect systems [68]. However, only a few theoretical works that combine both magnetic disorder and defects can be found in the literature [69, 70, 10, 71, 72, 73, 74]. Such studies employ approximative methods to calculate defect energies, especially by making assumptions on atomic relaxations. For example, some of these studies [69, 11, 12] assume the atomic geometry in the ferromagnetic geometry for the paramagnetic state. However, through tracer diffusion experiments, Iijima et al. [22] have shown that the atomic relaxations around the vacancy in the paramagnetic state are larger than the relaxations in the ferromagnetic state. On the other hand, some studies [13, 14] fully relax atoms in each magnetic configuration. We show in this chapter that such a set-up that is based on the assumption that the time-scale for magnetic relaxations are comparable to that of atomic relaxations can lead to vacancy energies that are largely different from experimental values. These approximative schemes are discussed in the results section of the chapter. Recently, Gambino and Alling [71] computed atomic relaxations within the adiabatic approximation. In this case, an averaging over atomic positions obtained from a set of calculations with changing magnetic configurations was carried out. However, the approach converges the forces indirectly without a direct control over their accuracy, and requires a large number of DFT calculations to achieve this goal.

In the present chapter, a newly developed atomic relaxation method [3] based on spin-space averaging (SSA) [63] is presented. SSA was originally introduced to describe phonons in paramagnetic (PM) or magnetically disordered materials (discussed in methodology chapter). SSA is based on the adiabatic limit, a physical approach to the PM state, where the magnetic degrees of freedom are assumed to change much faster compared to the atomic degrees of freedom. Therefore, SSA relies on computing averaged forces obtained from many different magnetic configurations, rather than instantaneous forces from any particular magnetic configuration. The disordered local moment (DLM) model (discussed in chapter 2) is used to sample the configurational space of the PM state within the supercell approach of DFT. Since such excited states or configurations are far from the energy minimum or ground-state, a robust and reliable spin-constraint approach (discussed in methodology chapter) is used to constrain the magnetic moments so that the magnetic disorder is conserved throughout the calculation run.

The new relaxation method (SSA relaxation method/scheme) is applied to a prototype sys-

tem of body-centered cubic (bcc) Fe with a vacancy as the defect, since many works in the literature are available for comparison. Another motivation is to gain new insights into vacancy formation, migration and activation energies, since vacancy energetics can be decisive in understanding diffusion mechanisms and mechanical properties of the material. The results obtained from SSA relaxation method are compared with alternative, approximative relaxation approaches. The impact of volume expansion and comparisons with experimental literature are discussed.

The chapter is organized as follows: section 3.2 discusses generation of magnetic configurations, section 3.3 presents simulation algorithm for SSA relaxations, computational details are discussed in section 3.4. Results are presented and discussed in section 3.5 and the chapter is concluded with section 3.6.

3.2 Generating random magnetic configurations

By neglecting spin-orbital coupling, magnetic disorder can be represented by randomised collinear atomic moments within DFT [57]. In this regard, special-quasirandom structures (SQSs) [58, 75] provide an efficient prescription to emulate randomness in a given supercell, as discussed in chapter 2. Originally introduced for chemical disorder, the SQS approach has been generalized for magnetic disorder [75, 76] and several works in the literature have successfully employed collinear SQSs to reveal PM bulk properties in different materials [75, 77, 59, 76]. In the present chapter, a perfect bulk in the PM state is sampled by applying spin constraints on randomly distributed spin-up and spin-down magnetic moments provided by a binary SQS, such that the total magnetic moment sums up to zero. An example of the SQS structure for a $2 \times 2 \times 2$ bcc cell is shown in Fig. 3-1. Different SQSs can be generated by considering different pair correlation functions. In Tab. 3-1 energies and lattice parameters of different magnetic SQSs are compared. Since the energies and lattice parameters are very similar for different SQSs, a single SQS is sufficient to represent the bulk PM state. Such an observation is supported by previous studies [77], where different magnetic SQSs with different pair correlation functions were shown to yield similar energies and equilibrium volumes in bcc Fe.

Unlike the situation in perfect bulk, creating a vacancy in a bulk SQS results in a specific magnetic environment around the vacancy. Therefore, various local magnetic environments need to be superimposed for a proper representation of the PM state. In order to generate different magnetic structures with a vacancy, either a vacancy can be created at the same position in different SQSs or a vacancy can be created at different positions in a given SQS. The

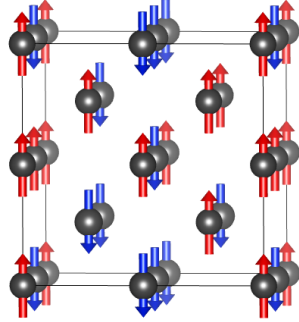


Figure 3-1: An example of a SQS structure for a $2 \times 2 \times 2$ bcc cell is shown. Note that the actual calculations employ a $3 \times 3 \times 3$ bcc cell.

Magnetic state	ΔE (meV)	a (\AA)
Ferromagnetic	0	2.834
Paramagnetic (SQS A)	193	2.829
Paramagnetic (SQS B)	196	2.830
Paramagnetic (SQS C)	196	2.830

Table 3-1: Comparison of energy differences (ΔE) and lattice parameters (a (\AA)) for the bulk ferromagnetic (FM) and PM states. Different SQSs that are generated by considering different correlation functions are compared for the PM state. ΔE is the energy difference with respect to the FM ground-state at 0 K. $3 \times 3 \times 3$ supercells are considered for the calculations.

latter method has two advantages: (1) It is similar to the spin-wave method [69, 12], where a completeness of spin configurations is ensured and thereby the translational symmetry of the system is naturally incorporated (2) generating a single parent SQS is sufficient for both the bulk and vacancy structures, without any need for additional SQSs. The choice of the parent SQS is neither unique nor crucial, as realized in Tab. 3-1. In addition to generating different magnetic configurations, atomic forces are symmetrized according to the structural symmetries of the system and thereby effectively increasing the total number of magnetic snapshots.

It is to be noted that once an atom is removed from the bulk SQS to create a vacancy, the total magnetic moment is not zero. A magnetic moment which is equal in magnitude and opposite in direction to the spin of the removed atom remains as surplus. Nonetheless, since a superposition of different magnetic configurations with either positive or negative residual spins is considered, the effective moment of the vacancy can be regarded as zero.

3.3 Protocol for SSA relaxation

The algorithm for carrying out relaxation in the PM limit is shown in Fig. 3-2 and discussed in the current section:

- After generating random magnetic configurations as discussed in the above section, a

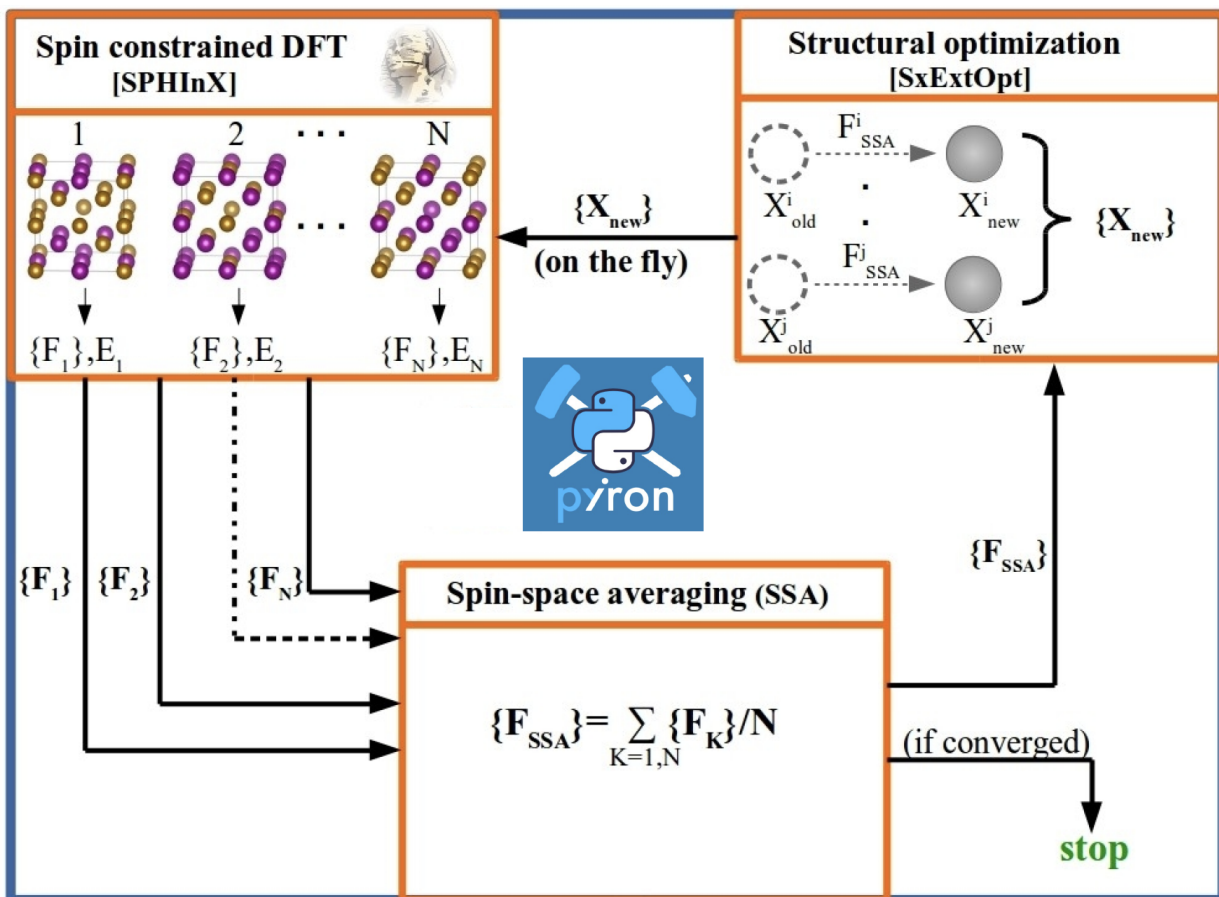


Figure 3-2: Schematic picture with the algorithm for the SSA relaxation method. Various tools (Random magnetic configuration generator, DFT code with spin constraint tool, SSA scheme, External structural optimizer, and ART tool for migration barrier calculations) are combined and connected to build the final protocol [3].

static spin-constrained DFT calculation is performed on each magnetic configuration. Such a constraint scheme is discussed in the last chapter, and is applied for the first time to obtain the results in the present chapter. The forces on the atoms in all magnetic configurations are collected after the electronic minimization. A set of forces obtained from each magnetic configuration, say N^{th} configuration for example, is represented as $\{F_N\}$ and the total energy as E_N in Fig. 3-2.

- Each atom experiences a different force in different magnetic configurations. Forces on each atom from all the configurations are averaged according to the SSA scheme (discussed in the methodology chapter) [63]. The SSA force in the PM limit is defined as:

$$\mathbf{F}_{SSA}^i = \frac{1}{N} \sum_{K=1}^N \mathbf{F}_K^i. \quad (3-1)$$

Here, \mathbf{F}_{SSA}^i is the SSA force on the i^{th} atom. \mathbf{F}_K^i is the force on the i^{th} atom in the K^{th} magnetic configuration, N is the total number of magnetic configurations.

- In the next step, the SSA forces are symmetrized according to the crystal symmetries of the system. It is to be noted that symmetry-breaking might occur in defect structures that could be smothered by explicit symmetrization. However, such a situation does not arise in the present system of study, i.e., bcc Fe with a vacancy.
- In the case of calculations involving saddle-point configurations (or migration barriers), the symmetrized SSA forces are further transformed according to the activation-relaxation technique (ART) [78, 79]. ART systematically explores the local potential energy surface and activates the migrating atom from the local minimum to the adjacent saddle point. Thus, ART bypasses the need for an expensive search of entire transition path.
- In the following step, the atoms are relaxed according to the SSA forces (or SSA + ART forces in the migration barrier calculations). For this purpose, the optimization scheme 'external structure optimizer' (SxExtOpt) [80] is used in our work. The advantage of using SxExtOpt is two-fold: (1) The structural optimization scheme needs to interrupt the calculation and should carry out the optimization externally, since the output forces from DFT calculations undergo a series of treatments as discussed above. SxExtOpt facilitates such an external optimization (2) SxExtOpt parametrizes the force Hessian on the fly and therefore ensures fast convergence. Since SSA relaxation scheme is, in general, computationally much more expensive than a simple DFT run, a faster convergence of the geometry is much desired.
- The new output geometry from structural optimization is provided as an input structure for magnetic configurations for the next set of spin-constrained DFT calculations. The steps discussed before are repeated until the SSA forces are converged to the required criterion.

The relaxation scheme described is referred to as 'SSA relaxation'. The schematic of such a protocol is represented in Fig. **3-2**. To bring together different parts of the complex algorithm, the python based integrated development environment (IDE) *pyiron* [81] is used. *pyiron* provides a platform to set-up DFT calculations, perform external optimizations and analyze the output data.

3.4 Computational details

The SPHInX package [82] is used to perform DFT calculations. The calculations employ PAW [83, 84] formalism with the Perdew-Burke-Ernzerhof (PBE) flavor of the generalized-gradient approximation (GGA) [85, 48]. A $3 \times 3 \times 3$ cell of 54 atoms is used for all bulk calculations, while vacancy calculations involve 53 atoms. The 0 K equilibrium lattice parameter for both the FM and PM states is found to be about 2.83 Å (Tab. **3-1**). For the calculations that include volume expansion in the paramagnetic state, a lattice constant of 2.87 Å is used. This value is obtained using the relative lattice expansion coefficient near the Curie temperature that is measured from experiments [86]. Fermi-Dirac smearing is used for all the calculations, with a smearing width of 0.1 eV. The width is chosen such that the corresponding electronic temperature (about 1160 K) is above the Curie temperature (1043 K) in order to emulate electronic temperature in the PM state. Further, it is verified that reducing the smearing width to 0.05 eV changed the vacancy formation energy by only about 2 meV. An energy cut-off of 600 eV and \mathbf{k} -point mesh of $6 \times 6 \times 6$ are chosen. 10^{-5} eV is chosen to be the convergence criterion for the total energy in the electronic relaxation loop. Ionic relaxation is stopped when the forces are converged within 0.015 eV/Å. The convergence of SSA forces for the first and second nearest-neighbour atoms of the vacancy in the vacancy formation energy calculation are shown in Fig. **3-3**.

Magnetic moments are allowed to relax for FM calculations, whereas the spin constraints are applied for PM calculations. For the PM bulk, moments are constrained to $2.1 \mu_B$ as obtained from a moment-energy optimization at 0 K. In the presence of the vacancy, the change in the magnitude of magnetic moment of the nearest-neighbour atoms is considered after carrying out a set of spin constrained calculations to identify the optimum moment magnitude ($2.3 \mu_B$) via moment-energy optimization. However, it is to be noted that constraining moment magnitude is an approximation. Therefore, it is necessary to ensure that the resulting contribution to the total energy is small. To derive the penalty energy that arises from constraints, one can use Lagrange multipliers as

$$\nu_a = dE/dM^a, \quad (3-2)$$

where, ν_a is the Lagrange multiplier, E is the energy and M^a is the magnetic moment of atom a . Near the optimum value, the energy depends quadratically on the magnetic moment, i.e.,

$$\Delta E = \frac{(dE/dM)^2}{2S}. \quad (3-3)$$

Here, $S = d^2E/dM^2 = d\nu/dM$ is the spin stiffness. For the current study, the root-mean-

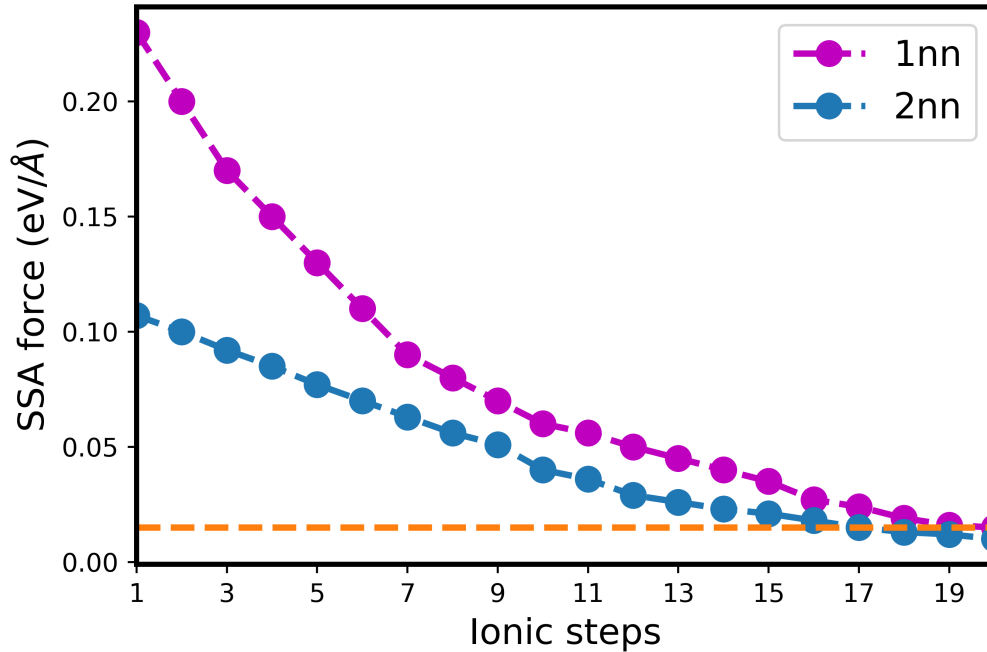


Figure 3-3: Convergence of SSA forces for the first and second nearest-neighbour atoms of the vacancy. The ionic relaxation is stopped when the force on each atom is within 0.015 eV/\AA , which is marked by the orange dashed line.

square (rms) value for the constraining field strength is $\text{rms}(\nu) = 30 \text{ meV}/\mu_B$. From the bulk calculations, the spin stiffness of $S = 550 \text{ meV}/\mu_B^2$ per atom is extracted. Using these values, the energy contribution from constraints is found to be small and is about 1 meV per atom. In addition, the value is similar for bulk, vacancy and transition states. As a result, the error cancellations from the energy differences will further reduce the impact of constraining magnitudes of moments. Therefore, constraining the magnitudes is not a major assumption, while it substantially improves the numerical efficiency of DFT calculations.

The convergence of vacancy formation energies with respect to the number of magnetic structures is considered: the difference in vacancy formation energies calculated for six and eight configurations is found to be about 20 meV and the difference in vacancy formation energies calculated for seven and eight structures is found to be about 5 meV . Thus, eight configurations are chosen for all PM calculations. Further, the symmetries of the crystal structure are utilized while symmetrizing the forces, which increases the total number of magnetic snapshots. For example, for the vacancy state, the effective number of magnetic snapshots is $8 \times 48 = 384$. Therefore, the number of magnetic configurations needed to achieve convergence depends inversely on the number of symmetries of the system.

The vacancy formation energy is calculated as [68]

$$E_f = E_{N-1}^{\text{vac}} - \left(\frac{N-1}{N} \right) E_N^{\text{bulk}}, \quad (3-4)$$

and the migration energy as

$$E_m = E_{N-1}^{\text{saddle}} - E_{N-1}^{\text{vac}}. \quad (3-5)$$

Here, E_{N-1}^{vac} , E_N^{bulk} , E_{N-1}^{saddle} are the energies of - supercell with vacancy, a perfect bulk and a supercell with a saddle-point, respectively. In the case of SSA relaxations (i.e., paramagnetic case), the averaged total energy obtained from all the magnetic configurations after achieving the convergence of SSA forces is considered. ART [78] is used to determine migration barriers. The activation energy E_a is defined as the sum of the vacancy formation energy E_f and the vacancy migration energy E_m .

3.5 Results and Discussion

The application of the SSA relaxation scheme to bcc Fe as a prototypical material system and the resulting physical insights are presented in the current section. The calculated values of vacancy formation energies, migration energies and activation energies for different cases are summarized in Tab. **3-2**. The impacts of magnetic disordering, relaxations and volume expansion are discussed systematically as follows:

3.5.1 Impact of magnetic disorder

Bcc Fe shows a strong FM ordering at low temperatures. In the FM state, the calculated formation, migration and activation energies are 2.15 eV, 0.74 eV and 2.89 eV respectively, as shown in Tab. **3-2** and Fig. **3-4**. These values are well in agreement with experiments ($E_a^{\text{FM}} = 3.01$ eV [89], 2.75 eV [22]) and previous theoretical results [12, 11]. Thus, in order to properly capture the PM state, it is to be noted that magnetic disorder such as the one given by the SQS structure is indeed required. In other words, as discussed in chapter 2, the pair correlation functions need to be reduced to zero (or close to zero) for a proper sampling of the PM state and only achieving zero magnetization is not sufficient. For example, assuming an ordered magnetic configuration such as the antiferromagnetic (AFM) state in place of random magnetic configurations can lead to erroneous results for the PM state: when vacancy calculations are performed in the AFM state, a negative vacancy formation energy is obtained. The negative value arises because the removal of an atom to create

	E_f (eV)	E_m (eV)	E_a (eV)
This work			
FM	2.15	0.74	2.89
PM (SSA relaxed)	1.62	0.30	1.92
PM (unrelaxed)	1.94	0.63	2.57
PM (FM relaxed)	1.71	0.50	2.21
PM (individually relaxed)	0.99	0.45	1.44
PM (SSA, $a = 2.87$ Å)	1.89	0.35	2.24
Experimental values for PM			
Matter <i>et al.</i> [87]	1.60		
de Schepper <i>et al.</i> [88]	1.79		
Iijima <i>et al.</i> [22]			2.61
de Schepper <i>et al.</i> [89]			2.37
Other theoretical values for PM			
Gambino <i>et al.</i> [71] ($a = 2.84$ Å)	1.61		
Ruban <i>et al.</i> [69] ($a = 2.90$ Å)	1.77		
Sandberg <i>et al.</i> [11]	1.54	0.40	1.97
Ding <i>et al.</i> [12] ($a = 2.90$ Å)	1.98	0.43	2.41

Table 3-2: First-principles values of activation energy E_a for self-diffusion, the vacancy formation energy E_f and the migration barrier E_m for nearest neighbour vacancy jumps [3] in bcc Fe. For the PM state, energies obtained from different relaxation schemes are compared. The values are presented for the theoretical equilibrium lattice constant $a = 2.83$ Å, if not indicated differently.

the vacancy results in a more stable state that involves a ferromagnetic interaction of the eight nearest neighbour atoms around the vacancy. Since the vacancy formation energy is negative, further calculation of the migration barrier has not been performed. Though the AFM state does not occur at any temperature in bcc Fe, the distinctive result of negative vacancy formation energy signifies the importance of considering disordered local magnetic moments for the PM state.

On introducing magnetic disorder, the vacancy energies decrease substantially and systematically compared to the FM state: the vacancy formation energy for the SSA relaxation (1.62 eV) is ~ 0.5 eV smaller and the migration energy (0.30 eV) is reduced by 0.44 eV, resulting in a difference of about 1 eV in the activation energy (Fig. 3-4). The larger vacancy energies in the FM state as compared to the PM state could be because the formation of a vacancy involves overcoming both the structural and magnetic symmetries in the FM state. The relative effect is highest in the case of the migration energy, where the magnetic

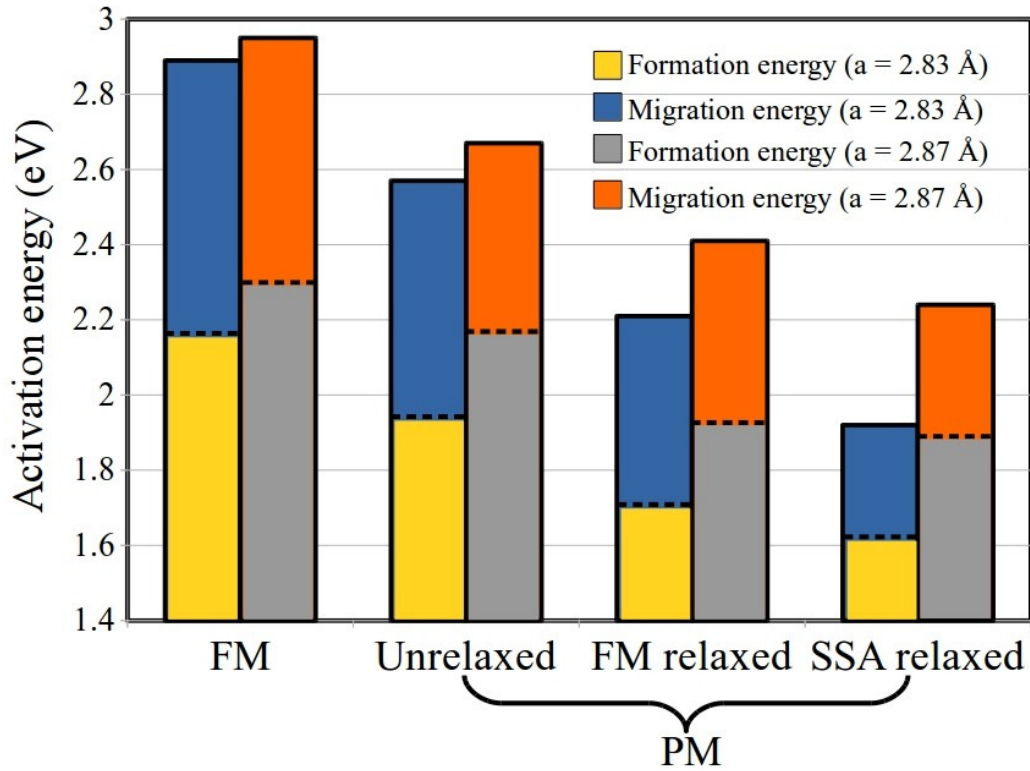


Figure 3-4: Comparison of activation energies, which are the sums of formation energies (lower section of each bar) and migration energies (upper section of each bar), between physically realistic SSA relaxations and other relaxation considerations in the PM state in bcc Fe. Results are shown for the theoretical equilibrium lattice constant ($a = 2.83 \text{ \AA}$) and at a high-temperature lattice constant ($a = 2.87 \text{ \AA}$) close to the Curie temperature [3].

disorder changes the migration barrier by more than 50% as compared to the FM barrier. The change in the activation energies of the two magnetic states manifests as a prominent kink (first-order transition) in the diffusion-coefficients (Fig. 4-5 in chapter 4) at the Curie temperature. Thus, magnetic disorder has a dramatic effect on vacancy energetics. The impact of atomic relaxations on vacancy energies is discussed next.

3.5.2 Impact of atomic relaxations

The main results obtained from the SSA relaxation are described in this section. These main results are compared with approximative relaxation schemes that are used in the literature (mentioned in the introduction of the chapter). Accordingly, the PM vacancy energies are classified as those obtained from (1) the unrelaxed case, (2) the FM relaxed case, (3) the

SSA relaxation, and (4) the individually relaxed case. The results concerning the equilibrium lattice parameter, i.e., $a = 2.83 \text{ \AA}$, are discussed in the current section Fig. **3-4**. Each of the relaxation schemes is defined and discussed in detail as follows.

1. In the unrelaxed case, the vacancy energies are calculated by averaging the total energies of different magnetic configurations that have the atomic structure of the perfect bulk in which an atom is removed to create a vacancy. The main reason to consider such a case is straightforward: the vacancy energies obtained from this case purely incorporate the effect of magnetic disorder and this gives an opportunity to decouple its effect on relaxations and relaxation energies. In such a case, the vacancy formation energy is 1.94 eV, the migration energy is 0.63 eV and the activation energy is 2.57 eV. The activation energy is smaller than the FM counterpart by 0.32 eV, which signifies the strong impact of magnetic disordering. However, this is only about a one-third of the total decrease in the PM state as obtained from SSA relaxation. Consequently, it is evident that the relaxation effects are crucial and cannot be neglected.
2. Similar to the unrelaxed case, the FM relaxed values are obtained by freezing the atomic structure of all the magnetic configurations, but to the relaxed geometry in the FM state. The underlying assumption in such a method is that the structural configuration corresponding to the PM minimum is close to that of the FM minimum. While the FM relaxed method has been used in the literature [12, 11], a careful and proper treatment of atomic relaxations in the PM state is necessary for many systems, including bcc Fe. As shown in Fig. **3-4**, for this case, the vacancy formation energy is 1.71 eV, the migration energy is 0.50 eV, and the activation energy is 2.21 eV. Compared to the activation energy in the FM state, where the structural configuration is the same but the magnetic state is different, the reduction is 0.68 eV. On the other hand, compared to the activation energy in the unrelaxed case, where the structural configuration is different but the magnetic state is the same, the reduction is 0.36 eV. Therefore, it is evident that while the change in the magnetic state is the most dominant factor in driving the reduction in activation energy, the contribution of atomic relaxations is still significant.
3. The last bar in Fig. **3-4** shows values corresponding to the SSA relaxation method. Physically, the SSA relaxation scheme is nearest to the true picture, where an atom in the PM state experiences an averaged force because of the rapidly changing magnetic environment. Here, the vacancy formation, migration, and activation energies are 1.62 eV, 0.30 eV, 1.92 eV, respectively. Therefore, the reduction in activation energy compared to the activation energy in the FM relaxed state is about 0.3 eV. This

signifies that it is crucial not only to consider the proper magnetic state, but also proper relaxations in the proper magnetic state. The migration energy for the SSA relaxation is the lowest amongst all the schemes, and the migration energy calculations depend on relaxations in both the vacancy state and saddle-point state.

4. Another commonly employed relaxation scheme in the literature [13, 14] is the ‘individually relaxed’ scheme. Here, each random magnetic configuration used for the SSA averaging is allowed to relax completely until the forces on all the atoms in that particular magnetic configuration are vanishingly small. The averaged energy of all such configurations is considered. Unlike any of the previous cases, here different magnetic configurations end up with different atomic configurations after structural relaxations. Such a relaxation method differs fundamentally from the SSA relaxation, because the physical picture in the individually relaxed scheme assumes a time-scale for the magnetic degrees of freedom that is comparable to that of the atomic degrees of freedom. In other words, each atom is assumed to react and adjust to a specific magnetic environment unlike the SSA relaxation. The vacancy energies are listed in the 5th row in Tab. **3-2**. Clearly, the vacancy formation energy (0.99 eV) and the activation energy (1.44 eV) are substantially smaller and the lowest of all the relaxation schemes. The reduction in the energies can be attributed to the stronger relaxations of atoms, as they are not constrained by any external conditions. In the case of the vacancy state, symmetry breaking relaxations are observed, leading to further decrease in the formation energy. On the other hand, the SSA relaxation counterpart has a larger value, since the structural minimization in this case does not correspond to the minimization of any single random magnetic configuration, but is correlated to many configurations.

The large difference in the activation energies is rooted in the underlying assumptions on time-scales of the atomic and magnetic degrees of freedom. In the individually relaxed scheme, the time-scales are assumed to be comparable, whereas in the SSA relaxation scheme, the magnetic degrees of freedom are much faster than atomic degrees of freedom (adiabatic limit). The observation (5th row in Tab. **3-2**) that the activation energy obtained from the individually relaxed scheme is unrealistic and artificial justifies the assumption of the adiabatic limit. The vacancy formation energy from the SSA relaxation is in agreement with the value obtained by Gambino et al. [71], where a position averaging scheme was considered in the adiabatic limit.

The atomic geometries obtained in different relaxation schemes for the nearest-neighbour atoms of the vacancy are quantified in terms of their displacements from their positions in the perfect bulk in Fig. **3-5**. The structural configuration is different for different magnetic

configurations in the individually relaxed scheme. Therefore, the averages of displacements, which are calculated over all these structural configurations, are considered to represent the relaxations in the individually relaxed case in Fig. 3-5. The SSA displacements are sandwiched in between the other two schemes. Due to crystal symmetries, all the first nearest-neighbour atoms of the vacancy in the vacancy state can be quantified by the same value. However, these atoms can be further classified as the first, second and third nearest-neighbours of the migrating atom in the saddle-point case. From the figure - (1) the yellow coloured atoms are the first nearest-neighbours and experience a slightly repulsive force away from the migrating atom, (2) the second nearest-neighbour atom marked in green experiences a small attractive pull towards the vacancy and (3) the third nearest-neighbour atoms marked in orange are benefited by the atoms moving away from the vacancy and at the same time attracted by two vacancies, resulting in large displacements into the core. In bcc structures, second nearest-neighbour atoms of the vacancy in the vacancy state also undergo significant relaxations. The relaxations of these second nearest-neighbour atoms show similar trend as the first nearest-neighbour atoms with respect to the different relaxation schemes. The displacements or relaxations in the PM state as observed from the SSA relaxation are larger compared to the FM state. Such an observation is in agreement with conclusions from tracer diffusion experiments by Iijima et al. [22]. The tracer diffusion coefficients for the self-diffusion in bcc Fe obtained from this work were used to find the fraction of the kinetic energy that is carried by the migrating atom via the equations derived in earlier works [90, 91]. In turn, the fraction of the kinetic energy of migrating atom is related to the activation volume [92, 90], which is an effective measure of atomic relaxations during the vacancy activation. Consequently, the atomic relaxations in the PM state were found to be relatively larger than the FM state.

3.5.3 Inclusion of volume expansion

At high temperatures, volume expansion occurs and hence it becomes necessary to incorporate the change in lattice parameter for the PM state. While the results in the previous sections correspond to the equilibrium lattice parameter ($a = 2.83 \text{ \AA}$) at 0 K, the current section describes the effect of lattice expansion. To this end, a lattice parameter of 2.87 \AA that is obtained by extrapolating the equilibrium lattice constant using the experimental relative lattice expansion co-efficient [86] above the Curie temperature is used. The inclusion of volume expansion makes the comparison with experimental results more viable.

The vacancy formation, migration, and activation energies after including volume expansion are compared with those of with equilibrium volume in Fig. 3-4. Evidently, the inclusion

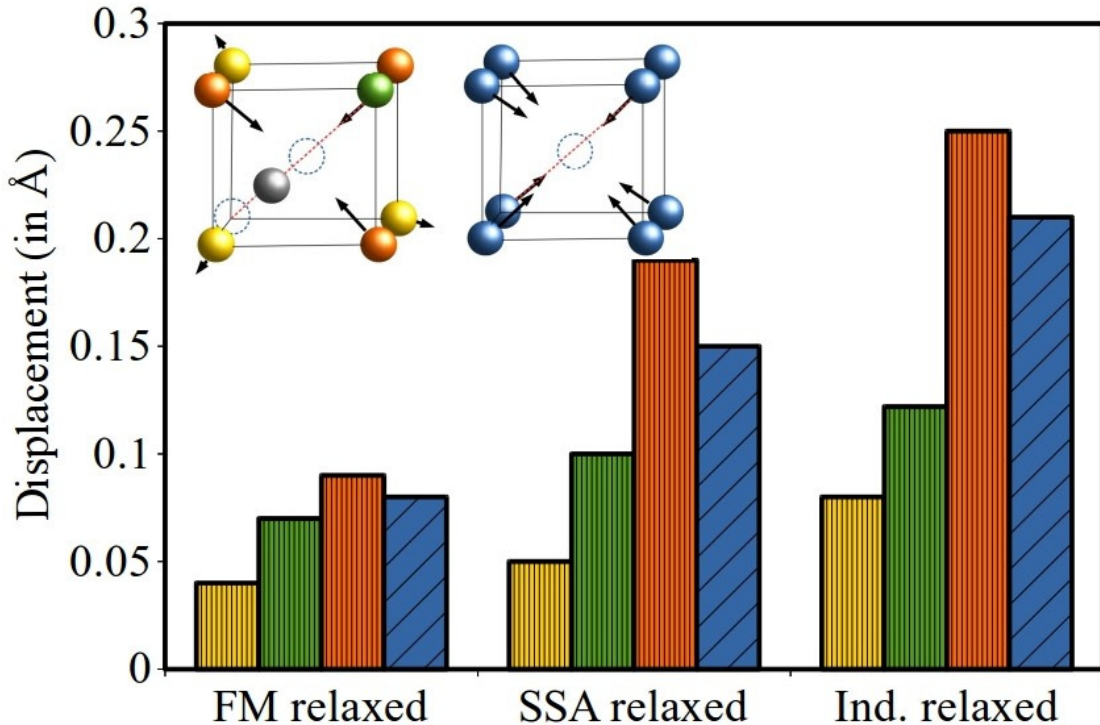


Figure 3-5: Displacements of nearest-neighbour atoms of the vacancy for different relaxation schemes for the PM state of bcc Fe are shown [3]. Atoms are represented according to local symmetry, and the displacements are linked to the corresponding atoms in the diagrams given in the inset. Blue bars show the displacement in the vacancy state and yellow, green, and orange bars depict the displacements in the transition state.

of volume expansion results in an increase of vacancy activation energy, driven largely by the increase in formation energy. This is because of the smaller equilibrium volume for the vacancy formation as compared to the bulk equilibrium volume. The activation energy for the SSA relaxation in this case is 2.24 eV, with the formation energy of 1.89 eV and the migration energy of 0.35 eV. It is to be noted that the activation energy has a similar value as that of the FM relaxed scheme (2.21 eV) with equilibrium lattice constant. This is only a coincidence and could be because of error cancellation in the FM relaxed case: the exclusion of both proper SSA relaxation (which reduces the activation energy relatively) and volume expansion (which increases the activation energy) could lead to such a cancellation. In general, both SSA relaxations and volume expansion need to be considered for a more exact treatment of magnetic disorder at high-temperatures.

The available literature (Table **3-2**) for vacancy formation and activation energy in bcc Fe show dispersed values, for both theory and experiments. The experiments can be largely classified as positron annihilation experiments [93, 87, 88] and tracer diffusion experiments [89, 22]. de Schepper et al. [88] studied a high purity sample for positron annihilation experiments as compared to previous experiments in the literature. The vacancy formation energy from volume expansion inclusive SSA relaxation (1.89 eV) is in good agreement with such positron annihilation experiments by de Schepper et al., (1.79 ± 0.10). The tracer diffusion experiments [89, 22] observe that the relaxations in the PM state is larger compared to the FM state, agreeing with the SSA relaxation calculations. Quantitatively, the activation energies obtained from the tracer diffusion experiments (2.37-2.61 eV) are larger compared to the value obtained from SSA relaxations (2.24 eV). Though the magnetic entropy is not explicitly calculated in the present study, it is to be noted that the SSA relaxation method presented in this chapter is aimed at obtaining total energies in the paramagnetic (fully disordered, at high temperatures) state, where the magnetic entropy contributions to the vacancy formation and migration free energies are known to be zero due to cancellation effects when taking the difference between the defect and perfect bulk cell [74]. This is also true for the fully ordered ferromagnetic state for similar reasons.

3.6 Conclusions

A new physically realistic atomic relaxation scheme, which captures the adiabatic limit for defect systems in the presence of magnetic disorder, is introduced. Within the limitations of DFT and the adiabatic limit, the SSA relaxation scheme is an exact method that is computationally efficient. In developing the SSA relaxation method, various tools are combined and collaborated with the DFT code SPHInX. However, the structure of the method is designed with a goal of smooth transferability to any DFT code that has a constrained magnetism scheme, and the method can be applied to magnetically disordered materials with any kind of defects.

The SSA relaxation is benchmarked by applying it to bcc Fe with a vacancy by calculating the vacancy formation, migration, activation energies in the PM state. Comparisons are made with the relaxation schemes commonly employed in the literature. All the PM results are consistently smaller compared to the values in the FM state, in agreement with the experimental literature. In general, the impact of magnetic disorder is found to be dominant in determining vacancy energies, while a significant contribution arises from the relaxations. Differences in the activation energies obtained from the FM relaxed scheme, individually relaxed scheme as compared to the SSA relaxations provide new physical insights: The

FM relaxations (or displacements) are much different and smaller compared to the SSA (or PM) relaxations, in agreement with the experimental observations. The activation energy obtained from the individually relaxed scheme is too small and different compared to the SSA relaxation scheme and experiments. This finding establishes that the slow time-scale for magnetic degrees of freedom as assumed in the individually relaxed scheme is far from physical reality. The adiabatic limit, where the magnetic degrees of freedom are faster compared to the atomic degrees of freedom assumed in SSA relaxations, is justified. The atomic displacements in the SSA relaxation are larger than the FM relaxed and smaller than the individually relaxed displacements. This indirectly implies that in a system where the displacements (and hence resulting energies) obtained from the FM relaxed and individually relaxed schemes show similar values, the more expensive SSA relaxations could be replaced by one of these cheaper relaxation schemes or by taking the energy average of both the schemes.

Further, the impact of volume expansion is studied by performing SSA relaxations using the lattice parameter of the system at the Curie temperature. The results show a notable increase in the vacancy formation and activation energies. Finally, it is shown that for a viable comparison with the experiments, the SSA relaxations as well as the volume expansion need to be included for the high-temperature PM state.

4 Impact of magnetism on diffusion of Mn in α -Fe bulk

4.1 Introduction

The study of diffusion, which is a crucial kinetic phenomenon, is needed to understand the physics of segregation, nucleation and precipitation in materials. As a consequence, also mechanical properties of materials depend on their atomic diffusion processes. For this reason, understanding diffusion properties is paramount in systems such as Fe-based alloys that have important practical applications.

FeMn systems form an important class of steels. Mn segregation from bulk to extended defects such as grain boundaries and dislocations in steels is well-known but detailed physical knowledge as to their kinetics and mechanisms is lacking. A part of such an understanding concerns Mn diffusion in the bulk. Properties such as diffusion coefficients in Fe-based alloys have been measured via tracer diffusion experiments [6, 94, 95, 5, 96, 97, 98, 99, 100, 101, 102, 103, 104, 105, 106]. However, these measurements are restricted by the temperature range they can access. While the theoretical computation of diffusion in non-magnetic materials is relatively straightforward, magnetic systems such as α -Fe and its alloys exhibit a characteristic deviation from the Arrhenius behaviour as the magnetic order undergoes a transition to a disordered state above the Curie temperature. While several theoretical studies are available for self-diffusion in pure Fe [107, 108, 109, 110, 74], the treatment of paramagnetic (PM) state in these works is typically subjected to serious assumptions on atomic relaxations, as discussed in the previous chapter. In comparison, studies regarding Mn-vacancy diffusion in Fe are scarce [111, 112]. Both these works reported the vacancy-Mn binding energies, vacancy formation energies and migration barriers in the FM state but ignored the PM state.

In the present chapter, the SSA relaxations method introduced before is employed to gain physical insights into the diffusion of Mn in Fe. Diffusion coefficients, solute-solvent diffusion ratios and correlations factors are central physical quantities that need to be computed in order to investigate diffusion mechanisms. The Ruch model [113], which is based on a model

introduced by Girilfaco [114], is used here to compute self diffusion coefficients. Le Claire's model [115] provides the ratio of diffusion coefficients of the solute to that of the solvent. These models are discussed in the next section. The computational details are provided in Sec. 4.3, results and discussions in Sec. 4.4 and the conclusions of the chapter are drawn in Sec. 4.5.

4.2 Diffusion coefficients

4.2.1 Ruch model

Diffusion in material systems such as bcc Fe and its alloys deviates from the Arrhenius behaviour across the magnetic order-disorder transition, resulting in a characteristic kink in the diffusion profile. Here, the diffusion accelerates with respect to temperature when transforming from an ordered to a disordered magnetic state. To predict such a diffusion profile, Ruch *et al.* introduced a model [113] that interpolates vacancy activation energies between the magnetically ordered (FM) and disordered (PM) states:

$$D(T) = D(0) \exp \left[-\frac{E_a^{\text{PM}}(1 + \alpha S(T)^2)}{RT} \right]. \quad (4-1)$$

Here, $D(T)$ is the diffusion coefficient at temperature T , $D(0)$ is the pre-exponential factor, E_a^{PM} is the activation energy in the PM state, S is the normalized magnetization at temperature T and R is the universal gas constant. The α parameter is given by,

$$\alpha = \frac{E_a^{\text{FM}} - E_a^{\text{PM}}}{E_a^{\text{PM}}}. \quad (4-2)$$

Therefore, the description of diffusion coefficients requires the determination of activation energies in the FM and PM states. It is interesting to note that while the FM activation energies are straightforward to capture in first-principle studies, the low-temperature diffusion coefficients or activation energies are difficult to measure in tracer diffusion experiments. On the other hand, the opposite is true for the high temperature PM state.

4.2.2 Ratio of diffusion coefficients

In the presence of a solute atom next to the vacancy, the relative rate of solute diffusion coefficients with respect to self-diffusion coefficients of the host atom provides useful insights. To this end, Le Claire formulated [115] a model based on the nearest neighbour (NN) jumps of the vacancy, which provides the ratio of diffusion coefficient of the solute to that of the

host atom. Taking the example of the FeMn system, the ratio is given by,

$$\frac{D_{\text{Mn}}}{D_{\text{Fe}}} = \frac{f_2 \omega_2 \omega_4}{f_0 \omega_0 \omega_3} \quad \text{with} \quad \omega_i = \nu e^{-\frac{E_m^{(i)}}{k_B T}}, \quad (4-3)$$

where D_{Mn} and D_{Fe} are the Mn and Fe diffusion coefficients respectively, and ω_i are the jump frequencies. ν are the attempt frequencies that depend on the mass of the atom. f_0 is the correlation factor of the pure system, and is a constant for the given crystal structure. For the bcc systems, f_0 is 0.7272. In the present case of Mn in Fe, the attempt frequencies of Fe and Mn are assumed to be equal, since their atomic masses are similar.

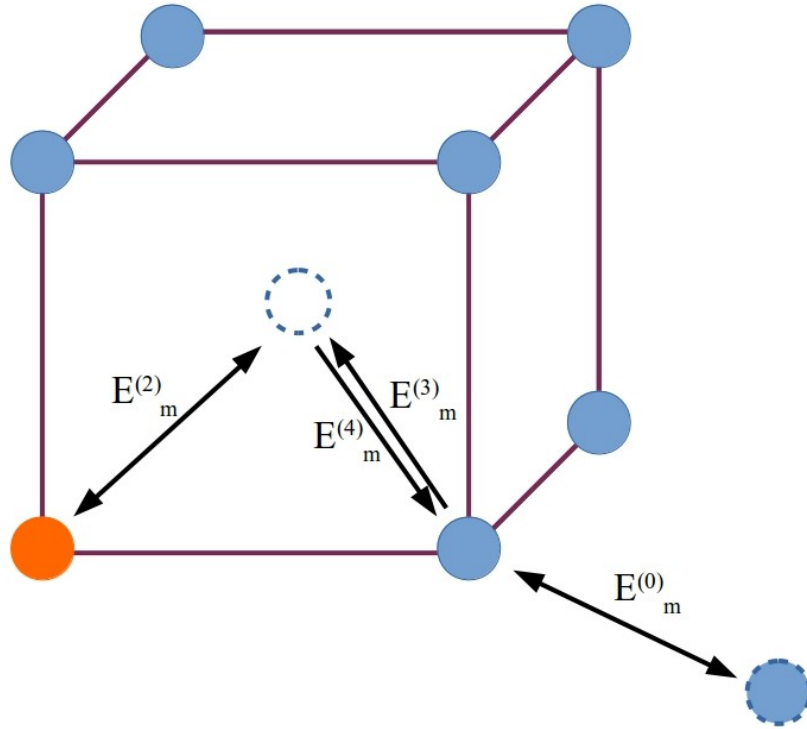


Figure 4-1: Migration energies for the $1NN$ jumps of the vacancy (dashed circle) in the vicinity of a solute atom (orange circle). $E_m^{(0)}$ is the self-diffusion migration barrier of the host atom and represents any jump that is not affected by the presence of the solute atom. Arrows represent the directions of atomic jump.

Different migration barriers considered for the Le Claire's model are presented in Fig. 4-1. Unlike the case in pure Fe with a vacancy, where all the $1NN$ jumps were similar, the presence of a solute causes non-random or correlated jumps. Such correlations are stored in f_2 , known as the kinetic correlation factor of the solute. f_2 is a function of all the NN jumps

and is given by,

$$f_2 = \frac{\mu}{2(\omega_2/\omega_3) + \mu} \quad (4-4)$$

$$\begin{aligned} \mu &= 7 - \left(1 + 0.512 \left(\frac{\omega_0}{\omega_4}\right)\right)^{-1} \\ &- 2 \left(1 + 1.536 \left(\frac{\omega_0}{\omega_4}\right)\right)^{-1} - \left(1 + 3.584 \left(\frac{\omega_0}{\omega_4}\right)\right)^{-1} \end{aligned} \quad (4-5)$$

f_2 attains values between 0 and 1. The smaller the f_2 , the more correlated are the vacancy-solute jumps and vice-versa. This means that the chemical environment is highly distinguishable for the vacancy if f_2 is smaller, and indistinguishable as f_2 approaches the asymptotic value f_0 (f_2 approaches f_0 when $\omega_2 \approx \omega_3$ and $\omega_3 \approx \omega_4$, from Eq. (4-6)). Subsequently, $D_{Mn} \approx D_{Fe}$ (from Eq. (4-3)). For more details regarding the equations, the reader is referred to LeClaire [115] and Manning [116].

4.2.3 Mixing scheme for the ratio of diffusion coefficients

The Ruch model provides a prescription for interpolating between the FM and PM activation energies via the α parameter (Eq. (4-2)), given by -

$$E_a(T) = E_a^{\text{PM}}(1 + \alpha S(T)^2) . \quad (4-6)$$

An explicit calculation of the migration barrier at each intermediate temperature is computationally costly. Therefore, in order to evaluate the diffusion ratios as discussed previously, one needs an interpolation scheme for individual migration barriers, too. To realise this, an interpolation scheme similar to that for the activation energies is employed for each migration barrier:

$$E_m(T) = E_m^{\text{PM}}(1 + \alpha_m S(T)^2) , \quad (4-7)$$

where E_m is the migration energy or barrier. Here, α_m is given by,

$$\alpha_m = (E_m^{\text{FM}} - E_m^{\text{PM}})/E_m^{\text{PM}} . \quad (4-8)$$

Therefore, each migration jump is associated with a specific α_m . In order to compare the impact of different interpolation schemes, a similar interpolation was applied directly on the diffusion coefficients instead of individual migration energies, and the obtained results were very similar. Therefore, for the rest of the chapter, only the aforementioned interpolation of

migration energies is considered to discuss the results. The interpolated migration barriers are further used to determine the diffusion coefficients and kinetic correlation factors. The Ruch model is employed to determine the diffusion coefficients of pure Fe, and the Le Claire's model is further used to extract the Mn diffusion coefficients from the ratios. Experimental values of the pre-exponential factor and magnetization [117] are used as input parameters for the Ruch model.

4.3 Computational details

4.3.1 DFT based calculations

The DFT calculations are performed with the SPHInX [118] code, by employing the Perdew-Burke-Ernzerhof (PBE) generalized-gradient approximation (GGA) [85, 48], using the projector augmented wave (PAW) [119, 120] formalism. In order to make direct comparisons with experimental results, the experimental lattice constants [86] of 2.86 Å and 2.90 Å are considered for the FM and PM states respectively. These values are larger than their corresponding equilibrium lattice constants at 0 K (obtained from DFT) as a result of thermal expansion. $3 \times 3 \times 3$ supercells of 54 atoms are considered for bulk calculations and a single vacancy is created for vacancy calculations. For the FeMn system, a single Fe atom is replaced by a Mn atom.

A $6 \times 6 \times 6$ k -point mesh and an energy cut-off of 600 eV are taken for all the calculations. The error in total energy due to the choice of these parameters is minimized to 1 meV/atom after careful convergence tests. A smearing width of 0.1 eV, within the Fermi-Dirac smearing scheme, is chosen. The criterion for electronic convergence of the total energy is 10^{-5} eV. Structural optimization for atomic relaxations is carried out with SxExtOpt [80]. The convergence criterion for atomic forces in structural optimization is set to 0.015 eV/Å.

As discussed in the previous chapter, spin constrained calculations are performed for the PM state. Magnetically disordered structures are generated using the SQS [58] method. Adiabatic decoupling, where the magnetic degrees of freedom are rapidly changing relative to the atomic degrees of freedom, is assumed. The previously introduced SSA relaxation method [3] is employed for all the calculations in the PM state. The results obtained using the SSA relaxations are labelled as DFT-SSA in figures involving comparisons with the experiments and effective interaction model (discussed below). Spins are not constrained for the FM calculations. In the FM bulk state, Mn couples antiferromagnetically to Fe ($-2.05 \mu_B$), whereas it attains a moment magnitude of $1.8 \mu_B$ in the PM state. The magnetic

moments in the PM state for both the bulk and vacancy structures are determined by careful moment-energy optimizations. The presence of Mn in the proximity of the vacancy results in the vacancy-Mn binding energy given by,

$$E_{\text{binding}} = \left(E_{\text{vac}}^{(N-1)} + E_{\text{Mn}}^{(N-1)} \right) - \left(E_{\text{vac,Mn}}^{(N-2)} + E^{(N)} \right). \quad (4-9)$$

The energies on the right hand side of the equation refer to supercells with a single vacancy, with a single Mn atom in the Fe bulk, with both the vacancy and Mn atom, and without both, respectively. Here, N is the total number of Fe atoms is in the pure bcc bulk state. For the PM state, energies of different magnetic configurations are averaged to obtain each term. According to this definition, a positive binding energy refers to an attractive interaction between the vacancy and the Mn atom.

The migration barriers are computed by Activation-Relaxation Technique (ART) [121]. The migration energy corresponding to the transition (trans) state is defined as:

$$E_m = E_{\text{trans}} - E_{\text{vac}}, \quad (4-10)$$

where E_{trans} is the energy of the transition state supercell.

4.3.2 Effective interaction model and tracer diffusion experiments

The main results of the current chapter are compared with the results of the colleagues from CEA Saclay (A. Schneider, F. Soisson, C.-C. Fu) and the University of Münster (V. Kulitckii, S. Divinski, G. Wilde), where the former contributed through an effective interaction model (EIM) coupled with Monte Carlo (MC) simulations [74] and the latter conducted tracer diffusion experiments. Therefore, some of the central figures present the results of these studies along with those of DFT-SSA. However, these results are added to compare and confirm the independent results obtained in the current chapter, and are not a part of the thesis. The results are a part of the publication: *The impact of magnetic transition on Mn diffusion in α -iron: Correlative state-of-the-art theoretical and experimental study*, O. Hegde, V. Kulitckii, A. Schneider, F. Soisson, T. Hickel, J. Neugebauer, G. Wilde, S. Divinski, C.-C. Fu, *Phys. Rev. B* 104, 184107 (2021) [4].

4.4 Results and discussions

The results pertaining to vacancy energies are discussed first in this section, followed by a discussion on diffusion properties.

4.4.1 Vacancy energies

The vacancy formation energies in pure Fe for the FM and PM states are 2.22 eV and 1.96 eV respectively, for the experimental lattice parameters. The presence of Mn generates a binding energy with the vacancy, calculated according to Eq. (4-9). In the FM state, the $1NN$ binding energy between Mn and the vacancy is 0.15 eV and reduces to 0.10 eV in the PM state. Here, the positive value refers to an attractive interaction between the solute and the vacancy. The $1NN$ vacancy-Mn binding energy in the FM state reported in the literature (0.15 eV [112], 0.17 eV [111]) is in good agreement with the the current work. The energies in the PM state have not been reported before. When Mn is present at the $2NN$ distance, the binding energies are 0.06 eV and 0.03 eV for the FM and PM states, respectively. Small values for the $2NN$ binding energies indicate that the $2NN$ jumps of the vacancy can be neglected. To determine the formation energies at intermediate temperatures, they are obtained by subtracting the migration energy at any given temperature from the activation energy at the same temperature, both of which are given by the Ruch model discussed before. The resulting profiles of formation energies for pure Fe and Mn in Fe are shown in Fig. 4-2.

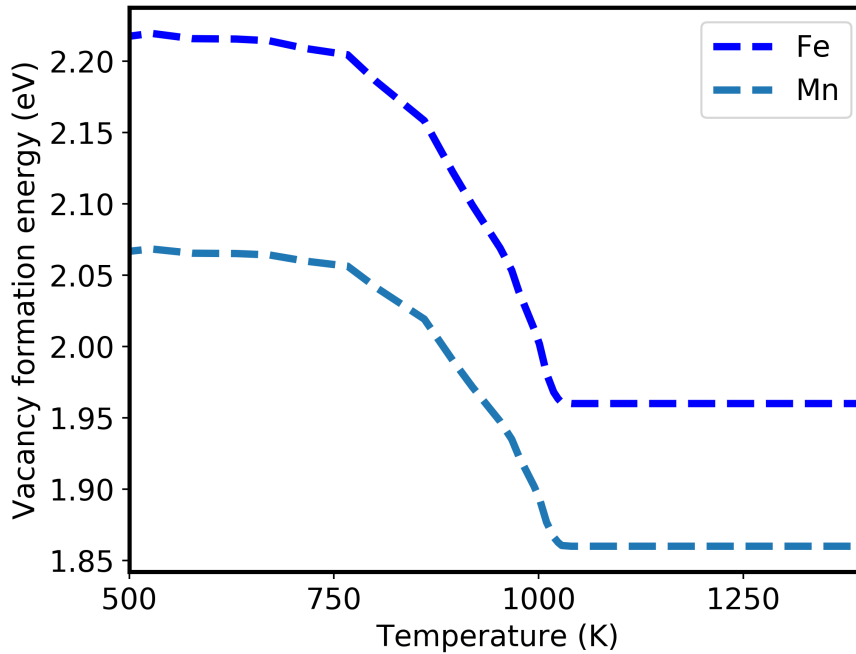


Figure 4-2: Vacancy formation energies in pure Fe and in the dilute case of Mn in Fe. The vacancy is positioned at $1NN$ distance from Mn in the dilute FeMn system.

Migration energies (eV)		
	Ferromagnetic	Paramagnetic
$E_m^{(0)}$	0.73	0.43
$E_m^{(2)}$	0.46	0.41
$E_m^{(3)}$	0.64	0.42
$E_m^{(4)}$	0.58	0.36

Table 4-1: The calculated migration energies for the exchanges of the vacancy with nearest neighbour atoms in both the FM and PM states in pure Fe and dilute FeMn system. $E_m^{(0)}$ is the migration barrier for the jump in pure Fe (or any Fe jump that is unaffected by the presence of Mn). $E_m^{(2)}$ is the migration barrier for the Mn jump. $E_m^{(3)}$ and $E_m^{(4)}$ represent the Fe jumps that dissociate and associate Mn-vacancy pair, respectively (Fig. 4-1).

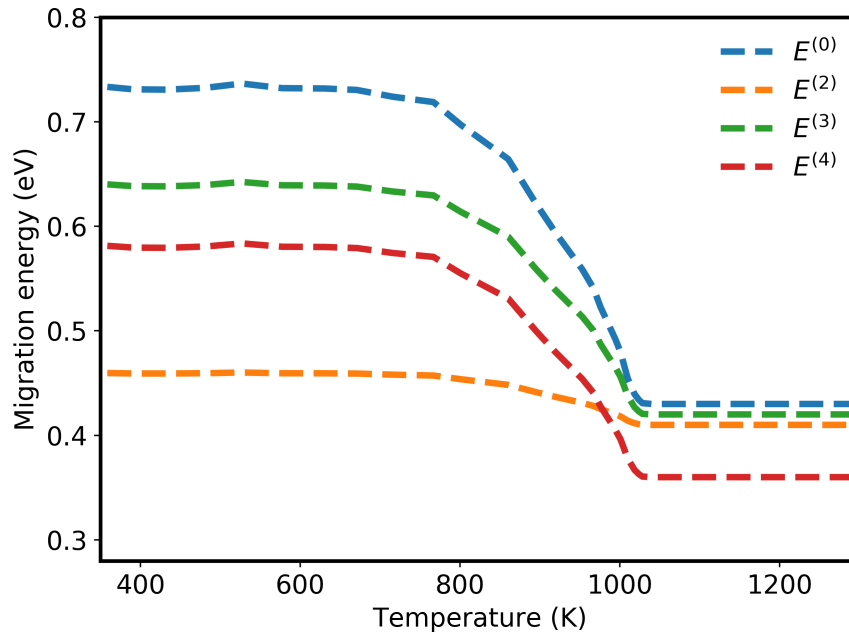


Figure 4-3: Vacancy migration energies for the intermediate temperatures obtained by the Ruch interpolation for the $1NN$ jumps of the vacancy in FeMn [4].

Different migration barriers for the jumps depicted in Fig. 4-3 and the limiting values in the fully FM and PM states are enlisted in Tab. 4-1. Clearly, the energies for the PM jumps are significantly smaller than their FM counterparts. This is because of magnetic disordering reduces the barriers and in addition larger relaxations in the PM state result in further decrease of the barriers. It is interesting to note that the migration energy of Mn ($E_m^{(2)} = 0.46$

eV) differs largely from the pure Fe barrier ($E_m^{(0)} = 0.73$ eV) in the FM state. This is a first indication that Mn diffuses much faster than Fe in the FM state. The fact that the jump that associates the vacancy and Mn ($E_m^{(3)}$) is smaller than the jump that dissociates them ($E_m^{(4)}$) agrees well with the observation that the $1NN$ Mn-vacancy binding is attractive, in both the FM and PM states.

These fully FM and PM migration barriers are further fitted according to the Ruch model as given in Eq. (4-7) to obtain intermediate migration barriers, which are represented in Fig. 4-3. It is immediately apparent from the figure that the migration energies for different jumps have more dispersed values in the FM state and are much closer in the PM state. This means that the distinction of chemical environment around the vacancy is rather reduced in the PM state compared to the FM state. This is further confirmed later in the discussion of kinetic correlation factors.

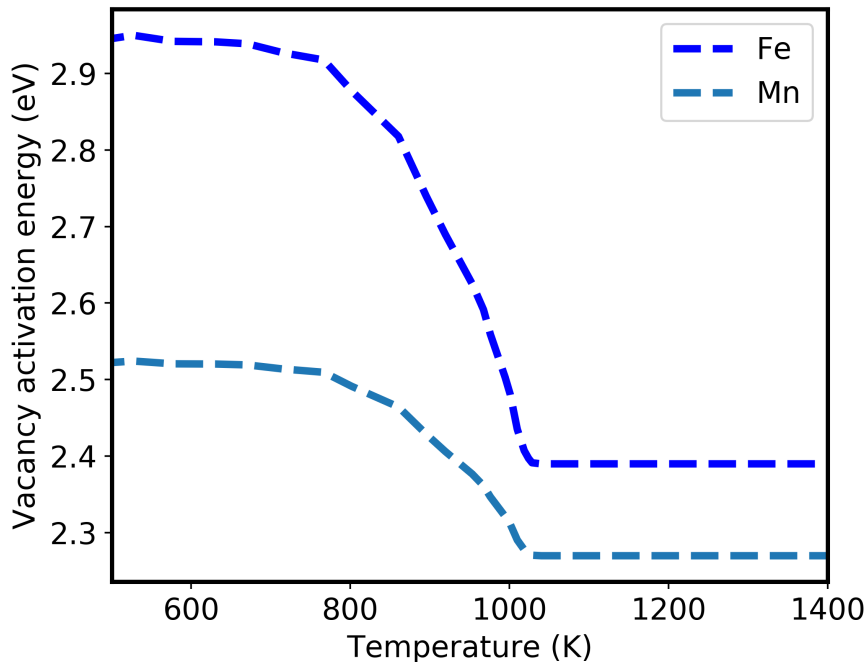


Figure 4-4: Vacancy activation energies for pure Fe and Mn in Fe.

The activation energies in the fully FM and PM states are obtained by the summation of corresponding formation and migration energies. In pure Fe, the values are 2.95 eV and 2.39 eV in the FM and PM states respectively. For the dilute FeMn system, the values are 2.53 eV and 2.27 eV in the same order. It is important to note that the activation energy difference

between the FM and PM states is remarkably reduced on the introduction of Mn solute. This difference, as will be seen in the next section, will effectively reduce the kink or acceleration in Mn diffusion coefficients relative to Fe diffusion across the Curie temperature. The profiles of activation energies are shown in Fig. 4-4. Similar to the formation and migration cases, the PM window of difference in the activation energies for Fe and Mn is much smaller than that in the FM state, indicating a dominant effect of magnetic disordering on the local chemistry around the vacancy.

4.4.2 Diffusion parameters

The self-diffusion coefficients of Fe are derived from the Ruch model (Eq. (4-1)) using activation energies in the FM and PM states. The resulting diffusion profile is presented in Fig. 4-5. The comparison of the obtained diffusion coefficients with the experimental literature shows a good agreement between DFT-SSA and experiments. The kink marks the transformation from the FM to PM state.

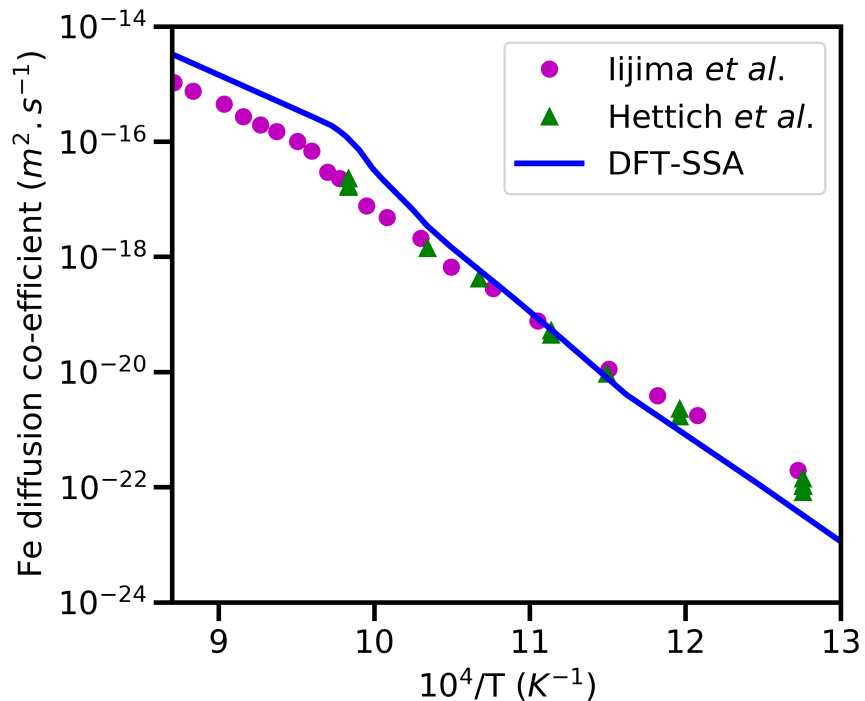


Figure 4-5: Self-diffusion coefficient in bcc Fe as a function of temperature, obtained from DFT-SSA. The experimental values from Iijima et al. [5] and Hettich et al. [6] are compared.

The Mn diffusion coefficients and their profiles are plotted in Fig. 4-6. The DFT-SSA results are compared with the EIM-MC results from the collaborators from CEA Saclay and tracer diffusion experiment results from the collaborators from the University of Münster. Overall, all the profiles are in good agreement with each other. The novelty of the DFT-SSA results lies in an accurate handling of the PM state and its atomic relaxations, but an interpolation scheme such as the Ruch model is required to fit the FM and PM activation energies. On the other hand, EIM-MC explicitly computes the diffusion coefficients at intermediate temperatures, but assumes the FM geometry for all the temperatures. Precision parallel grinding and ion-beam sputtering are used in the experiments for measuring the penetration profiles of the tracer at higher and lower temperatures, respectively. The novelty of the current experimental data is that the temperature range over which the diffusion coefficients are measured is larger than that in previous experiments. Therefore, the three different methodologies validate each other and agree well. This indicates that simpler models such as the Ruch model and Le Claire’s model give reliable results for dilute alloys, provided that accurate energies as obtained from DFT-SSA are used as model inputs.

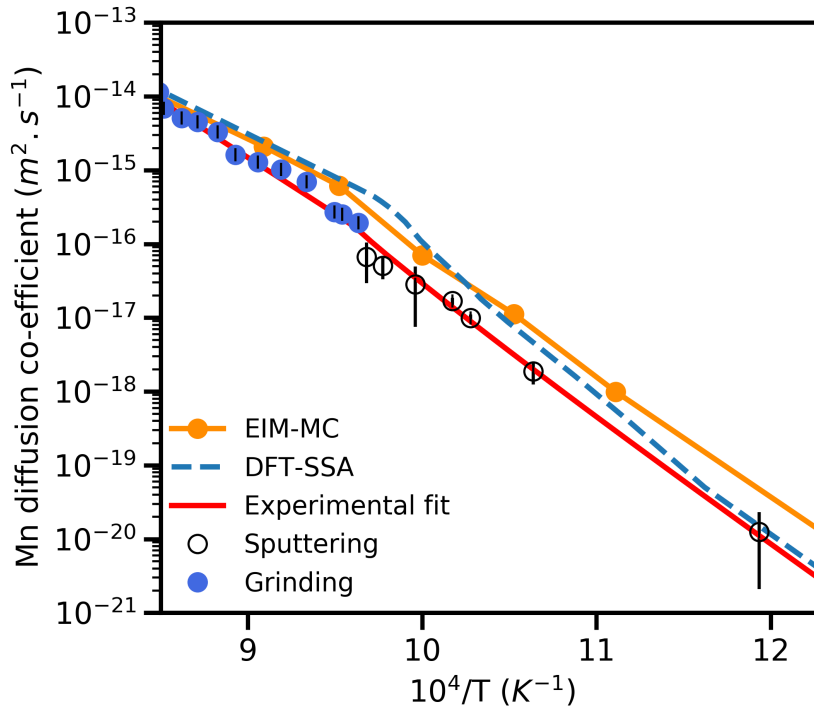


Figure 4-6: Diffusion coefficient of Mn in bcc Fe as a function of temperature, obtained from DFT-SSA, EIM-MC and experimental measurements [4]. EIM-MC are obtained by the collaborators from CEA Saclay and the experimental measurements are conducted by the collaborators from the University of Münster.

Fig. 4-7 compares the Fe and Mn diffusion coefficients obtained from DFT-SSA. From the figure, it is clear that the kink in Mn diffusion profile is remarkably reduced as compared to Fe. This is a direct consequence of the fact that the difference in activation energies of the two magnetic states is larger in the case of Fe than Mn. Such a behaviour is largely due to the difference in activation energies in the FM state, since the PM activation energies for Fe (2.39 eV) and Mn (2.27 eV) are similar and result in the PM diffusion profiles to be almost parallel. In the FM state, the Mn-vacancy binding energy is larger as compared to the PM state. As a consequence, the vacancy formation energy is much reduced in the presence of Mn. Further, the Mn migration energy (0.46 eV) is substantially smaller than the barrier in pure Fe (0.73 eV). This is because of the larger size and similar atomic mass of Mn in comparison with Fe, which favours an exchange of Mn with the vacancy more than Fe.

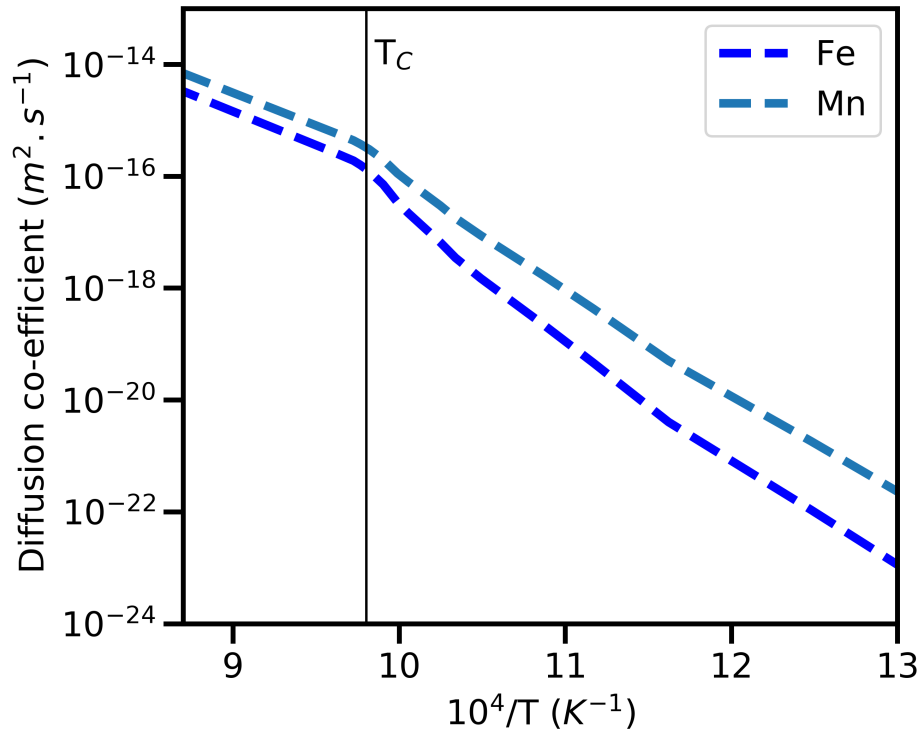


Figure 4-7: Comparison of the diffusion profiles for self-diffusion and Mn diffusion in α -Fe.

The ratio of diffusion coefficients obtained from DFT-SSA through Le Claire's model are presented along with the EIM-MC and experimental results in Fig. 4-8. In the fully PM regime, all the results are in perfect agreement, where the ratio is almost a constant and Mn diffuses about 2-3 times faster than Fe. Just below the Curie temperature, DFT-SSA

continues to be in good agreement with the experiment. At about 900 K, the DFT-SSA value (about 10) lies in between the EIM-MC (about 15) and experimental (about 5) value. For the large part, the three methodologies are in good agreement. The experimental error reduces as one moves towards higher temperatures. The ratio increases exponentially as the temperature decreases, indicating that Mn diffuses much faster than Fe in the FM state. Reiterating the point made before, the small value of the ratio in the PM state demonstrates that the magnetic disordering reduces or erases chemical distinctiveness.

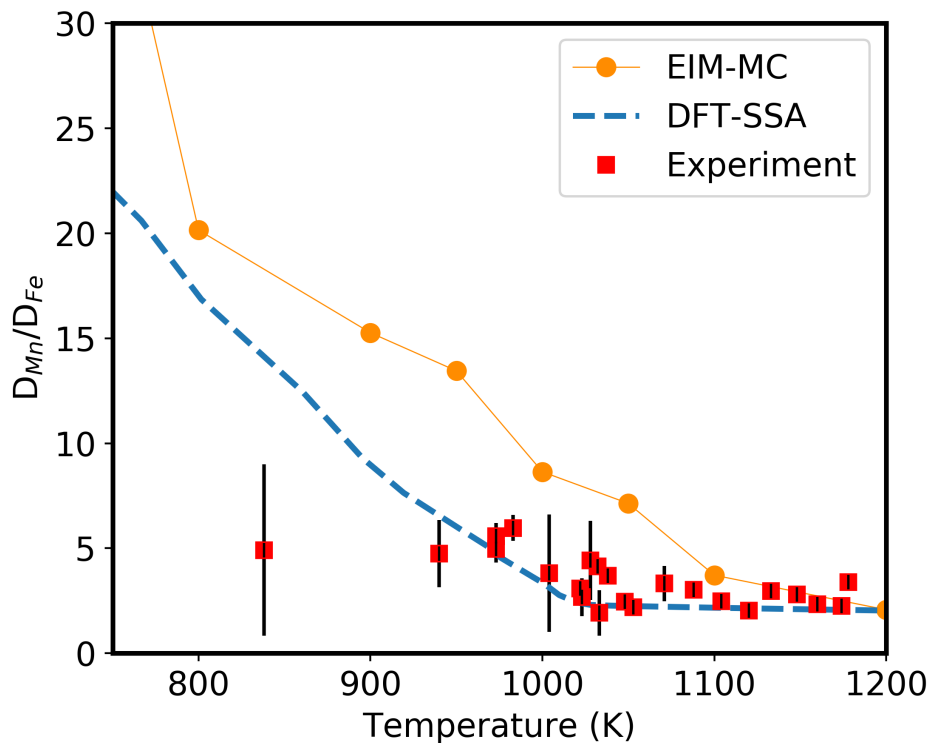


Figure 4-8: Ratio between the Mn diffusion coefficient in bcc Fe and the Fe self-diffusion coefficient [4]. The EIM-MC results are obtained by the collaborators from CEA Saclay and the experimental measurements are conducted by the collaborators from the University of Münster.

To understand the effect of magnetic disorder further, the solute (or Mn) correlation factors are studied and shown in Fig. 4-9. Since these factors are currently not possible to extract from the tracer diffusion experiments, only the DFT-SSA and EIM-MC results are presented. When only FM barriers are considered even at high temperatures, the profile deviates significantly from the curve that includes proper PM considerations. This indicates that the effect of magnetic disorder is paramount at high temperatures. At low temperatures the kinetic

correlation factor approaches 0 and at high temperatures it reaches the asymptotic value of 0.7272 or the self-diffusion correlation factor (a constant for the bcc crystal structure). Here, the low values mean that the solute and vacancy jumps are highly correlated and vice-versa. Therefore, in the FM state the chemical identity is preserved whereas magnetic disordering in the PM state destroys it, resulting in random exchanges of solute and host atoms with the vacancy.

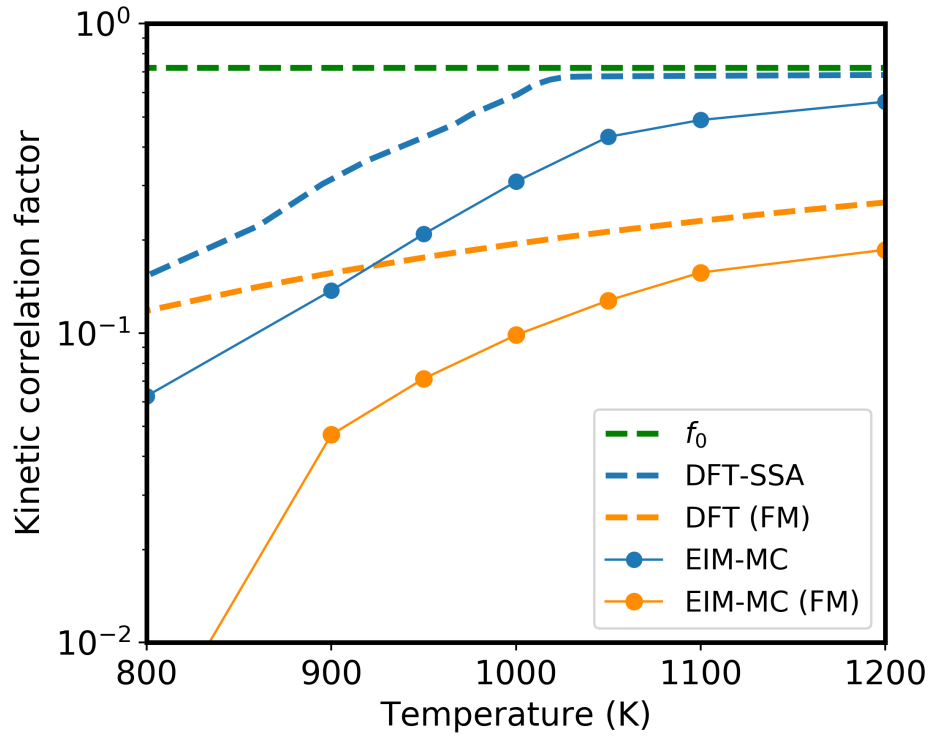


Figure 4-9: Kinetic correlation factors for Fe self-diffusion (f_0 : green line) and Mn diffusion (f_2 : blue lines) [4]. The f_2 kinetic correlation factor determined by considering only the barriers in the FM state is also displayed (orange lines) for comparison and to highlight the impact of magnetic disorder. The EIM-MC results are obtained by the collaborators from CEA Saclay.

4.5 Conclusions

The impact of magnetism on diffusion properties of the dilute FeMn system has been studied in the present chapter. In the FM state, the presence of Mn in the vicinity of the vacancy leads to an attractive binding energy and a substantially smaller migration barrier for the Mn-vacancy jump as compared to the jump in pure Fe. Magnetic disordering in the PM

state exhibits a significant influence on vacancy energetics, resulting in their reduction as compared to the values in the FM state. In addition, the energetics of vacancy, in particular migration energies for different jumps have more similar values in the PM state and are more dispersed in the FM state. This indicates that magnetic disorder dominates over chemical identities at high temperatures. This conclusion is further strengthened by the study of solute kinetic correlation factors, which reveals a clear and crucial impact of the magnetic disorder at high temperatures. The FM state exhibits a low value of the correlation factor while it reaches a high, asymptotic value with respect to the solvent correlation factor (f_0) in the PM state, indicating that the jumps are highly correlated in the FM state and are more random in the PM state.

Diffusion coefficients, which are important for practical and engineering purposes, are determined from the Ruch model and Le Claire's model with vacancy activation and migration energies obtained from DFT-SSA as model inputs. For the case of self-diffusion in Fe, good agreement with the existing experimental literature is seen. The non-Arrhenius behaviour is marked by the kink in the diffusion profile across the Curie temperature. For the Mn diffusion, excellent agreements with the tracer diffusion experiments and EIM-MC results are obtained. The Mn diffusion profile shows a reduced kink in the diffusion profile across the magnetic order-disorder transition as compared to Fe self-diffusion. This is mainly due to (i) the larger binding energy and remarkable reduction in the Mn migration barrier as compared to the pure Fe barrier in the FM state, (ii) similar activation energies for Fe and Mn diffusion in the PM state, which lead to a decrease in the difference of activation energies between the FM and PM state for the Mn case compared to Fe self-diffusion. The ratios of diffusion coefficients obtained from the Le Claire's model, which uses migration barriers obtained from DFT-SSA, is in good agreement with the experiments and EIM-MC results. Mn diffuses very fast compared to Fe in the FM state (about 20 times at 800 K) and diffuses only about twice as fast as Fe in the PM state. In general, good agreement between DFT-SSA, experiments and EIM-MC for different diffusion properties show that simpler models such as the Ruch model and Le Claire's model provide excellent results for dilute alloys if accurate energies as obtained from DFT-SSA are given as inputs. Thus, new physical insights and deeper understanding regarding vacancy mediated diffusion in the FeMn system are obtained.

5 Interplay of structure, chemistry and magnetism at FeMn grain boundaries

5.1 Introduction

Grain boundaries are an important class of extended defects that are ubiquitous and influence various physical properties of materials, such as toughness, fracture, and corrosion [122, 24, 123]. The presence of grain boundaries not only alters the local structure, but can have impact on the local chemistry via solute segregation. In turn, segregation can have impact on the mechanical properties of grain boundaries [25], and provides opportunities for grain boundary engineering [24]. For example, solute segregation is linked to grain boundary embrittlement in various materials [124, 125, 126], including steels [25]. Experimentally, in order to control the segregation and engineer the grain boundary toughness, various heat treatments are performed [24]. Different heat treatments could inadvertently result in different magnetic states in the material, demanding a thorough understanding of magnetism and the related physics.

Over the course of the present chapter, magnetism is identified and discussed as one of the important aspects in determining FeMn grain boundary energetics, such as grain boundary formation energies, Mn segregation energies, vacancy formation energies etc. Through these discussions, the complex interplay of local structure, chemistry, and magnetism are revealed. The relaxation scheme (SSA relaxations) [3] introduced in chapter 3 and applied to understand diffusion in the FeMn bulk in chapter 4 facilitates the study of such an interplay even in the magnetically disordered state. Finally, the knowledge from Mn segregation and vacancy formation is used to perform first-principles tensile tests in order to understand the impact of different situations on the grain boundary decohesion.

The chapter is organized as follows: Definitions of various energies are discussed in sec. 5.2, followed by computational details in sec. 5.3. The results concerning grain boundary formation energies, segregation energies, vacancy formation energies, a special case of magnetic states at intermediate temperatures and tensile tests are discussed in sec. 5.4, before

concluding the chapter in sec. 5.5.

5.2 Computation of grain boundary energetics

First-principles DFT provides an accurate description of grain boundary energetics. In the present section, the formulas used to describe such energies are discussed. The grain boundary formation energy (or simply termed as grain boundary energy) is given as:

$$\Delta E_{GB} = \frac{E_{GB} - E_{bulk}}{2A}. \quad (5-1)$$

Here, E_{GB} and E_{bulk} are the energies of the grain boundary and bulk supercells that have the same number of atoms. A is the area of the grain boundary plane in the given supercell. To account for two grain boundaries that exist in the supercell due to periodic boundary conditions, a factor of 2 is introduced in the denominator. It is to be noted that while the grain boundary energy for a pure system is unique for the given grain boundary structure, for systems with solutes, it depends on the solutes' substituted sites. Here, a positive value of ΔE_{GB} would mean that the grain boundary formation is an endothermic process. Since it is obvious that ΔE_{GB} refers to the formation of a grain boundary in the current chapter, the subscript is dropped for the rest of the chapter.

Even a minuscule amount of solutes at the grain boundaries can have a significant impact on the structural and mechanical properties. Therefore, it is necessary to have a quantitative measure of their segregation drive. In this regard, the segregation energies are defined as:

$$E_{seg}^{X@i} = (E_{GB}^{X@i} - E_{bulk}^X) - (E_{GB} - E_{bulk}), \quad (5-2)$$

where $E_{seg}^{X@i}$ is the segregation energy of solute X at site i of the grain boundary, $E_{GB}^{X@i}$ is the total energy of the supercell with the solute X at site i of the grain boundary and E_{bulk}^X is the total energy of the bulk supercell with the solute. Assuming that the solute X is segregated and is situated at the i -th site, the segregation energy of the next solute atom X' at j -th site is given as,

$$E_{seg}^{X'@j} = (E_{GB}^{X@i,X'@j} - E_{bulk}^{X,X'}) - (E_{GB}^{X@i} - E_{bulk}^X). \quad (5-3)$$

In order to extract the fractional occupancy of a solute atom at a grain boundary, McLean introduced a thermodynamic model [127]. This model is analogous to the Langmuir adsorp-

tion isotherm for gases, and is known as the Langmuir-McLean isotherm -

$$\frac{c_{GB}^{X@i}}{1 - c_{GB}^{X@i}} = \frac{c_{bulk}}{1 - c_{bulk}} e^{-E_{seg}^{X@i}/k_B T} . \quad (5-4)$$

$c_{GB}^{X@i}$ is the fraction of the solute at a grain boundary site i , c_{bulk} is the solute fraction in the bulk and T is the temperature. The Langmuir-McLean isotherm accounts for the configurational entropy, and assumes that the solute-solute interactions are negligible and that the segregation is parametrized by a single term E_{seg} . As a first approximation and for the purpose of the current chapter, the Langmuir-McLean model serves sufficiently well. More complex models have been developed, such as those introduced by Seah and Hondros (for ordered binary systems) [128], Fowler adsorption isotherm (solute-solute interactions) [129], Guttman isotherm (interactions for multiple co-segregation) [130].

The vacancy formation energy $E_f^{vac@i}$ at a grain boundary site i in Fe is defined as,

$$E_f^{vac@i} = E_{GB}^{vac@i} - E_{GB} + \mu_{Fe,bulk} . \quad (5-5)$$

Here, $E_{GB}^{vac@i}$ is the total energy of the grain boundary supercell with a vacancy at site i and $\mu_{Fe,bulk}$ is the chemical potential of pure Fe.

5.3 Computational details

First-principles DFT calculations are performed with SPHInX [118] using the generalized-gradient approximation (GGA) [85, 48], within the projector augmented wave (PAW) formalism [119, 120]. $\Sigma 5[001](310)$ (Fig. 5-1) is taken as the representative grain boundary for the calculations, unless otherwise specified. Supercells of 80 atoms are used for both grain boundary and bulk calculations. The optimised dimensions for the grain boundary cell are: $a = 18.483 \text{ \AA}$, $b = 8.972 \text{ \AA}$, $c = 5.674 \text{ \AA}$.

A $3 \times 6 \times 9$ k -point mesh and energy cut-off of 500 eV are used for all the calculations. The error in total energy due to the choice of these parameters is minimized to 1 meV/atom after careful convergence tests. Fermi-Dirac smearing scheme with a smearing width of 0.1 eV is chosen. The criterion for electronic convergence of the total energy is 10^{-5} eV. Structural optimization for atomic relaxations is carried out with SxExtOpt [80]. The convergence criterion for atomic forces in structural optimization is set to 0.02 eV/Å.

The ferromagnetic calculations are unconstrained (unless otherwise indicated) and param-

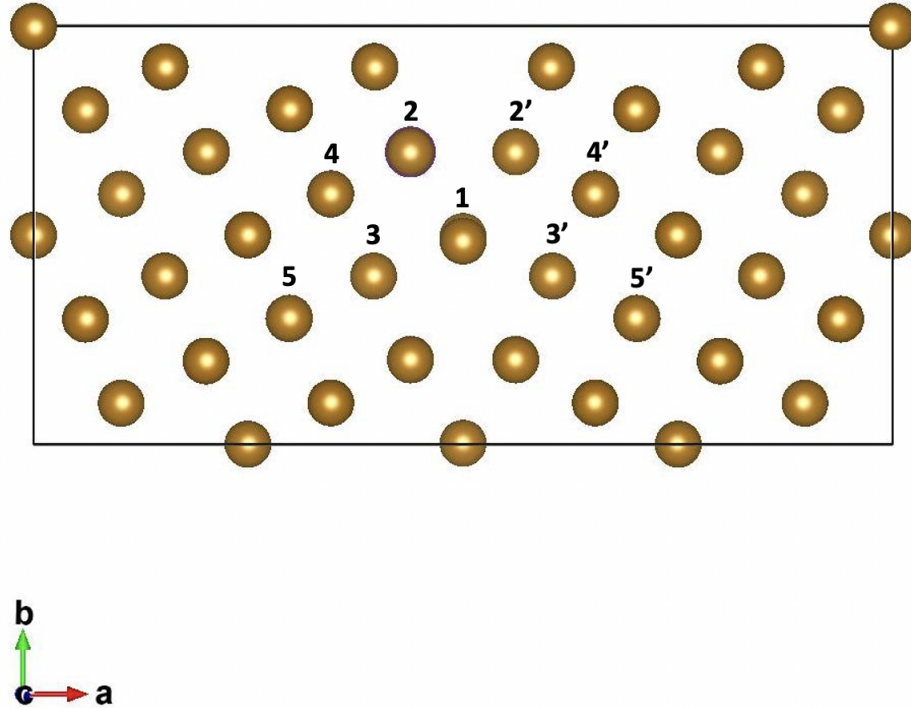


Figure 5-1: $\Sigma 5[001](310)$ grain boundary with different sites labelled. A supercell with 80 atoms is used with an additional layer in the c -axis. Only one atom in each layer (along b -axis) is labelled, since they are symmetrically equivalent to the other sites in the same layer for the given pure grain boundary.

agnetic calculations are constrained. Since the moment magnitudes change in the vicinity of the grain boundary, the optimum values are obtained by a set of constrained test calculations. For the paramagnetic grain boundary calculations, six magnetic configurations are used initially for performing SSA relaxations, i.e., for force averaging. Later, the relaxed geometry or positions obtained from the SSA relaxations are distributed over fifteen magnetic configurations to perform averaging over total energies. Such a scheme has been adopted due to the expensive nature of paramagnetic relaxations in extended defects, including grain boundaries. The averaged energies are considered for the computation of grain boundary energetics. These various random magnetic configurations are generated by special quasirandom structures (SQSs) [58] method, where the atoms with opposite moments are distributed randomly by minimizing the correlations (described in the Theoretical Methods chapter). Different configurations can be generated by varying the cluster sizes for minimizing correlations. Thus, the randomness in each structure can be regarded as of good quality.

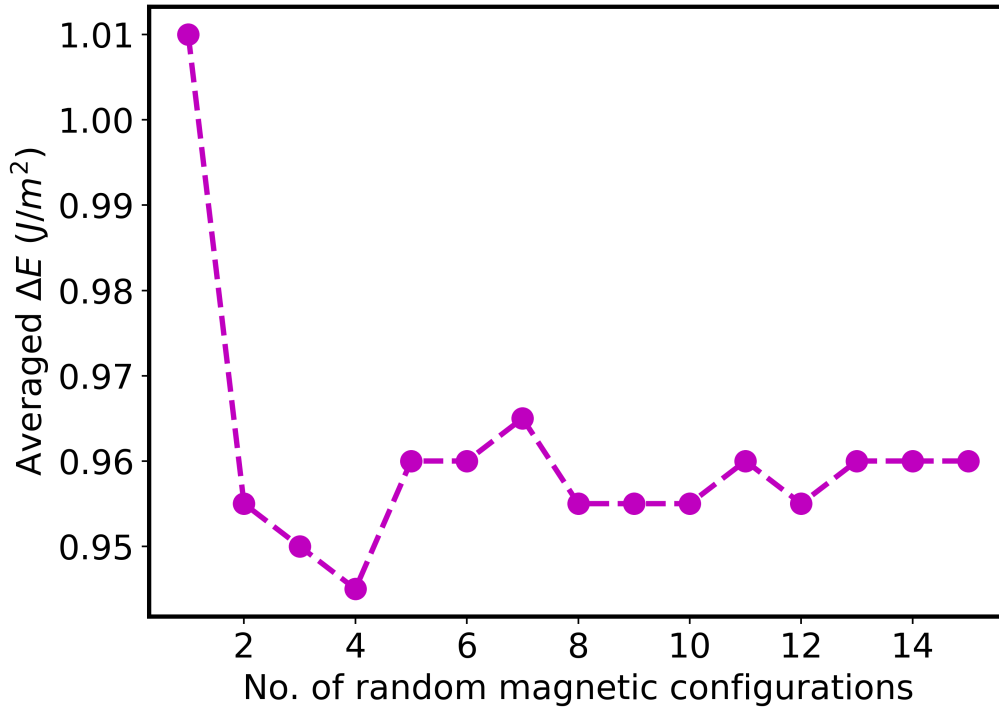


Figure 5-2: Convergence of averaged grain boundary ($\Sigma 5[001](310)$) energy in the paramagnetic state with respect to the number of random magnetic configurations.

The convergence of paramagnetic grain boundary energies for pure Fe with respect to the number of random magnetic configurations (or SQSs) is presented in Fig. 5-2. The y -axis represents grain boundary energy that is averaged over the corresponding number of configurations given in the x -axis. Clearly, the grain boundary energy lies in a small window of $\approx 0.01 J/m^2$ from about 8 magnetic configurations, and a total of 15 configurations is taken to confirm convergence. This is because the symmetries of the system are further reduced on incorporating Mn solutes or a vacancy, and a slightly larger number of configurations will ensure the convergence of paramagnetic energies.

5.4 Results and discussion

The results are presented and discussed in the present section. In the ferromagnetic bulk, Fe atoms have a magnetic moment of $2.20 \mu_B$, whereas the Fe atoms at the grain boundary layer (i.e., at site 1 and equivalent sites in Fig. 5-1) possess a moment of $2.53 \mu_B$. The larger volume at the grain boundary site results in the increase of the moment size. As shown in Fig. 5-3, the magnitude of the moments are $2.08 \mu_B$ in the paramagnetic bulk, and $2.30 \mu_B$

at the grain boundary layer.

A single Mn solute in the ferromagnetic bulk couples antiferromagnetically with the Fe atoms with a moment of $-2.05 \mu_B$. It is known that Mn in Fe bulk has a local energy minimum for the ferromagnetic coupling, with only a small difference in energy compared to the antiferromagnetic global minimum [18]. Therefore, the initial conditions specified in the calculation run can determine the final moment for Mn, and a careful set up is needed to achieve the convergence to the global minimum. At the grain boundary in the ferromagnetic state, Mn strongly couples antiferromagnetically to Fe, with a larger moment of $-3.10 \mu_B$. In the paramagnetic bulk, Mn attains a moment magnitude of $1.80 \mu_B$, and $2.60 \mu_B$ at the grain boundary layer. Therefore, for both the magnetic states, the change in Mn magnetic moment is larger than the Fe moment. Further, it is to be noted that the changes in moment magnitudes from the bulk to the grain boundary are similar for the ferromagnetic and paramagnetic states.

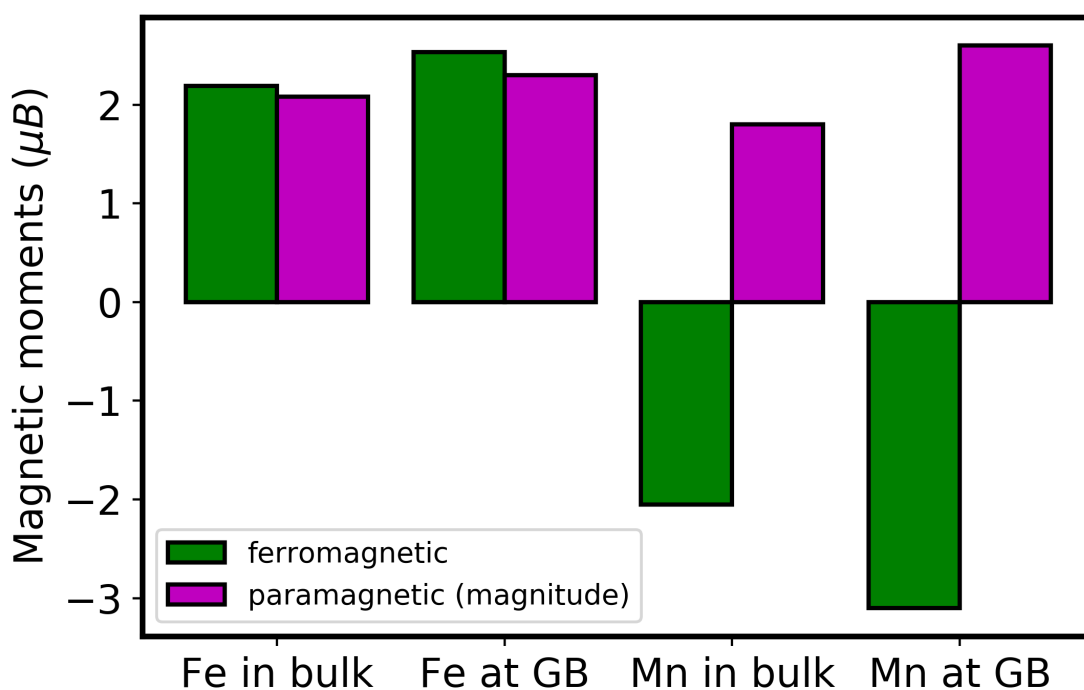


Figure 5-3: Magnetic moments of Fe and Mn in bcc Fe bulk and grain boundary, for the ferromagnetic and paramagnetic states. For the paramagnetic state, only the magnitudes of moments are considered.

The antiferromagnetic coupling of Mn in the Fe bulk and grain boundary is also evident from the resolved local density-of-states (DOS), shown in Fig. 5-4. In the figure, the DOS

for the Mn solute atom and its nearest neighbour Fe atom are shown. Clearly, for Mn in the bulk, the majority spin state is down-spin state, since larger number of states are occupied in the down-spin region below the Fermi level [131, 132]. On the other hand, Fe atom exhibits up-spin state as the majority spin state. Further, broad peaks are observed between -4 eV to -2 eV in the down-spin state for Mn, suggesting the localisation of *d*-electrons in the majority spin (or down-spin in this case) state. These features arise from an antiferromagnetic coupling of Mn atom in Fe bulk shown in Fig. 5-3. ’

At the grain boundary, the local DOS for Mn is significantly different than that in the bulk. As can be seen in Fig. 5-4, the broader peak that is present around -4 eV in the bulk becomes sharper at the grain boundary. Also, the peak height is larger for Mn atom at the grain boundary. In addition, a sharp peak that is present in the bulk above the Fermi level reduces in height for the grain boundary Mn atom. All these observations suggest an even stronger antiferromagnetic coupling of a Mn atom at the grain boundary with a larger moment magnitude.

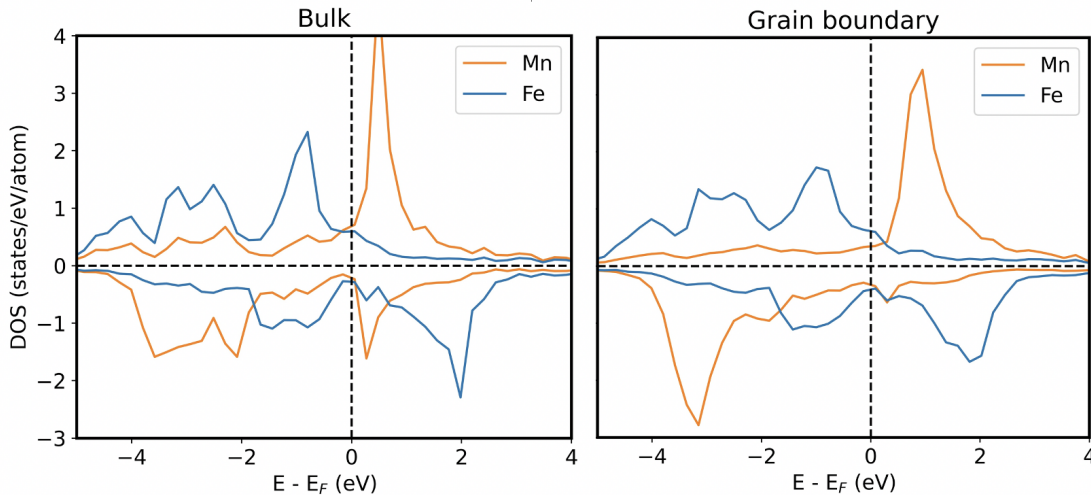


Figure 5-4: Local density-of-states (DOS) of a Mn atom in the bulk and grain boundary, along with the DOS of its nearest neighbour Fe atom. The Fermi energy is shifted to 0 eV.

5.4.1 Grain boundary formation energies

The grain boundary energies quantify the ease of formation of grain boundaries. They are calculated according to Eq. 5-1 and are shown in Fig. 5-5. The grain boundary energy in the

ferromagnetic state is calculated to be 1.57 J/m^2 and agrees well with the literature values [133]. The presence of Mn at the grain boundary (site 1 in Fig. 5-1, 25% coverage for the considered supercell) reduces the grain boundary energy to 1.50 J/m^2 . On the other hand, the impact of the paramagnetic state is remarkable as seen in Fig. 5-5: the grain boundary energy in pure Fe is 0.96 J/m^2 and is smaller than the ferromagnetic state by 0.61 J/m^2 . While a theoretical computation in the paramagnetic state is not present in the literature, an experimental estimation of grain boundary energies as a function of temperature has been carried out by Geise et al [8]. In these experiments, bulk diffusion and grain boundary diffusion coefficients were used to calculate grain boundary energies via a semi-empirical formula given by Gupta et al., [134] and Borisov et al [9]. These experimental values are given in Tab. 5-1. The samples were polycrystals of pure Fe, hence a direct quantitative comparison is not possible. However, similar to the theoretical prediction, the grain boundary energy reduces with increasing temperature, and attains a value of about 0.98 J/m^2 for the pure sample above the Curie temperature, indicating a strong impact of magnetism on grain boundary energies.

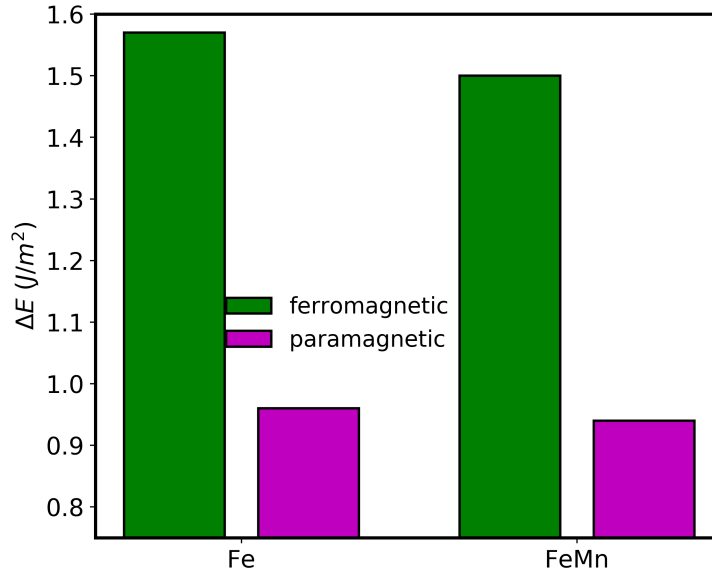


Figure 5-5: Grain boundary energies for pure Fe and Mn segregated Fe grain boundaries, in both the ferromagnetic and paramagnetic states.

On substituting a Mn atom at the grain boundary layer (25% coverage for the considered supercell) in the paramagnetic state, the grain boundary energy reduces slightly to 0.94 J/m^2 , i.e., by 0.02 J/m^2 compared to the pure Fe case. It is interesting to note that for both the pure Fe and FeMn systems, the difference in the total energies between the ferromagnetic

and paramagnetic grain boundary supercells is much smaller than the difference between the bulk supercells.

T (K)	pure	less pure
766	1.18	1.07
905	1.13	1.09
1005	1.06	1.05
1092	0.98	0.98

Table 5-1: Experimental grain boundary energies (in J/m^2) estimated by Geise et al [8] from the diffusion data in α -Fe, using a semi-empirical approach of Borisov et al. [9].

Starting from the ferromagnetic state in pure Fe, the gradual decrease of grain boundary energy with the magnetic disorder growing outwards from the grain boundary layer, i.e., layer with site 1 in Fig. 5-1, can be seen in Fig. 5-6. Such a figure helps in understanding the stepwise impact of paramagnetism on the grain boundary energy. Clearly, more than half the reduction of the grain boundary energy in going from the fully ferromagnetic state to fully paramagnetic state, i.e., $0.61 \text{ J}/\text{m}^2$, already occurs when the first 20% of the system (layers next to and including the grain boundary) is magnetically disordered. Therefore, unsurprisingly, the disordering of the immediate layers around the grain boundary has the maximum impact on grain boundary energy.

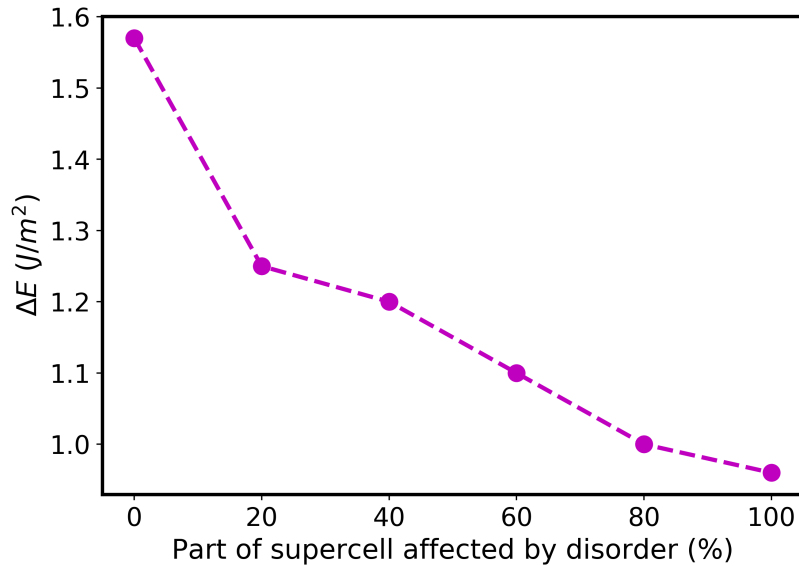


Figure 5-6: Change in grain boundary energy with increasing magnetic disorder in the supercell, starting from the grain boundary layer until it covers the entire supercell.

5.4.2 Mn segregation energies

The segregation behaviour of solutes can have a drastic influence on the mechanical properties of materials. In order to understand the dependence of the Mn segregation on the low- and high-temperature magnetic states, segregation energies are discussed in this section. These segregation energies are calculated according to Eqns. 5-2 and are presented in Fig. 5-7.

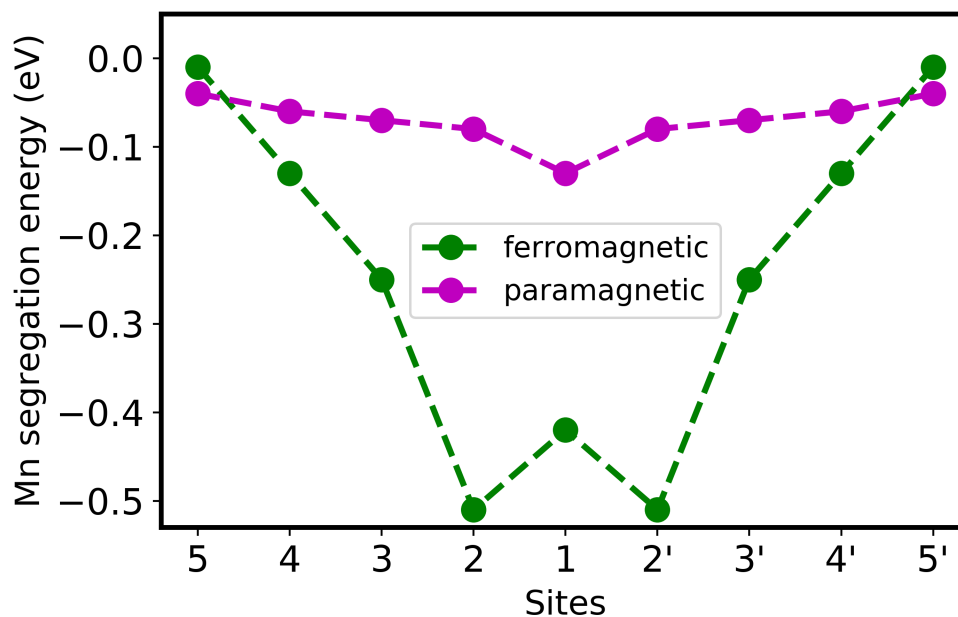


Figure 5-7: Mn segregation energies with respect to different sites (labelled in Fig. 5-1) in the grain boundary supercell, for the ferromagnetic and paramagnetic states.

The segregation profile for the ferromagnetic state is discussed first. The segregation energy at a site in the grain boundary layer (i.e., at site 1 in Fig. 5-1) is -0.42 eV, which is large. Here, the negative sign refers to attractive interaction. The drive for segregation is even stronger for the sites in the layers immediately next to the grain boundary, where the segregation energy is -0.51 eV. It is interesting to note that though the Voronoi volume is larger for the grain boundary sites, segregation is more favourable for the next layer. As discussed in the previous chapter, Mn diffuses very fast relative to Fe in bulk. Therefore, the segregation of Mn from bulk to the grain boundary is kinetically favourable, too. The segregation energy decreases sharply further away from this layer and is almost 0 for the layer with site 5, which can therefore be considered as bulk-like.

A hypothesis as to why the layer next to the grain boundary is more attractive for Mn can be based on arguments regarding magnetism. The sites in this layer (such as site 2 in Fig. 5-1) have very closely situated nearest neighbours (site 2') at a distance of about 2.27 Å (lattice parameter = 2.83 Å). Therefore, the presence of two strongly ferromagnetic atoms at these two sites that are at a short distance from each other could lead to magnetic frustrations. Thus, the presence of an atom like Mn that exhibits strong antiferromagnetic (AFM) coupling could reduce these frustrations. To further probe this hypothesis, since a direct investigation of magnetic pair interaction parameters is not straightforward for structures such as grain boundaries, an indirect study of the effective magnetic interaction parameter is presented in Fig. 5-8. By flipping the spin of Fe atom (AFM Fe) at different sites in pure Fe grain boundary, one can take the difference of the supercell energies with and without the spin flip ($E_{down} - E_{up}$). Such a difference is proportional to the effective interaction parameter (J_{eff}) and will be called so for the present. To avoid the atomic spin reverting back to the ground state during the calculation run, the spins are constrained to the magnitudes exactly equal to those in the completely spin-up state. The difference (or the effective parameter) is large in the bulk, i.e., about 0.84 eV, indicating that including a Fe atom with spin-down state is highly unfavourable. This is expected, since bulk bcc Fe is a strongly ferromagnetic system. For the grain boundary sites, the profile shown in Fig. 5-8 is interesting.

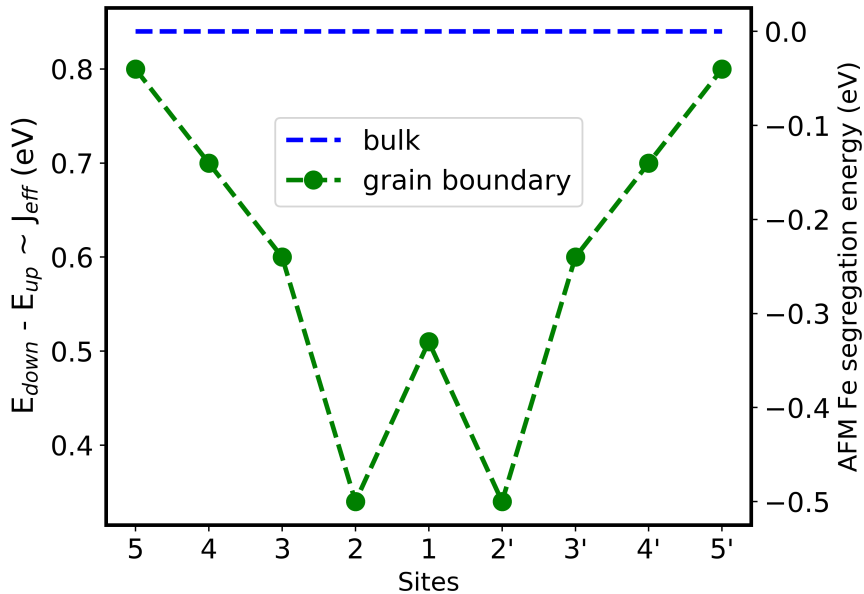


Figure 5-8: Effective magnetic interaction parameters at different sites (labelled in Fig. 5-1) in the grain boundary supercell, for the ferromagnetic Fe system. Segregation energies of AFM Fe atom is shown in the second y -axis.

For the site 1 in the grain boundary layer, the effective parameter is much smaller than the bulk value, about 0.51 eV. The smallest value is for the site in the layer next to the grain boundary layer, which is 0.34 eV. This strengthens the hypothesis that the presence of an atom with spin-down state could relieve the possible frustrations due to closely located ferromagnetic atoms. In fact, the entire profile looks similar to the Mn segregation profile qualitatively. Quantitatively too, if we consider the segregation energy of the AFM Fe atom that can be obtained taking the difference of grain boundary $E_{down}-E_{up}$ values and the bulk counterpart, the values are similar to the Mn segregation energies (Fig. 5-8). Towards the site 5, the effective parameter almost attains the bulk value.

The paramagnetic segregation profile in Fig. 5-7 is remarkably different to the ferromagnetic profile. The energies are considerably smaller in magnitude compared to the ferromagnetic state, indicating that the segregation drive is reduced on transition to the magnetically disordered state. Unlike the ferromagnetic case, the segregation tendency in the paramagnetic state is largest for the grain boundary site 1, where the segregation energy is -0.13 eV. It is to be noted that the layer next to the grain boundary is not the most favourable, since the moments are disordered by default and Mn moment is not special as in the ferromagnetic case. Segregation energy gradually reduces away from the grain boundary layer and becomes almost 0 for the fifth layer, similar to the ferromagnetic case.

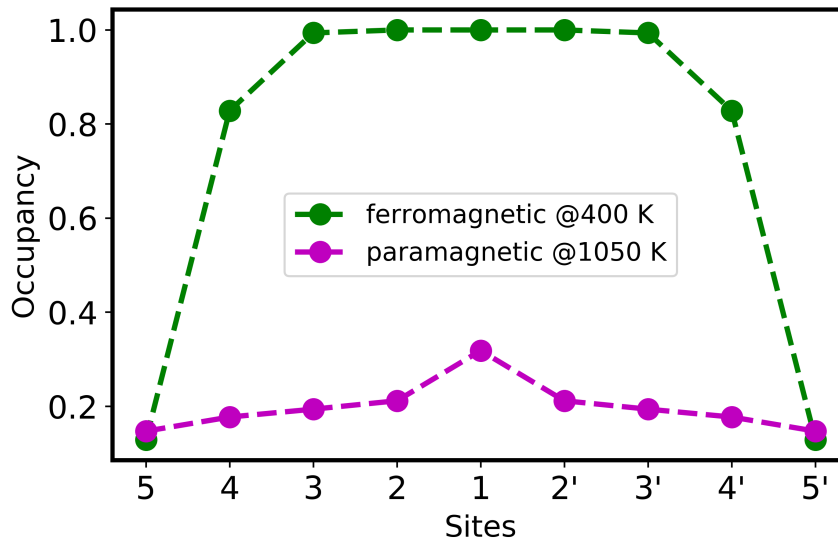


Figure 5-9: Mn occupancies at different sites (labelled in Fig. 5-1) in the grain boundary supercell, calculated using the ferromagnetic and paramagnetic segregation energies assuming 10% Mn composition in the bulk.

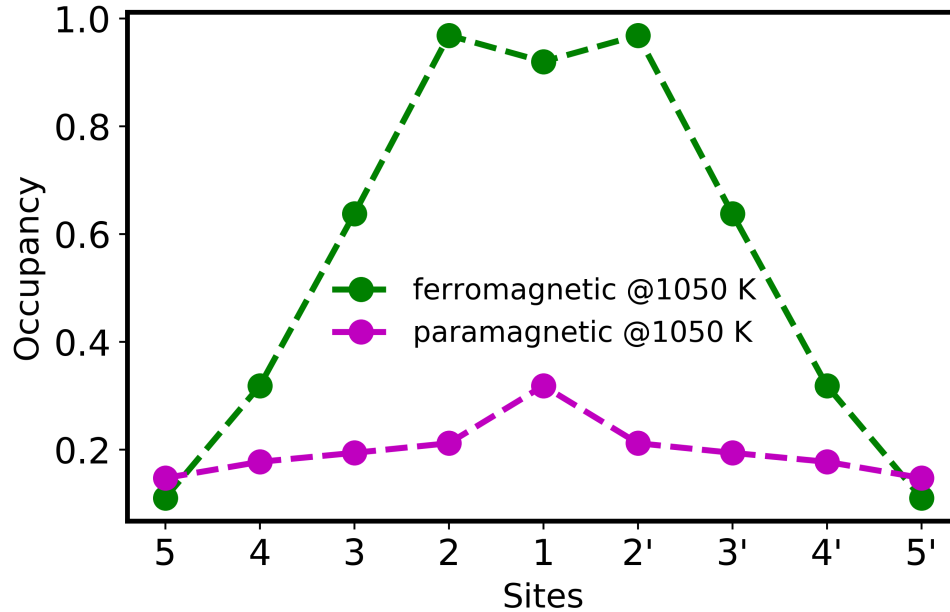


Figure 5-10: Mn occupancies at different sites (labelled in Fig. 5-1) in the grain boundary supercell, calculated using the ferromagnetic and paramagnetic segregation energies for the same temperature (1050 K) assuming 10% Mn composition in the bulk.

The occupancy of Mn at different sites can be extracted using the corresponding segregation energies for the ferromagnetic and paramagnetic states via McLean's model as given in Eq. (5-4), for the given bulk composition and temperature. Assuming 10% Mn composition in the bulk, which is relevant for many existing experimental works [24, 123, 25], the occupancy profile at two different temperatures pertinent to the ferromagnetic and paramagnetic states are calculated and presented in Fig. 5-9. Sites in the first three layers are completely occupied by Mn in the ferromagnetic state at 400 K, while the occupancy beyond the third layer reduces sharply and is nearly zero for the fifth layer. For the paramagnetic state at 1050 K, the occupancy at a site in the grain boundary layer is around 0.3 and decreases gradually as one moves away from the grain boundary layer. It is important to calculate the occupancy for the temperatures relevant for the paramagnetic state using paramagnetic segregation energies, since using ferromagnetic segregation energies can give substantially different occupancies for these temperatures. For example, occupancies obtained for the same temperature (1050 K) using the ferromagnetic and paramagnetic segregation energies differ significantly as shown in Fig. 5-10. In this case, the ferromagnetic segregation energies substantially overestimate the occupancies compared to the paramagnetic state. Therefore, entropic arguments alone do not provide a complete understanding. The reduction in the Mn

composition in the grain boundary at higher temperatures has also been reported in atom probe tomography (APT) experiments [25], which emphasizes the importance of proper paramagnetic energy considerations. To obtain the Mn concentration at the grain boundary in the paramagnetic state experimentally, the material can be quenched from paramagnetic temperatures such that the Mn concentration is frozen in and can be measured by APT.

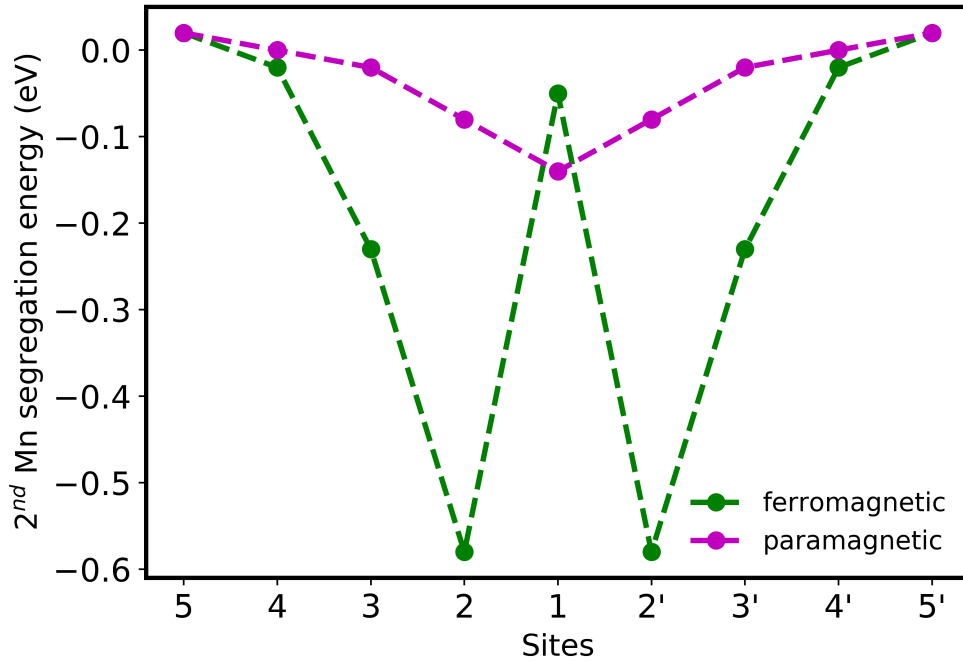


Figure 5-11: Segregation energies for the second Mn atom when a Mn atom is located at the grain boundary layer (site 1 in Fig. 5-1), for the ferromagnetic and paramagnetic states.

To understand how the Mn-Mn interactions at the grain boundary influence the segregation behaviour, segregation energies are calculated for the second Mn atom when the first Mn atom is located at site 1 in the grain boundary layer (Fig. 5-1). These energies are calculated according to Eq. (5-3) and the results are presented in Fig. 5-11. From the figure, the segregation energy for the second Mn atom at a nearest neighbour site in the grain boundary layer (i.e., along \mathbf{c} -axis in Fig. 5-1) in the ferromagnetic state is much smaller in magnitude (-0.05 eV) compared to when only one Mn atom is present (-0.42 eV), probably due to Mn-Mn repulsion when both the Mn atoms are located in the same layer. On the other hand, the segregation drive is even larger for the nearest neighbour site in the layer next to the grain boundary in comparison with the single Mn atom. In fact, this is the most favourable geometry for the grain boundary system with two Mn atoms, more so than the

case where both the Mn atoms are present in the layer (at two nearest neighbour sites in this layer) next to the grain boundary. For the next layers, segregation energies are similar to those for the single Mn atom.

In the paramagnetic state, the segregation profile for the second Mn atom is very similar to the single Mn atom case both qualitatively and quantitatively, with the grain boundary layer being the most favourable for both the Mn atoms. Therefore, the Mn-Mn interaction can be assumed to be negligible, leading to a similar conclusion as the one that was drafted in the last chapter: magnetic disordering dominates chemical interactions and erases their effects.

The Curie temperature marks the transition from the ferromagnetic state to the paramagnetic state. While the Curie temperature for the bulk bcc Fe is well-known (1043 K), the question arises as to whether the formation of a grain boundary leads to a different Curie temperature locally. However, a direct computation of Curie temperatures for such defect systems is not trivial. Since the paramagnetic energies obtained from SSA relaxations are highly accurate, these energies are used to extract Curie temperatures through the mean-field definition:

$$T_C = \frac{2}{3} \times \frac{(E_{FM} - E_{PM})}{Nk_B}, \quad (5-6)$$

where E_{FM} and E_{PM} are the supercell energies in the ferromagnetic and paramagnetic states respectively, N is the number of atoms in the supercell and k_B is the Boltzmann constant. It is known that the mean-field definition overestimates the Curie temperature in systems such as bcc Fe. Since the true Curie temperature is known for bcc Fe, all the obtained Curie temperatures in the following are rescaled by a factor accordingly. Curie temperatures obtained from the mean-field model and the corresponding rescaled values are presented in Fig. 5-12 as a function of Mn composition, for both the bulk and grain boundary systems. The calculated values are fitted with a linear fit.

In the bulk, the Curie temperature decreases at the rate of 20 K per Mn %. This slope lies within the values reported in the literature (10 K per Mn % [135], 43 K per Mn % [136]). The grain boundary Curie temperatures are remarkably different and smaller than the bulk values. Even for pure Fe, a difference of around 240 K is observed, with the rescaled grain boundary Curie temperature being 802 K. The Curie temperature for the grain boundary further decreases with the addition of Mn at the rate of 12 K per %. This indicates that there exists a temperature window where the bulk is in the ferromagnetic state (Curie temperature being much higher) and the area around the grain boundary is in the paramagnetic state

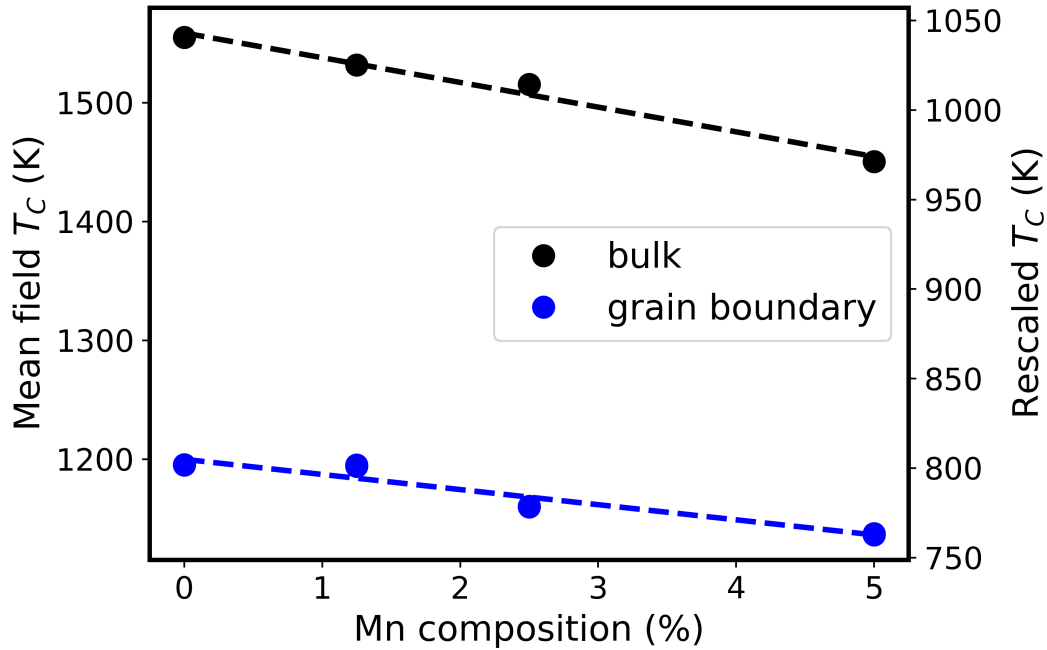


Figure 5-12: Mean-field Curie temperatures as a function of Mn composition, for both the bulk and grain boundary systems.

(Curie temperature being lower). For example, for the pure Fe, the range is between 802 K to 1043 K. Below 802 K, both the bulk and grain boundary are in the ferromagnetic state, and both are in the paramagnetic state above 1043 K. The figure is an excellent example to showcase the structural, chemical, and magnetic interplay at the grain boundaries. Here, the structural transformation, i.e., the formation of grain boundaries remarkably affects the magnetic order-disorder transition temperature. Simultaneously, the local chemistry, i.e., Mn composition influences the Curie temperature, too. In the earlier discussions, a significant impact of the magnetic states on the grain boundary energies and Mn segregation energies are observed. On the other hand, in the present discussion, local structure and chemistry are seen to influence the Curie temperature, and hence the local magnetic state. The change in the local magnetic state further influences segregation, and so on, revealing an astonishing interplay of magnetism, chemistry and structure.

The segregation energies and site occupation values discussed earlier correspond to such cases, where both the bulk and grain boundary have the same magnetic state, i.e., either in the very low temperature limit or very high temperature limit. Since the intermediate temperature window implies simultaneous presence of the paramagnetic state in the grain boundary and ferromagnetic state in the bulk, the corresponding segregation energies are

calculated by substituting ferromagnetic bulk supercell energies and paramagnetic grain boundary energies in Eq. (5-2). The resulting segregation energies and occupation values are presented in Fig. 5-13. Since the layers including and immediately next to the grain boundary are of interest, segregation energies are calculated for these layers, and the ferromagnetic bulk is assumed to begin from the fifth layer on either side of the grain boundary layer. It is clear from both the segregation and occupancy profiles that this special case lies in between the limiting cases. However, the segregation drive is much stronger than the case where both the bulk and grain boundary are in the paramagnetic state.

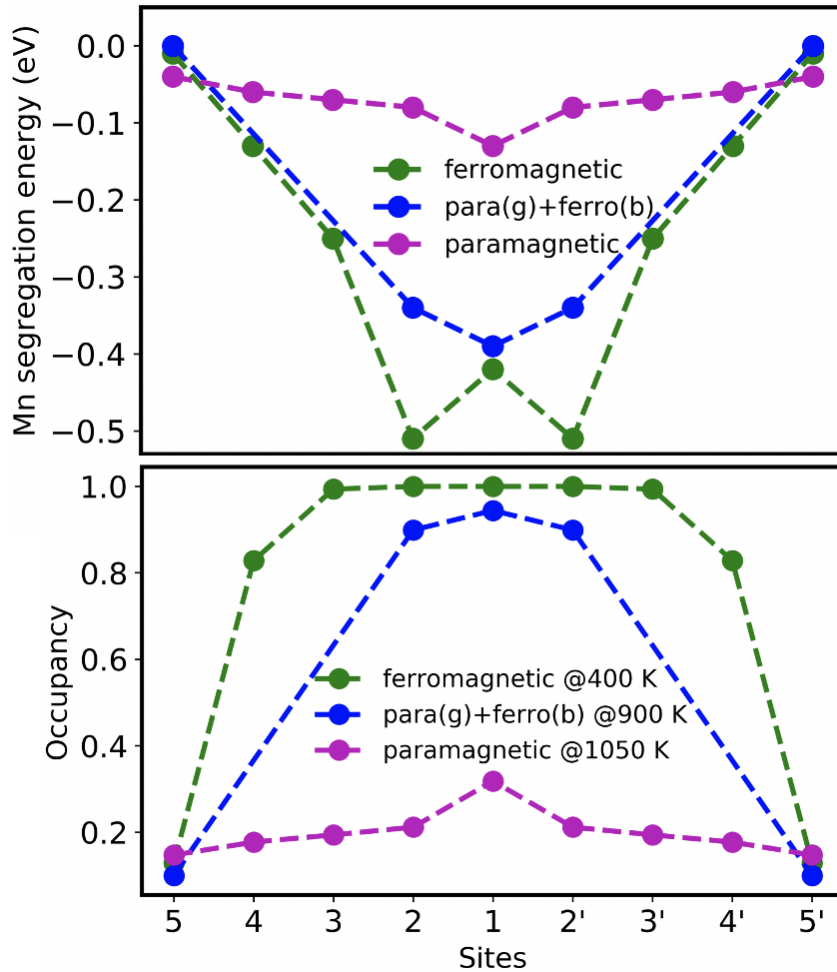


Figure 5-13: Segregation energies and occupancies for the case with the grain boundary in the paramagnetic state and the bulk in the ferromagnetic state. The other two limits are also shown for comparison.

5.4.3 Vacancy at the grain boundary

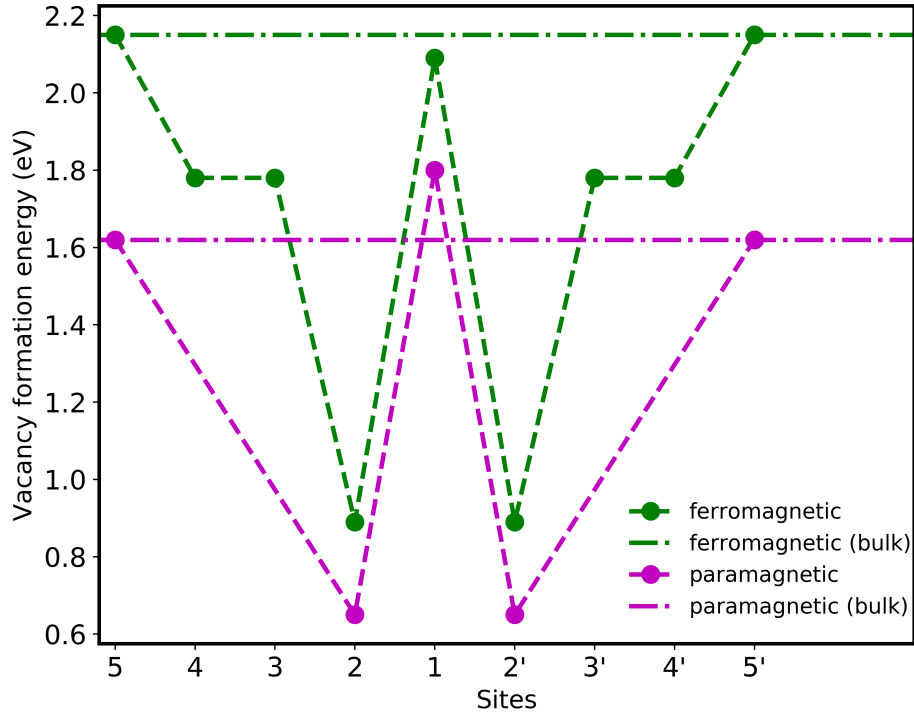


Figure 5-14: Vacancy formation energies at different grain boundary sites, for the ferromagnetic and paramagnetic states. Bulk values (dashed-dot lines) have been added for the reference.

The formation of vacancies in the vicinity of grain boundaries can have a drastic impact on the mechanical properties. Experimentally, it has been speculated that the vacancies could accelerate the grain boundary decohesion [25], ultimately leading to the fracture of the material. Moreover, vacancies are crucial for understanding kinetics of segregation. Therefore, insights about vacancy formation energies will be relevant in this regard. These energies are calculated according to Eq. (5-5) and the results are plotted in Fig. 5-14. As presented in chapter 2, the vacancy formation energies in bulk Fe are 2.15 eV and 1.62 eV for the ferromagnetic and paramagnetic states respectively, for the equilibrium lattice constant of 2.83 Å. In the ferromagnetic state, the formation energy at site 1 in the grain boundary layer is almost the same as that in the bulk. However, a drastic reduction in the vacancy formation energy is observed for the layer next to the grain boundary, qualitatively similar to the segregation profile. The vacancy formation energy in this layer is 0.89 eV, which is more than 1 eV smaller than the bulk value. The smaller formation energy indicates that this layer could act like a sink for vacancies. The formation energy is relatively much larger

for the third layer, i.e., about 1.77 eV, and is similar for the fourth layer. The bulk value is attained in the fifth layer, similar to the segregation profiles.

In the paramagnetic state, the vacancy formation energy in the grain boundary layer is slightly larger than the bulk value. However, similar to the ferromagnetic state, the next layer is the most favourable for vacancy formation with the formation energy of 0.65 eV. This is lower than the ferromagnetic counterpart, therefore this layer can be regarded as a better vacancy sink. Since these calculations are highly expensive and the profile after the second layer is similar for various cases that are discussed previously, separate calculations have not been carried out except for the fifth layer. Again, the vacancy formation energy at site 5 (in Fig. 5-1) in the fifth layer is the same as in the bulk.

5.4.4 Grain boundary decohesion

Mn is known to cause grain boundary embrittlement and fracture in steels [24, 25, 137]. Having understood that Mn segregation is thermodynamically favourable in the previous sections, finally the extent of its effect on grain boundary decohesion, based on local geometry and chemistry is studied in this section. Moreover, as discussed in the last section, it is also important to understand the impact of vacancies on decohesion since Mn-vacancy pairs have been speculated to significantly contribute to the fracture in experiments [24, 25]. While the fracture of Mn decorated grain boundaries in steels have been observed experimentally [24, 25], Ito et al., [137] have theoretically studied twin boundary decohesion by Mn in bcc Fe. In this study, a single Mn atom at the grain boundary layer in the ferromagnetic state was considered. A more complex study of the impact of Mn at different sites, larger concentration, vacancies and vacancy-Mn pairs is missing in the literature. The present section attempts to address these issues. It is to be noted that all the results presented in this section concern the ferromagnetic state, since tensile test calculations are highly expensive even for the magnetically ordered state. Full-fledged magnetically disordered calculations are extremely time consuming and are omitted for the current study. However, comments on the transferability of the ferromagnetic results to the paramagnetic state are made wherever possible.

The tensile tests are performed by increasing the uniform, uniaxial strain in the [310] direction normal to the grain boundary plane (or along **a** in Fig. 5-1), until the grain boundary fractures. Strain is defined as the change in the cell length divided by the equilibrium cell length (i.e., $\Delta a/a$). Energies at each strain are calculated and the stress at each strain is calculated by taking the difference of these energies and dividing by the corresponding change

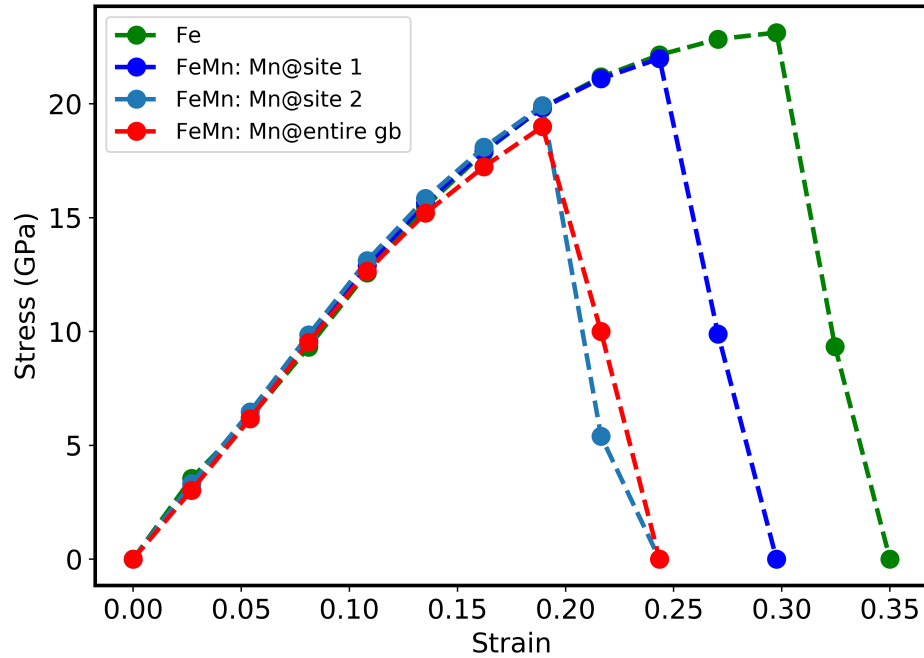


Figure 5-15: Stress-strain curves obtained from first-principles tensile tests for pure Fe (green dashed line), Mn substituted at site 1 covering 25% of the grain boundary layer or layer 1 (blue dashed line), Mn at site 2 covering 25% of the layer next to the grain boundary layer (light blue dashed line) and when the entire grain boundary layer is covered by Mn (red dashed line).

in volume of the cell, via the centered-difference method. The resulting stress-strain curves when a Mn atom is situated at site 1 (25% coverage of layer 1 or grain boundary layer), at site 2 (25% coverage of the layer next to grain boundary layer), when the entire grain boundary layer is covered with Mn (100% coverage of the grain boundary layer in Fig. 5-1) and for the pure Fe case are presented in Fig. 5-15. The system size and periodic boundary conditions inhibit the emission of dislocations and thereby curb plasticity. Due to this, the stress values are artificially high [138]. On the other hand, such a set-up allows to capture purely the impact of Mn (or vacancy, studied later) on grain boundary decohesion. The pure Fe grain boundary fractures when the strain is around 30%. Substituting Mn at site 1 (25% coverage of the grain boundary layer) significantly reduces the fracture strain to about 24%, already indicating that Mn embrittles the grain boundary. Mn embrittlement ability is even more severe at site 2, in the layer next to the grain boundary layer (25% coverage of this layer). Here, the fracture strain reduces to 19% and the stress corresponding to the fracture (fracture stress) reduces too. As discussed in the last section, site 2 is the most favourable for Mn segregation. To understand the stress-strain behaviour for a larger Mn concentration,

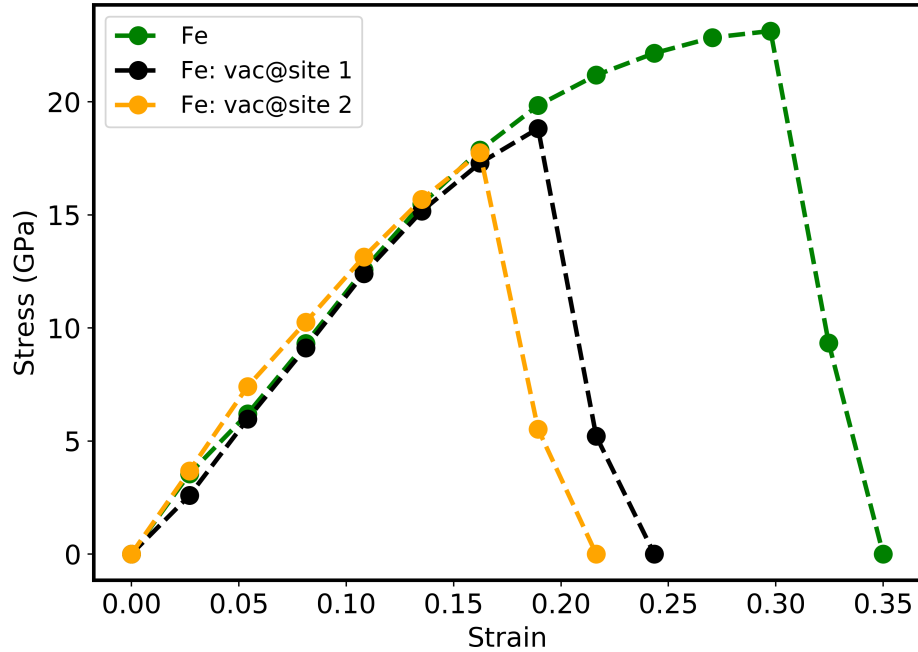


Figure 5-16: Stress-strain curves for the Fe grain boundary with a vacancy in site 1 (black dashed line), site 2 (yellow dashed line). The case of pure Fe without any vacancy has been added for reference.

the entire grain boundary is covered with Mn (100% coverage of the grain boundary layer). For this case, the fracture strain is smaller than when a single Mn atom is located at site 1 (25% coverage of the grain boundary layer), but is the same as when a single Mn atom is located at site 2 with a slightly smaller fracture stress.

In Fig. 5-16, the stress-strain curves for the vacancy at site 1 and site 2 are shown, the latter being the most favourable for vacancy formation. The presence of vacancy at these sites has even larger impact on the grain boundary fracture as compared to Mn at corresponding sites, as shown in Fig. 5-16. The fracture strain is about 19% for the vacancy at site 1, showing a strong impact on the grain boundary decohesion. Similar to Mn, the presence of vacancy at site 2 is even more detrimental to the grain boundary, with the fracture strain of 16%. The vacancy formation energies are much smaller for this layer in both the ferromagnetic and paramagnetic states, as discussed in the last section. Of both the magnetic states, the vacancy formation energy is even smaller for the paramagnetic state, and the ferromagnetic results discussed here could also be relevant for the paramagnetic state. Therefore, vacancies can also be key promoters of embrittlement in both the magnetic states.

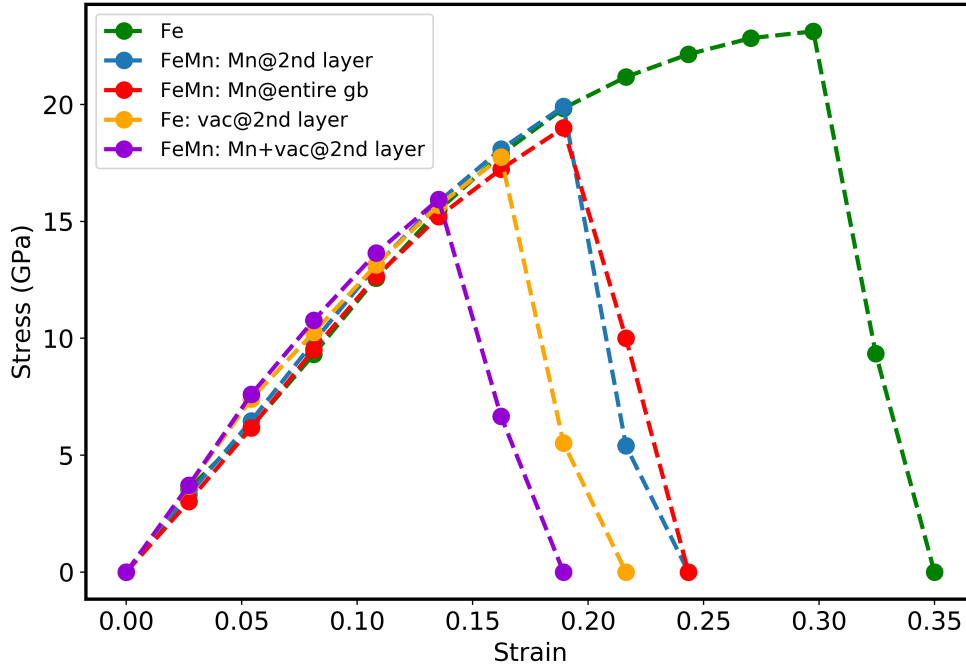


Figure 5-17: Stress-strain curve for Fe grain boundary with both Mn and vacancy in the second layer (violet dashed line), compared with the cases of a Mn atom in the second layer, Mn covering the entire grain boundary layer and vacancy in the second layer. Pure Fe case is also added for reference.

The impact of Mn-vacancy pair on the grain boundary decohesion is studied by substituting a Mn atom and creating a Fe vacancy in the layer next to the grain boundary, named as 2nd layer in Fig. 5-17. This layer is chosen since it is the most favourable for Mn segregation and vacancy formation. In the figure, the stress-strain curve corresponding to the Mn-vacancy pair is compared with the most detrimental cases with respect to Mn or vacancy that are discussed above, which are: (a) a Mn atom at site 2 in the layer next to the grain boundary, (b) Mn atoms cover entire grain boundary layer (c) a vacancy in the layer next to the grain boundary. The case of pure Fe grain boundary has also been shown for reference. From the figure, it is clear that the presence of both Mn and vacancy is highly detrimental to the grain boundary toughness, the fracture strain being 13.5%. Compared to all the discussed cases, this is the most detrimental situation. Therefore, the experimental speculations that the Mn-vacancy pairs could contribute substantially to the grain boundary fracture [24, 25] are confirmed in the present study.

5.5 Conclusions

In summary, the relaxation scheme based on SSA has been extended and applied to grain boundaries in the present chapter, thereby gaining new physical insights. Beginning with the grain boundary formation energies, a remarkable impact of magnetic disordering is seen. The reduction in grain boundary energies in the paramagnetic state is in agreement with the trends observed in the tracer diffusion experiments. The scheme is further applied to predict Mn segregation behaviour at the grain boundary, where, again, a substantial impact of magnetism is observed. Moreover, largely different segregation energies at different grain boundary sites are observed, particularly for the ferromagnetic state. The chemical complexity is increased in the next step by considering Mn-Mn interactions at and in the vicinity of the grain boundary. The segregation profile is again significantly different for the two magnetic states. The paramagnetic profile is similar to the single Mn case whereas it is much different for the ferromagnetic case. The reduced segregation drive in the paramagnetic state agrees well with the APT experiments at high temperatures. A special case, where the grain boundary exhibits paramagnetic state while the bulk is in the ferromagnetic state is revealed and discussed via mean-field considerations. This is made possible by the accurate computation of paramagnetic energies using SSA relaxations. Overall, a remarkable impact of structural-chemical-magnetic coupling on these different physical properties is observed. The vacancy formation energies are studied in the next step, and the grain boundaries are identified to be potential vacancy sinks in both the magnetic states.

The first-principles tensile tests are carried out based on the knowledge extracted from the segregation and vacancy formation studies. The extent of Mn embrittlement at different sites and different concentration is discussed. Vacancies too, are found to be highly detrimental to the grain boundary, whereas the Mn-vacancy pair is identified as the most detrimental of all the cases.

Thus, the present chapter probes, predicts, and reveals various structural, chemical, and magnetic properties of FeMn grain boundaries. The physical understandings drawn from the present chapter could be used for the theoretical and experimental engineering of grain boundaries in steels.

6 Influence of twin boundaries on magnetic domains in τ -MnAl

(The main results of the chapter have been published in - *Influence of crystalline defects on magnetic nanodomains in a rare-earth-free magnetocrystalline anisotropic alloy*. Dhanalakshmi Palanisamy, András Kovács, Omkar Hegde, Rafal E. Dunin-Borkowski, Dierk Raabe, Tilmann Hickel, and Baptiste Gault, Phys. Rev. Materials 5, 064403 (2021). The citation is given in reference [7].)

6.1 Introduction

Permanent magnets are an important class of materials used in hydro-electric industries, robotics, and electrical appliances [139] etc. As discussed in chapter 1, in general, permanent magnets form a category of "hard" magnetic materials that are hard to demagnetize. Such magnets possess large coercivity, remnant magnetization and magnetic anisotropy. In this regard, the best magnets are based on rare-earth (RE) elements [140] such as neodymium, dysprosium, cerium etc. However, as they are named, they occur in rare amount in nature and most of them are very expensive. On the other hand, Fe-based magnets are abundant and cheap, but yield low values of magnetic energy density. Therefore, low-cost magnets that are RE-free yet exhibit large coercivity and magnetic anisotropy, such as τ -MnAl, are gathering large interest in the scientific and industrial communities [28].

MnAl exhibits an $L1_0$ crystal structure that extends from the near-equal-stoichiometric composition till about 60% Mn composition, known as the τ phase. This phase is ferromagnetic and exhibits a large magnetic anisotropy along with a high magnetic energy density [35, 7]. The τ phase forms from the hexagonal ϵ phase via a massive transformation [37]. During this transformation, a large number of twin boundaries, dislocations and antiphase boundaries are formed [35]. Such defects can play a crucial part in determining the performance of magnets.

In the previous chapter, the interplay of grain boundary structure, chemistry, and magnetism had been explored in FeMn alloys. Since such interactions were remarkable, the current chap-

ter carries a similar philosophy albeit for a different system with different applications. The chapter explores the influence of twin boundary defects and their local chemical composition on the magnetic properties of τ -MnAl, using correlative theoretical and experimental studies.

The chapter is organized as follows: Sec. 6.2 discusses theoretical and experimental methods used, the results are presented and discussed in Sec. 6.3 and the conclusions are drawn in Sec. 6.4.

6.2 Computational and experimental details

6.2.1 First-principles calculations

First-principles DFT calculations are performed with the Vienna Ab-initio Simulation Package (VASP) [141]. The PBE-GGA framework [85, 48] with the PAW formalism [119, 120] is used for all DFT calculations. An energy cut-off of 500 eV is chosen along with a Monkhorst-Pack k-point mesh of $2 \times 5 \times 10$. These parameters are chosen after performing convergence tests and confirming that the resulting error contribution to the total energy is smaller than 1 meV/atom. All the calculations are performed with Methfessel-Paxton smearing [142], and a smearing width of 0.1 eV. The convergence criterion for the total energy in the electronic minimization is 10^{-6} eV and the convergence criterion for forces in ionic relaxation is 0.01 eV/Å. Supercells of 72 atoms are used for all the main results, unless otherwise specified. The equilibrium lattice parameters for the bulk $L1_0$ structure are $a = 3.88$ Å, $c = 3.50$ Å, in the face-centered tetragonal (fct) unit cell. While atomic positions and cell volumes are relaxed for all the calculations, a previously relaxed structure is considered for determining magneto-crystalline anisotropy energies (MAEs) via non-self-consistent, static calculations. A higher electronic convergence criterion of 10^{-7} eV is considered for MAE calculations. In addition, the spin-orbital coupling is switched on. Twin boundary supercells are oriented along $[11\bar{2}]$, $[111]$, $[1\bar{1}0]$ directions.

The twin boundary formation energies (*TBEs*) are evaluated as

$$TBE = \frac{E_{twin} - E_{bulk}}{2A} . \quad (6-1)$$

Here, E_{twin} is the energy of the twin supercell, E_{bulk} energy of the bulk supercell and A is the area of the twin boundary. Since the twin boundary occurs twice in the supercell because of the boundary conditions, a factor of 2 is introduced in the denominator. The solution

enthalpy (E_{SE}) is defined as

$$E_{SE} = \frac{[(E_{Mn_{55.5}Al_{44.5}} - E_{Mn_{50}Al_{50}}) - x(\mu_{Mn} - \mu_{Al})]}{x}, \quad (6-2)$$

where $E_{Mn_{55.5}Al_{44.5}}$ is the energy of the off-stoichiometric supercell (such a composition is considered in order to be consistent with the experiments), $E_{Mn_{50}Al_{50}}$ is the energy of the equal-stoichiometric supercell, μ_{Mn} and μ_{Al} are the chemical potentials of Mn and Al respectively. x is the number of atoms of Al replaced by Mn in the Al-sublattice of equal stoichiometric composition to achieve the off-stoichiometric composition. Bcc Mn and fcc Al are considered for chemical potentials. The formation energies and solution enthalpies are confirmed to be converged with respect to the supercell length, height and width by performing calculations on larger supercells with 144 atoms for both the bulk and twin. In the case of the bulk off-stoichiometric composition, the averaged energy over four different chemical configurations is considered. For the twin case, the energy is averaged over six different chemical configurations. Since the concentration of Mn in the Al-sublattice is small, the configuration space for the given supercell is not large and can be sufficiently sampled by a few configurations.

The domain wall energy (DWE) is calculated as the difference in the energies of supercells with and without the domain wall, per unit area of the domain wall. 180° domains are considered as they are found to be the most relevant domains in experiments. Specifically in the bulk, 180° domains occur along the easy axis because of the large MAE. The domain wall width is assumed to be negligible for simplification. In order to decouple the effect of the twin boundary on the DWE and the MAE from bulk contributions, the twin supercells are considered such that all the atoms are twin-like. The MAE is defined as the difference in the energy of a supercell with the magnetic moments oriented along the easy axis and the energy of a supercell with the magnetic moments oriented along the hard axis per unit volume of the system. In general, anisotropy energies are referred to as the differences in energies with the moments oriented along different axes, where the MAE is the maximum possible difference.

6.2.2 Correlative APT-TEM studies

Correlative APT-TEM studies are carried out by the experimental collaborators (Dhanalakshmi Palanisamy, Baptiste Gault) from MPIE, Düsseldorf. The experimental results are added for comparison and confirmation of the theoretical results, and are not the part of this thesis. MnAl alloy is melted and homogenized at 1373 K for 10 hours. Immediately, wa-

ter quenching is carried out, resulting in the retention of parent ϵ phase, a high-temperature phase, at room temperature. Finally, the sample is subjected to heat treatment for 2 hours at 723 K, which results in the formation of τ phase. Specimens that are shaped like needles are prepared from the micro-twin regions in the τ -phase of MnAl, in a dual beam scanning electron microscope (SEM) - focused ion-beam (FIB) instrument. These specimens are subjected to TEM and APT studies. TEM measurements are carried out with aberration-corrected Titan microscope operated at 300kV. APT measurements related to compositions at atomic-scale are performed using LEAPTM 5000 XS instrument operated with a laser pulse repetition rate of 200 kHz and energy of 40pJ.

6.2.3 Off-axis electron holography

Off-axis electron holography studies are carried out by the experimental collaborators (András Kovács, Rafał E. Dunin-Borkowski) from FZ Jülich. In these experiments, the phase change of the incident electron wave due to the magnetic field of the sample is quantitatively measured, as shown in Fig. 6-1. Consequently, a hologram is generated, which is an interference pattern formed by the superposition of a complex specimen wave with a tilted reference wave.

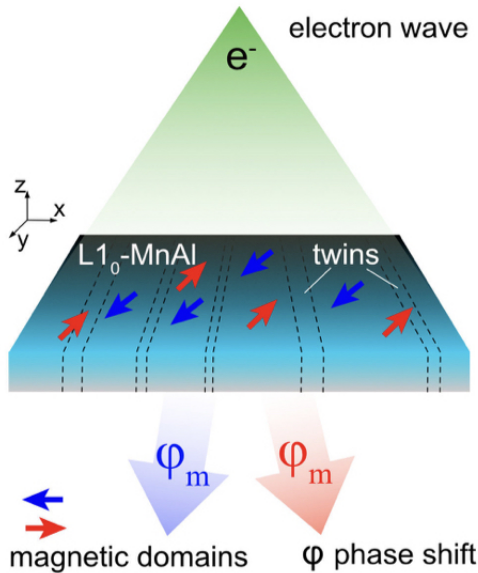


Figure 6-1: Schematic of the off-axis electron holography technique. The figure is generated by the experimental collaborators from FZ Jülich and is adapted from the collaborative work published in Phys. Rev. Materials 5, 064403 (2021) [7].

6.3 Results and discussion

The results pertaining to the interplay of structural defect (in this case twins), chemistry, and their impact on magnetic properties in τ -MnAl phase are discussed in this section. In the first part the structural and chemical properties are presented, whereas the second part showcases their relation with magnetic domains.

6.3.1 Structural and chemical properties of MnAl twin boundaries

As mentioned in the introduction, the formation of the τ -MnAl phase via a massive transformation from hexagonal ϵ phase is accompanied by the formation of a large number of twins. These twin boundaries are observed to have similar characteristics as face-centered-cubic (fcc) twin boundaries [35] and belong to the family of (111) planes. This is expected, since $L1_0$ can be regarded as an fct structure. Therefore, fct $\Sigma 3$ $[1\bar{1}0](111)$ twin boundaries are considered for the first-principles study (Fig. 6-5).

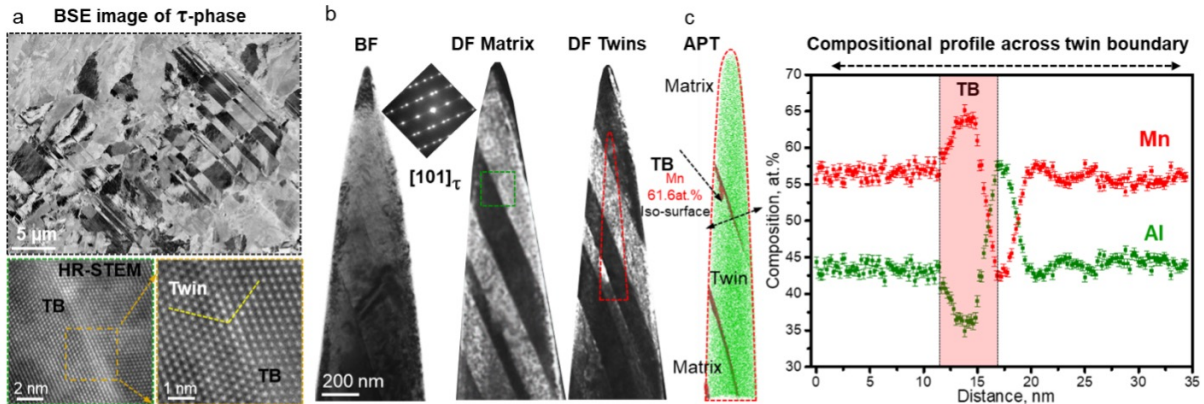


Figure 6-2: (a) BSE image of the microstructure, (b) BF- and DF-TEM images of the specimen, (c) BF-TEM image of the area considered for APT study and the APT profile revealing Mn segregation at the twin boundary. The figure is generated by the experimental collaborators from MPIE Düsseldorf and is adapted from the collaborative work published in Phys. Rev. Materials 5, 064403 (2021) [7].

The observations from backscattered electron microscopy (BSE) and correlative APT-TEM studies are presented in Fig. 6-2. The microstructure analysis through BSE (Fig. 6-2a) reveals a large number of micro-twins. The bright-field (BF) TEM images are shown in Fig. 6-2b. The electron diffraction pattern shows the reflection of (111) twin diffraction spots. The dark-field (DF) TEM images of both the matrix and the twins provides their

corresponding contrasted reflections. The area marked by the red dashed line is considered for the APT analysis. The APT result in Fig. 6-2c divulges the composition profile across the twin boundary and reveals the segregation tendency of Mn at the twin boundary. Mn enrichment raises its composition upto 63% at the twin boundary, while it is 55% in the matrix region.

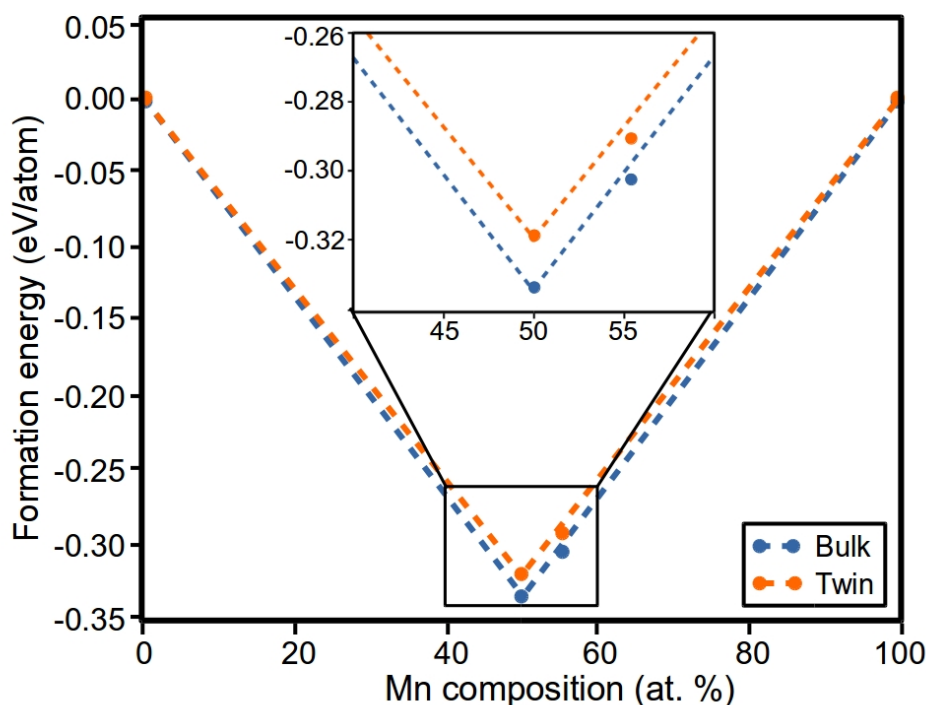


Figure 6-3: Formation energy convex hull for the bulk and twin structures of τ -MnAl as a function of Mn composition.

DFT calculations allow for an understanding of these experimental observations at the atomic scale. The DFT calculations are carried out for both the equal- and off-stoichiometric compositions, where the former is the only compound considered for the convex hull shown in Fig. 6-3. Pure elements are used as the end points of the convex hull. As seen from the figure, DFT can resolve such small energy differences with high accuracy. From the convex hull, it is evident that the formation energy points of $\text{Mn}_{55.5}\text{Al}_{44.5}$ lie below the hull for both the bulk and twin structures. This indicates that the off-stoichiometric composition is relatively stable and does not decompose in both the structures. The fundamental reason behind such a stability has been traced to the reduction of magnetic frustrations in

the Mn-sublattice by the presence of excess Mn atoms in the Al-sublattice [143]. Further, the *TBEs* for both $\text{Mn}_{55.5}\text{Al}_{44.5}$ (0.09 J/m^2) and $\text{Mn}_{50}\text{Al}_{50}$ (0.11 J/m^2) are observed to be very low, agreeing with the experimental observation of a large number (and high density) of twin boundaries in the τ phase. Finally, the solution enthalpies of the excess Mn atoms in $\text{Mn}_{55.5}\text{Al}_{44.5}$ as calculated according to Eq. (6-2) show reduced values in the presence of twin boundary (0.52 eV) as compared to the perfect bulk (0.59 eV). This observation rationalises the segregation tendency of Mn at the twin boundary as obtained from the APT studies. Thus, the correlative TEM-APT-DFT study allows for the observation and analysis of the structural and chemical interplay in τ -MnAl.

6.3.2 Magnetic domains and anisotropies

MnAl permanent magnets are known for their large coercivity and subsequent applications. Magnetic properties depend on the nucleation and pinning of magnetic domains. In this regard, the impact of twin defects on their magnetic properties is crucial to understand. The off-axis holography (described previously) provides highly resolved domain structures and domain directions. In Fig. 6-4, magnetic induction maps obtained from electron holography and their corresponding BF-TEM images are shown. In the case of the specimen without twins, magnetic domains are observed to be large in size, with a few 180° domain walls. As the density of twins increases, a plethora of remarkably fine shaped magnetic domains that have mosaic-like shape are observed. The size of these domains reduce to about 10-40 nm in the high density sample. Such domains are found to be highly stable, as a large number of them do not alter in size or directions before and after the saturation of the applied external magnetic field. These observations highlight the dramatic impact of twin boundaries on the magnetic domain properties. Consequently, the twin density can be crucial in determining the performance of τ -MnAl permanent magnets.

DFT calculations show that the excess Mn atoms in the Al-sublattice align antiferromagnetically to the Mn-sublattice atoms in both the bulk and twin regions. In particular, the moment of excess Mn atoms at the twin boundary is about $-2.5 \mu\text{B}$, whereas it is about $+2.4 \mu\text{B}$ for the atoms in the Mn-sublattice. As a result, one can conclude that the segregated Mn atoms lead to a reduction in the local magnetization in the proximity of the twin boundary. This might lead to the pinning of magnetic domain walls at the twin boundary, complying with the electron hologram observations. In other words, the reduction of local magnetization at the twin boundary pins the reversed domains and prevents them from moving across the twin boundary to the neighbouring grain, ultimately leading to the increase in the coercivity of the material. Such a pinning phenomenon has been experimentally observed in

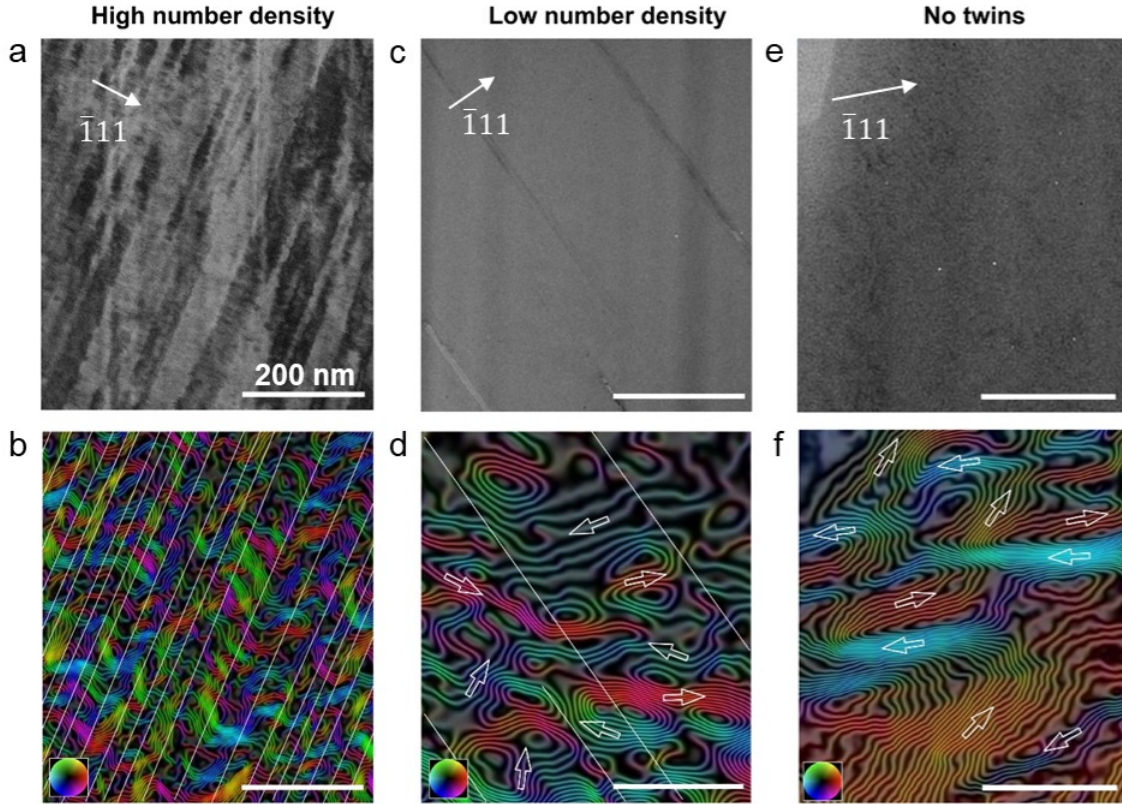


Figure 6-4: Magnetic domain structure of τ -MnAl with higher and lower densities of microtwins. (a), (c), (e) are BF TEM images and (b), (d), (f) are the corresponding projected in-plane magnetic induction maps recorded using off-axis electron holography. The figure is generated by the experimental collaborators from FZ Jülich and is adapted from the collaborative work published in *Phys. Rev. Materials* 5, 064403 (2021) [7].

Nd-Fe-B permanent magnets [144], where the segregation of non-magnetic Nd atoms at the grain boundaries resulted in the pinning of domain walls and increased coercivity. While Mn segregation could lead to domain wall pinning, it is to be noted that the pinning mechanism alone cannot explain the observation of a large number of nano-domains at the twin boundary. To understand this, the impact of twin boundaries on magnetic anisotropy energies and domain wall energies are studied.

The MAEs for the equal- and off-stoichiometric compositions in the bulk and twin phases are presented in Fig. 6-6b. Clearly, the presence of the twin boundary results in a substantial reduction of the MAE as compared to that in the bulk region. The variations due to compositional differences are not significant. The easy axis in the bulk is [001], which changes

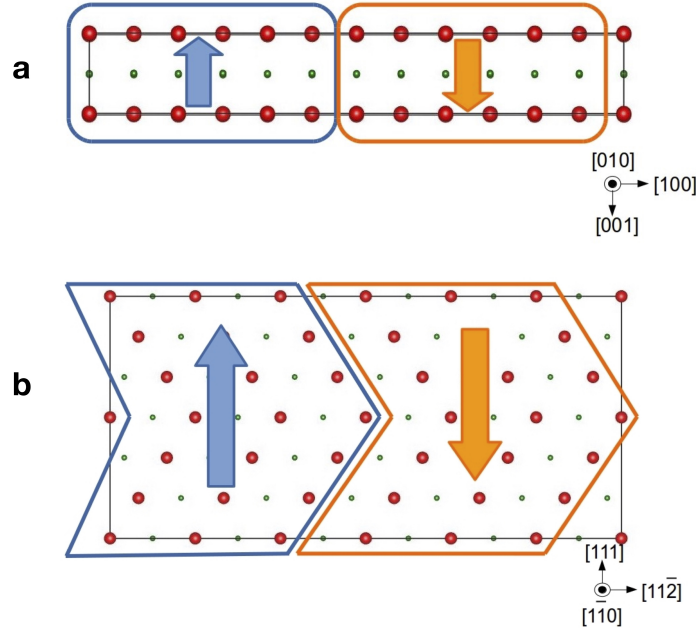


Figure 6-5: Schematic of the the bulk and twin supercells along with the domain walls considered for calculations.

to $[11\bar{2}]$ in the twin region. Besides the MAE, which is the largest difference (between the easy axis and hard axis), other anisotropy energies are substantially reduced in the vicinity of twin boundary, as shown in Tab. 6-1. Here, a few examples are taken to demonstrate that the anisotropy energies in the twin region are consistently smaller than in the bulk, since such calculations are computationally highly expensive and even more so in the case of extended defects such as twin boundaries.

Anisotropy energies (MJ/m ³)		
	Bulk	Twin
$[001] - [100]$	1.76	0.56
$[001] - [110]$	1.77	0.14
$[11\bar{2}] - [100]$	1.15	0.66
$[11\bar{2}] - [110]$	1.16	0.28

Table 6-1: Calculated anisotropy energies between different axes in the bulk and twin supercells.

Since the rotation of magnetic moments precedes the formation of domains walls, anisotropy energies are crucial to understand domain formation. The low values of anisotropy energies

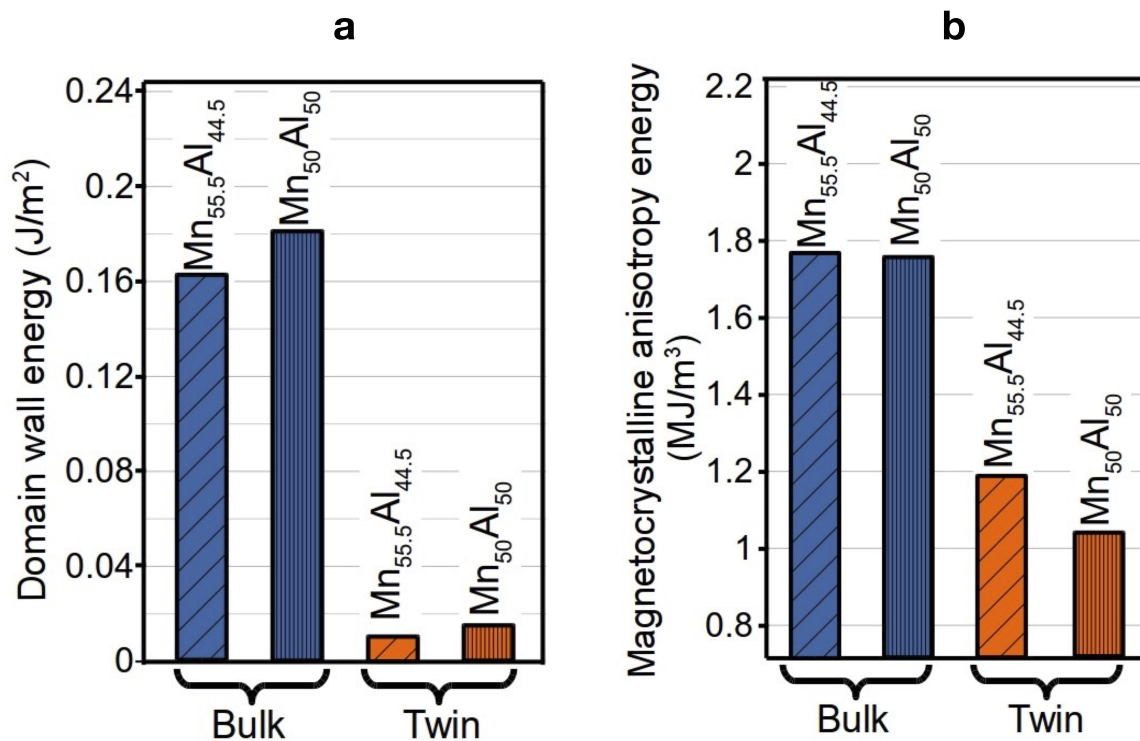


Figure 6-6: Calculated DWEs and MAEs for the equal- and off-stoichiometric compositions, in both the bulk and twin regions.

discussed above indicate that the twinning facilitates an easier formation of domain walls as compared to the bulk. While the anisotropy energies address the process that precedes the formation of domain walls, the question is also about the stability of the 180° domain walls after they are formed. For this purpose, 180° domains are created in the bulk and twin supercells, as shown in Fig. 6-5. As in the case of MAEs, the presence of twin boundaries result in a notable decrease of the DWEs compared to the bulk, as shown in Fig. 6-6a. Once again, the dependence of DWEs on structures (bulk and twin) outweigh the dependence on compositions (equal- and off-stoichiometric), where the latter is insignificant. The smaller values of DWEs in the twin supercell indicate the higher stability of the domain walls as compared to the bulk. This provides a possible understanding of the stability of domain walls observed in the electron-holography experiments. Thus, together with the anisotropy energies, domain formation energies confirm the experimental observations and corroborate the remarkable influence of the twin boundaries on the formation of magnetic domain walls in τ -MnAl.

6.4 Conclusions

Correlative studies of the structural, chemical, and magnetic properties of the technologically important class of permanent magnets, τ -MnAl, are presented in this chapter. The complexities pertaining to these properties at the atomic scale demand novel combination of the theoretical and experimental approaches. In this regard, in the first part, the knowledge from the first-principles DFT studies is compared with the APT-TEM experiments to confirm and understand structural and chemical properties. TEM experiments find a large density of twin boundaries in the off-stoichiometric τ -MnAl sample. DFT values of the twin boundary formation energies are very small, in agreement with the experiments. Further, the formation energy hull confirms the relative stability of the off-stoichiometric composition. APT composition profile across the twin boundary show an enrichment of Mn, supported by the reduction of Mn solution enthalpy in the twin region as calculated in DFT. The interactions of twin boundaries with magnetic domains are studied by off-axis electron holography experiments. The electron holograms reveal numerous finely structured magnetic domains, with a large number of 180° domain walls. The number of domains scales directly with the density of twins while their size scales inversely. DFT studies show that while the reduced magnetization could promote domain wall pinning at the twin boundary, the remarkable reduction in MAEs and DWEs provide deeper understanding of the formation and stability of the 180° domain walls.

The direct link of the defect structure and chemistry to the magnetic properties allows for the design of these magnetic materials with desired performances. The co-validation of the theoretical and experimental studies paves way for the computational prediction and design followed by experimental realisation in the future works.

7 Summary and outlook

The realms of defects and magnetism are vast in their own right, and their interplay is gaining significant relevance. This thesis aims at contributing a small portion in expanding such an area of overlap. In particular, the branch of computational materials physics concerning defect properties in magnetically disordered systems is still young, albeit challenging. We discuss our general motivations to address such challenges and to study material systems considered in the thesis, in chapter 1. More specific motives are discussed in the beginning of corresponding chapters. Further, we discuss the theoretical methods that underlie the tools adopted to achieve the results of the thesis in chapter 2. The presence of defects, such as vacancies, cause breaking of bonds and result in atomic relaxations. In this regard, we introduce a new method to account for atomic relaxations in magnetically disordered systems in chapter 3. The method is based on spin-space averaging (SSA), which considers the physical picture of rapidly varying magnetic degrees of freedom compared to the atomic degrees of freedom, i.e., the adiabatic approximation. Consequently, averaging of forces on atoms in different magnetic configurations is needed to capture the true paramagnetic state. We discuss how we bring different tools together to achieve this in the chapter. We apply the relaxation method, called as SSA relaxations, to the case of mono-vacancy in bcc Fe. The resulting relaxations and vacancy energies are found to be significantly different from those obtained from the approximative methods used in the literature, reiterating the importance of considering proper relaxations. In particular, assuming the physical limit where the time-scale for magnetic degrees of freedom are comparable with the atomic degrees of freedom leads to vacancy energies that deviate largely from the experimental values. Through these results, the adiabatic approximation is justified for vacancy in bcc Fe. Finally, the relevance of volume expansion is discussed in the chapter.

Defects in FeMn steels control various physical phenomena such as segregation, spinodal decomposition, phase transformation, fracture etc [26, 27, 23, 24, 25]. In this regard, it is pivotal to understand diffusion of Mn in bcc Fe. In particular, magnetic order-disorder transition could play decisive role in determining Mn diffusion properties. Therefore, in chapter 4, we use the SSA relaxation method to investigate and understand the impact of magnetic order/disorder on Mn diffusion in bulk Fe. To this end, we calculate Mn-vacancy binding

energies, vacancy formation energies, migration energies and activation energies in both the ferromagnetic and paramagnetic states. The migration barriers in the magnetically ordered state are more dispersed while they are more similar in the disordered state, implying that magnetic disordering dominates and reduces chemical distinctiveness. This is confirmed by studying Mn correlation factors, which show that the vacancy jumps are more random in the disordered paramagnetic state and highly correlated in the ferromagnetic state. Using the vacancy energies, the Mn and Fe diffusion coefficients, their ratios, correlation factors are extracted via the Ruch model and LeClaire's model. The self-diffusion coefficients of Fe show the prominent kink in the diffusion profile at the magnetic order-disorder transition. The kink is substantially reduced for the diffusion profile of Mn in bcc Fe. Mn diffuses very fast relative to Fe in the ferromagnetic state, as compared to the paramagnetic state. We compare our results with those of effective interaction models and tracer diffusion experiments obtained by our collaborators. Excellent agreements between theoretical and experimental results are seen, confirming the above derived physical conclusions.

Mn segregation at Fe grain boundaries are known to cause embrittlement and phase transformation. However, physical understanding of the segregation is little-known. We study grain boundaries, which are structurally more complex defects, in chapter 5. Once again, the SSA relaxations facilitate paramagnetic considerations even for grain boundaries. The ferromagnetic and paramagnetic states have very different grain boundary energies, with the latter being smaller, indicating strong magnetic coupling to the structural defect. The temperature dependence of the trend is consistent with the experimental literature. The chemical degrees of freedom are introduced by studying Mn site dependency in the context of segregation, and the results once again mark the importance of proper paramagnetic treatment. Combined with the understanding from chapter 4, where Mn was shown to diffuse much faster than Fe at low temperatures in the ferromagnetic state, the highly attractive segregation energies for the ferromagnetic state indicate that the Mn segregation to grain boundaries is both kinetically and thermodynamically favoured in the ferromagnetic state. By increasing Mn coverage in the grain boundary, Mn-Mn interactions are included. Mn segregation drive is found to be very strong in the ferromagnetic state and only slightly so in the paramagnetic state. Using the paramagnetic energies, a special case in the intermediate temperatures, where the grain boundary is in the paramagnetic state and the bulk is in the ferromagnetic state, is revealed. Overall, segregation studies show extraordinary interplay of structure, chemistry, and magnetism. Finally we bridge our physical understanding with engineering: By using knowledge from the segregation study, we discuss the degree of embrittlement caused by Mn, vacancy, and their combinations via tensile tests, the knowledge of which is crucial for "segregation engineering" at the grain boundaries.

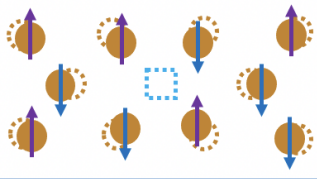
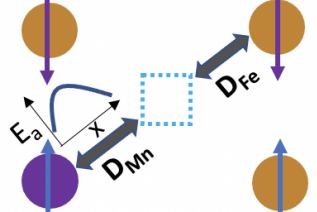
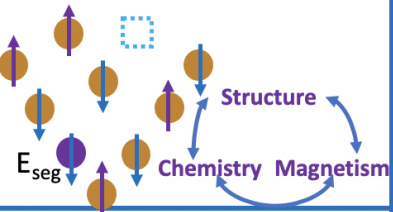
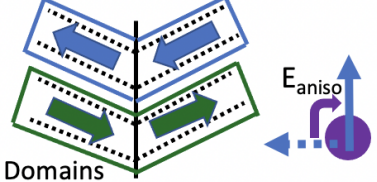
Chapter	Defect	Keywords	Schematic
III	Vacancy (in bcc Fe)	Method, magnetic disorder, relaxation, vacancy formation, migration, volume expansion	
IV	Solute-Vacancy (in bcc FeMn)	Diffusion, kinetics, solute-vacancy interaction, magnetic order-disorder transition, correlation factors	
V	Grain boundary (in bcc FeMn)	Formation, segregation, vacancy at grain boundary, magnetic disorder, structural-chemical-magnetic coupling, tensile tests	
VI	Twin boundary (in τ-MnAl)	Magnetic domains, correlative DFT-APT-Holography studies, anisotropy energies, twin boundary energies	

Figure 7-1: Summary of defect types, keywords and schematic diagrams corresponding to each result chapter in the thesis.

We consider a different system, MnAl permanent magnets, in chapter 6. The spirit of structural, chemical, and magnetic interplay is carried forward from the last chapter, but for twin boundaries in τ -MnAl. The results are presented in combination with the sophisticated experiments carried out by our collaborators. In the first part, the structural and chemical studies from theory are carried out in conjunction with the atom probe tomography (APT) experiments. APT reveals a number of Mn enriched twin boundaries in the off-stoichiometric sample. We show that the off-stoichiometric composition is indeed stable, by constructing the formation energy hull. The small values of twin boundary energies explain the large number of twin boundaries in the sample. Mn solution enthalpies are smaller in the vicinity of the twin boundary as compared to the bulk, in agreement with Mn enrichment observed in the APT studies. In the next part, we study the influence of these structural and chemical as-

pects on the magnetic properties along with the electron holography experiments performed by our collaborators. The experiments show a large number remarkably fine 180° domains at the twin boundaries, and only a few domains in the bulk. Theoretically, we explain these findings based on the domain wall energies and magnetocrystalline anisotropy energies, both of which are found to be significantly smaller in the twin region in comparison with the bulk. The small anisotropy energies mean easier rotation of magnetic moments to form the domains and the small domain wall energies indicate the high stability of 180° domains after their formation.

Thus, we learnt the above discussed findings through this thesis and try to expand the horizons of the field of magnetism in defects, albeit to a small degree. Though highly challenging, we see a few interesting opportunities through which one can further develop the methods presented in the thesis. Firstly, the vibrational contribution to the free energy [145, 146, 147] can be significant at finite temperatures and needs to be included for a more accurate description of the defect energetics in the paramagnetic state, since vibrational contributions can be pivotal in determining defect phase diagrams [148, 149]. While this needs significant methodological developments and computational efforts, the ever-increasing efficiency of modern computer clusters can make it feasible in the near future. Next, we consider the data generated in the thesis to be sufficiently accurate (in particular those concerning the paramagnetic state, since they are under-represented in the literature) to be used as input for kinetic Monte Carlo simulations. Especially, the study of diffusion phenomena in the vicinity of grain boundaries at finite temperatures would be of great interest in light of recent experimental observations of spinodal decomposition in FeMn grain boundaries [26]. Finally, the application of SSA relaxations to other industrially relevant materials would be exciting. In this regard, we have begun studying Ni_2MnGa Heusler alloys, a class of magnetic shape memory alloys known for their applications in magnetic actuators and sensors, and the first results are promising.

Bibliography

- [1] D. Raabe, D. Ponge, O. Dmitrieva, and B. Sander, “Designing ultrahigh strength steels with good ductility by combining transformation induced plasticity and martensite aging,” *Adv. Eng. Mater*, vol. 11, no. 7, pp. 547–555, 2009.
- [2] T. Hickel, B. Grabowski, F. Körmann, and J. Neugebauer, “Advancing density functional theory to finite temperatures: methods and applications in steel design,” *J. Phys. Condens. Matter*, vol. 24, no. 5, p. 053202, 2011.
- [3] O. Hegde, M. Grabowski, X. Zhang, O. Waseda, T. Hickel, C. Freysoldt, and J. Neugebauer, “Atomic relaxation around defects in magnetically disordered materials computed by atomic spin constraints within an efficient lagrange formalism,” *Phys. Rev. B*, vol. 102, p. 144101, Oct 2020.
- [4] O. Hegde, V. Kulitckii, A. Schneider, F. Soisson, T. Hickel, J. Neugebauer, G. Wilde, S. Divinski, and C.-C. Fu, “Impact of magnetic transition on mn diffusion in α -iron: Correlative state-of-the-art theoretical and experimental study,” *Phys. Rev. B*, vol. 104, no. 18, p. 184107, 2021.
- [5] Y. Iijima, K. Kimura, and K. Hirano, “Self-diffusion and isotope effect in α -iron,” *Acta Metall.*, vol. 36, p. 2811, 1988.
- [6] G. Hettich, H. Mehrer, and K. Maier *Scr. Metall.*, vol. 11, p. 795, 1977.
- [7] D. Palanisamy, A. Kovács, O. Hegde, R. E. Dunin-Borkowski, D. Raabe, T. Hickel, and B. Gault, “Influence of crystalline defects on magnetic nanodomains in a rare-earth-free magnetocrystalline anisotropic alloy,” *Phys. Rev. Materials*, vol. 5, no. 6, p. 064403, 2021.
- [8] S. Divinski, J. Geise, E. Rabkin, and C. Herzig, “Grain boundary self-diffusion in α -iron of different purity: effect of dislocation enhanced diffusion,” *Z. Metallkd.*, vol. 95, no. 10, pp. 945–952, 2004.
- [9] V. Borisov, V. Golikov, and G. Scherbedinskiy, “Relation between diffusion coefficients and grain boundary energy,” *Phys. Met. Metall*, vol. 17, pp. 881–885, 1964.

-
- [10] I. Abrikosov, A. Ponomareva, P. Steneteg, S. Barannikova, and B. Alling, “Recent progress in simulations of the paramagnetic state of magnetic materials,” *Curr. Opin. Solid State Mater. Sci.*, vol. 20, no. 2, pp. 85–106, 2016.
- [11] N. Sandberg, Z. Chang, L. Messina, P. Olsson, and P. Korzhavyi, “Modeling of the magnetic free energy of self-diffusion in bcc Fe,” *Phys. Rev. B*, vol. 92, no. 18, p. 184102, 2015.
- [12] H. Ding, V. I. Razumovskiy, and M. Asta, “Self diffusion anomaly in ferromagnetic metals: A density-functional-theory investigation of magnetically ordered and disordered Fe and Co,” *Acta Mater.*, vol. 70, pp. 130–136, 2014.
- [13] A. Ponomareva, Y. N. Gornostyrev, and I. Abrikosov, “Ab initio calculation of the solution enthalpies of substitutional and interstitial impurities in paramagnetic fcc Fe,” *Phys. Rev. B*, vol. 90, no. 1, p. 014439, 2014.
- [14] A. Ponomareva, B. Mukhamedov, and I. Abrikosov, “Theoretical modeling of interstitial carbon impurities in paramagnetic Fe-Mn alloys,” *Phys. Rev. Materials*, vol. 4, no. 2, p. 024401, 2020.
- [15] V. T. Witusiewicz, F. Sommer, and E. J. Mittemeijer, “Reevaluation of the Fe-Mn phase diagram,” *J. Phase Equil. Diff.*, vol. 25, pp. 346–354, 2004.
- [16] S. Bigdeli and M. Selleby, “A thermodynamic assessment of the binary Fe-Mn system for the third generation of calphad databases,” *Calphad*, vol. 64, pp. 185–195, 2019.
- [17] V. I. Anisimov, V. P. Antropov, A. I. Liechtenstein, V. A. Gubanov, and A. V. Postnikov, “Electronic structure and magnetic properties of 3d impurities in ferromagnetic metals,” vol. 37, p. 5598, 1988.
- [18] A. Schneider, C.-C. Fu, and C. Barreteau, “Local environment dependence of Mn magnetism in bcc iron-manganese alloys: A first-principles study,” *Phys. Rev. B*, vol. 98, p. 094426, 2018.
- [19] J. Geise and C. Herzig, “Impurity diffusion of vanadium and self-diffusion in iron,” *International Journal of Materials Research*, vol. 78, no. 4, pp. 291–294, 1987.
- [20] F. Buffington, K.-i. Hirano, and M. Cohen, “Self diffusion in iron,” *Acta Metall.*, vol. 9, no. 5, pp. 434–439, 1961.
- [21] Y. Iijima, “Diffusion in high-purity iron: Influence of magnetic transformation on diffusion,” *J. Phase Equilibria Diffus.*, vol. 26, no. 5, pp. 466–471, 2005.

- [22] Y. Iijima, K. Kimura, and K. Hirano, "Self-diffusion and isotope effect in α -iron," *Acta Metall.*, vol. 36, no. 10, pp. 2811–2820, 1988.
- [23] J. Hidalgo, C. Celada-Casero, and M. Santofimia, "Fracture mechanisms and microstructure in a medium Mn quenching and partitioning steel exhibiting macrosegregation," *Mater. Sci. Eng.*, vol. 754, pp. 766–777, 2019.
- [24] D. Raabe, M. Herbig, S. Sandlöbes, Y. Li, D. Tytko, M. Kuzmina, D. Ponge, and P.-P. Choi, "Grain boundary segregation engineering in metallic alloys: A pathway to the design of interfaces," *Curr. Opin. Solid State Mater. Sci.*, vol. 18, no. 4, pp. 253–261, 2014.
- [25] M. Kuzmina, D. Ponge, and D. Raabe, "Grain boundary segregation engineering and austenite reversion turn embrittlement into toughness: example of a 9 wt.% medium Mn steel," *Acta Mater.*, vol. 86, pp. 182–192, 2015.
- [26] A. K. Da Silva, D. Ponge, Z. Peng, G. Inden, Y. Lu, A. Breen, B. Gault, and D. Raabe, "Phase nucleation through confined spinodal fluctuations at crystal defects evidenced in Fe-Mn alloys," *Nat. Commun.*, vol. 9, no. 1, pp. 1–11, 2018.
- [27] L. Li, Z. Li, A. K. da Silva, Z. Peng, H. Zhao, B. Gault, and D. Raabe, "Segregation-driven grain boundary spinodal decomposition as a pathway for phase nucleation in a high-entropy alloy," *Acta Mater.*, vol. 178, pp. 1–9, 2019.
- [28] K. Skokov and O. Gutflisch, "Heavy rare earth free, free rare earth and rare earth free magnets - vision and reality," *Scr. Mater.*, vol. 154, pp. 289–294, 2018.
- [29] H. Fang, S. Kontos, J. Ångström, J. Cedervall, P. Svedlindh, K. Gunnarsson, and M. Sahlberg, "Directly obtained τ -phase MnAl, a high performance magnetic material for permanent magnets," *J. Solid State Chem.*, vol. 237, pp. 300–306, 2016.
- [30] A. Hornfeck and R. Edgar, "The output and optimum design of permanent magnets subjected to demagnetizing forces," *Electr. Eng.*, vol. 59, no. 12, pp. 1017–1024, 1940.
- [31] D. Crew, P. McCormick, and R. Street, "MnAl and MnAlC permanent magnets produced by mechanical alloying," *Scr. Metall. Mater.*, vol. 32, no. 3, 1995.
- [32] J. Mohapatra and J. P. Liu, "Rare-earth-free permanent magnets: the past and future," *Handb. Magn. Mater.*, vol. 27, pp. 1–57, 2018.

-
- [33] L. Pareti, F. Bolzoni, F. Leccabue, and A. Ermakov, “Magnetic anisotropy of MnAl and MnAlC permanent magnet materials,” *J. Appl. Phys.*, vol. 59, no. 11, pp. 3824–3828, 1986.
- [34] A. Chaturvedi, R. Yaqub, and I. Baker, “Microstructure and magnetic properties of bulk nanocrystalline MnAl,” *Metals*, vol. 4, no. 1, pp. 20–27, 2014.
- [35] D. Palanisamy, D. Raabe, and B. Gault, “On the compositional partitioning during phase transformation in a binary ferromagnetic MnAl alloy,” *Acta Mater.*, vol. 174, pp. 227–236, 2019.
- [36] J. Jakubovics and T. Jolly, “The effect of crystal defects on the domain structure of Mn-Al alloys,” *Physica B+ C*, vol. 86, pp. 1357–1359, 1977.
- [37] C. Yanar, J. Wiezorek, W. Soffa, and V. Radmilovic, “Massive transformation and the formation of the ferromagnetic 110 phase in manganese-aluminum-based alloys,” *Metall. Mater. Trans. A*, vol. 33, no. 8, pp. 2413–2423, 2002.
- [38] S. Bance, F. Bittner, T. G. Woodcock, L. Schultz, and T. Schrefl, “Role of twin and anti-phase defects in MnAl permanent magnets,” *Acta Mater.*, vol. 131, pp. 48–56, 2017.
- [39] J. Thielsch, F. Bittner, and T. Woodcock, “Magnetization reversal processes in hot-extruded τ -MnAl-C,” *J. Magn. Magn. Mater.*, vol. 426, pp. 25–31, 2017.
- [40] M. Born and R. Oppenheimer, “Zur quantentheorie der molekeln,” *Ann. Phys.*, vol. 389, no. 20, pp. 457–484, 1927.
- [41] D. Hartree, “Some relations between the optical spectra of different atoms of the same electronic structure. ii. aluminium-like and copper-like atoms,” in *Math. Proc. Cambridge Philos. Soc.*, vol. 23, pp. 304–326, Cambridge University Press, 1926.
- [42] V. Fock, “Näherungsmethode zur lösung des quantenmechanischen mehrkörperproblems,” *Z. Phys.*, vol. 61, no. 1-2, pp. 126–148, 1930.
- [43] L. H. Thomas, “The calculation of atomic fields,” in *Math. Proc. Cambridge Philos. Soc.*, vol. 23, pp. 542–548, Cambridge University Press, 1927.
- [44] E. Fermi, “Un metodo statistico per la determinazione di alcune priorietà dell’atome,” *Rend. Accad. Naz. Lincei*, vol. 6, no. 602-607, p. 32, 1927.

- [45] P. Hohenberg and W. Kohn, “Inhomogeneous electron gas,” *Phys. Rev.*, vol. 136, no. 3B, p. B864, 1964.
- [46] W. Kohn and L. J. Sham, “Self-consistent equations including exchange and correlation effects,” *Phys. Rev.*, vol. 140, no. 4A, p. A1133, 1965.
- [47] R. G. Parr and W. Yang, “Density-functional theory of atoms and molecules. international series of monographs on chemistry,” *Oxford University Press, New York*, vol. 3, pp. 14312–14321, 1994.
- [48] J. P. Perdew, K. Burke, and M. Ernzerhof, “Generalized gradient approximation made simple,” *Phys. Rev. Lett.*, vol. 77, no. 18, p. 3865, 1996.
- [49] J. P. Perdew, P. Ziesche, and H. Eschrig, “Electronic structure of solids’ 91,” 1991.
- [50] J. P. Perdew, S. Kurth, A. Zupan, and P. Blaha, “Accurate density functional with correct formal properties: A step beyond the generalized gradient approximation,” *Phys. Rev. Lett.*, vol. 82, no. 12, p. 2544, 1999.
- [51] V. Heine, “The pseudopotential concept,” *Solid State Phys.*, vol. 24, pp. 1–36, 1970.
- [52] P. E. Blochl, “Projector augmented-wave method,” *Phys. Rev. B*, vol. 50, p. 17953, 1994.
- [53] U. Von Barth and L. Hedin, “A local exchange-correlation potential for the spin polarized case: I,” *J. Phys. C Solid State Phys.*, vol. 5, no. 13, p. 1629, 1972.
- [54] T. Moriya, “Recent progress in the theory of itinerant electron magnetism,” *J. Magn. Magn. Mater.*, vol. 14, no. 1, pp. 1–46, 1979.
- [55] J. Hubbard, “Magnetism of iron: II,” *Phys. Rev. B*, vol. 20, no. 11, p. 4584, 1979.
- [56] H. Hasegawa, “Single-site functional-integral approach to itinerant-electron ferromagnetism,” *J. Phys. Soc. Japan*, vol. 46, no. 5, pp. 1504–1514, 1979.
- [57] B. Gyorffy, A. Pindor, J. Staunton, G. Stocks, and H. Winter, “A first-principles theory of ferromagnetic phase transitions in metals,” *J. Phys. F Met. Phys.*, vol. 15, no. 6, p. 1337, 1985.
- [58] A. Zunger, S.-H. Wei, L. Ferreira, and J. E. Bernard, “Special quasirandom structures,” *Phys. Rev. Lett.*, vol. 65, no. 3, p. 353, 1990.

- [59] F. Körmann, A. Dick, B. Grabowski, T. Hickel, and J. Neugebauer, “Atomic forces at finite magnetic temperatures: Phonons in paramagnetic iron,” *Phys. Rev. B*, vol. 85, no. 12, p. 125104, 2012.
- [60] R. J. Maurer, C. Freysoldt, A. M. Reilly, J. G. Brandenburg, O. T. Hofmann, T. Björkman, S. Lebègue, and A. Tkatchenko, “Advances in density-functional calculations for materials modeling,” *Annual Rev. Mater. Res.*, vol. 49, no. 1, p. 1, 2019.
- [61] T. Hickel, B. Grabowski, F. Körmann, and J. Neugebauer, “Advancing density functional theory to finite temperatures: methods and applications in steel design,” *J. Phys. Condens. Matter*, vol. 24, no. 5, 2012.
- [62] L.-F. Zhu, B. Grabowski, and J. Neugebauer, “Efficient approach to compute melting properties fully from ab initio with application to Cu,” *Phys. Rev. B*, vol. 96, p. 224202, Dec 2017.
- [63] F. Körmann, A. Dick, B. Grabowski, T. Hickel, and J. Neugebauer, “Atomic forces at finite magnetic temperatures: Phonons in paramagnetic iron,” *Phys. Rev. B*, vol. 85, p. 125104, Mar 2012.
- [64] F. Körmann, B. Grabowski, B. Dutta, T. Hickel, L. Mauger, B. Fultz, and J. Neugebauer, “Temperature dependent magnon-phonon coupling in bcc Fe from theory and experiment,” *Phys. Rev. Lett.*, vol. 113, p. 165503, Oct 2014.
- [65] P. Steneteg, B. Alling, and I. A. Abrikosov, “Equation of state of paramagnetic crn from ab initio molecular dynamics,” *Phys. Rev. B*, vol. 85, p. 144404, Apr 2012.
- [66] I. Stockem, A. Bergman, A. Glensk, T. Hickel, F. Körmann, B. Grabowski, J. Neugebauer, and B. Alling, “Anomalous phonon lifetime shortening in paramagnetic crn caused by spin-lattice coupling: A combined spin and ab initio molecular dynamics study,” *Phys. Rev. Lett.*, vol. 121, p. 125902, Sep 2018.
- [67] B. Dutta, F. Körmann, S. Ghosh, B. Sanyal, J. Neugebauer, and T. Hickel, “Phonons in magnetically disordered materials: Magnetic versus phononic time scales,” *Phys. Rev. B*, vol. 101, p. 094201, Mar 2020.
- [68] C. Freysoldt, B. Grabowski, T. Hickel, J. Neugebauer, G. Kresse, A. Janotti, and C. G. Van de Walle, “First-principles calculations for point defects in solids,” *Rev. Mod. Phys.*, vol. 86, pp. 253–305, Mar 2014.
- [69] A. V. Ruban and V. I. Razumovskiy, “Spin-wave method for the total energy of paramagnetic state,” *Phys. Rev. B*, vol. 85, no. 17, p. 174407, 2012.

- [70] P. Delange, T. Ayrál, S. I. Simak, M. Ferrero, O. Parcollet, S. Biermann, and L. Pourovskii, “Large effects of subtle electronic correlations on the energetics of vacancies in α -Fe,” *Phys. Rev. B*, vol. 94, p. 100102, Sep 2016.
- [71] D. Gambino and B. Alling, “Lattice relaxations in disordered Fe-based materials in the paramagnetic state from first principles,” *Phys. Rev. B*, vol. 98, p. 064105, Aug 2018.
- [72] I. Bleskov, T. Hickel, J. Neugebauer, and A. Ruban, “Impact of local magnetism on stacking fault energies: A first-principles investigation for fcc iron,” *Phys. Rev. B*, vol. 93, no. 21, 2016.
- [73] S. Lu, Q.-M. Hu, B. Johansson, and L. Vitos, “Stacking fault energies of Mn, Co and Nb alloyed austenitic stainless steels,” *Acta Mater.*, vol. 59, no. 14, pp. 5728 – 5734, 2011.
- [74] A. Schneider, C.-C. Fu, F. Soisson, and C. Barreteau, “Atomic diffusion in α -iron across the curie point: An efficient and transferable ab initio-based modeling approach,” *Phys. Rev. Letters*, vol. 124, no. 21, p. 215901, 2020.
- [75] B. Alling, T. Marten, and I. Abrikosov, “Effect of magnetic disorder and strong electron correlations on the thermodynamics of CrN,” *Phys. Rev. B*, vol. 82, no. 18, p. 184430, 2010.
- [76] A. Dick, T. Hickel, and J. Neugebauer, “The effect of disorder on the concentration-dependence of stacking fault energies in Fe_{1-x}Mn_x—a first principles study,” *Steel Res. Int.*, vol. 80, no. 9, pp. 603–608, 2009.
- [77] Y. Ikeda, A. Seko, A. Togo, and I. Tanaka, “Phonon softening in paramagnetic bcc fe and its relationship to the pressure-induced phase transition,” *Phys. Rev. B*, vol. 90, no. 13, p. 134106, 2014.
- [78] N. Mousseau and G. T. Barkema, “Traveling through potential energy landscapes of disordered materials: The activation-relaxation technique,” *Phys. Rev. E*, vol. 57, pp. 2419–2424, Feb 1998.
- [79] G. Barkema and N. Mousseau, “The activation-relaxation technique: an efficient algorithm for sampling energy landscapes,” *Comput. Mater. Sci.*, vol. 20, no. 3-4, pp. 285–292, 2001.

- [80] C. Freysoldt, “On-the-fly parameterization of internal coordinate force constants for quasi-newton geometry optimization in atomistic calculations,” *Comput. Mater. Sci.*, vol. 133, pp. 71–81, 2017.
- [81] J. Janssen, S. Surendralal, Y. Lysogorskiy, M. Todorova, T. Hickel, R. Drautz, and J. Neugebauer, “pyiron: An integrated development environment for computational materials science,” *Comput. Mater. Sci.*, vol. 163, pp. 24 – 36, 2019.
- [82] S. Boeck, C. Freysoldt, A. Dick, L. Ismer, and J. Neugebauer, “The object-oriented DFT program library S/PHI/nX,” *Comp. Phys. Comm.*, vol. 182, no. 3, p. 543, 2011.
- [83] P. E. Blöchl, “Projector augmented-wave method,” *Phys. Rev. B*, vol. 50, pp. 17953–17979, Dec 1994.
- [84] G. Kresse and D. Joubert, “From ultrasoft pseudopotentials to the projector augmented-wave method,” *Phys. Rev. B*, vol. 59, no. 3, p. 1758, 1999.
- [85] J. P. Perdew, J. A. Chevary, S. H. Vosko, K. A. Jackson, M. R. Pederson, D. J. Singh, and C. Fiolhais, “Atoms, molecules, solids, and surfaces: Applications of the generalized gradient approximation for exchange and correlation,” *Phys. Rev. B*, vol. 46, no. 11, p. 6671, 1992.
- [86] Z. S. Basinski, W. Hume-Rothery, and A. Sutton, “The lattice expansion of iron,” *Proc. Math. Phys. Eng. Sci.*, vol. 229, no. 1179, pp. 459–467, 1955.
- [87] H. Matter, J. Winter, and W. Triftshäuser, “Phase transformations and vacancy formation energies of transition metals by positron annihilation,” *Applied physics*, vol. 20, no. 2, pp. 135–140, 1979.
- [88] L. De Schepper, D. Segers, L. Dorikens-Vanpraet, M. Dorikens, G. Knuyt, L. Stals, and P. Moser, “Positron annihilation on pure and carbon-doped α -iron in thermal equilibrium,” *Phys. Rev. B*, vol. 27, no. 9, p. 5257, 1983.
- [89] L. De Schepper, G. Knuyt, and L. Stals, “The activation energy for self diffusion in ferromagnetic α -iron,” *J. Phys. Chem. Solids*, vol. 44, no. 2, pp. 171–174, 1983.
- [90] A. Le Claire, “Some comments on the mass effect in diffusion,” *Philos. Mag.*, vol. 14, no. 132, pp. 1271–1284, 1966.
- [91] J. G. Mullen, “Isotope effect in intermetallic diffusion,” *Phys. Rev.*, vol. 121, no. 6, p. 1649, 1961.

- [92] A. S. for Metals. Oak Ridge Chapter and O. R. N. Laboratory, *Diffusion in Body-Centered Cubic Metals*. American Society for Metals, 1965.
- [93] K. Maier, H. Metz, D. Herlach, and H.-E. Schaefer, “High temperature positron annihilation experiments in bcc metals,” *J. Nucl. Mater.*, vol. 69, pp. 589–592, 1978.
- [94] F. S. Buffington, K. Hirano, and M. Cohen, “Self diffusion in iron,” *Acta Metall.*, vol. 9, p. 434, 1961.
- [95] C. M. Walter and N. L. Peterson, “Isotope effect in self-diffusion in iron,” *Phys. Rev.*, vol. 178, p. 922, 1969.
- [96] D. W. James and G. M. Leak, “Self-diffusion and diffusion of cobalt in alpha and delta-iron,” *Philos. Mag.*, vol. 14, p. 701, 1966.
- [97] R. J. Borg and C. E. Birchenall, “Self-diffusion in alpha iron,” *Trans. A. I. M. E.*, vol. 218, p. 980, 1960.
- [98] J. Geise and C. Herzig, “Impurity diffusion of vanadium and self-diffusion in iron,” *Z. Metallkde.*, vol. 78, p. 291, 1987.
- [99] D. Graham and D. H. Tomlin, “Self-diffusion in iron,” *Philos. Mag.*, vol. 8, p. 1581, 1963.
- [100] J. Kucera, B. Millien, J. Ruzickova, V. Foldyna, and A. Jakobova, “Self-diffusion of iron in α -phase of iron and Fe-Cr alloys,” *Acta Metall.*, vol. 22, p. 135, 1974.
- [101] M. Luebbehusen and H. Mehrer, “Self-diffusion in α -iron: The influence of dislocations and the effect of the magnetic phase transition,” *Acta Metall. Mater.*, vol. 36, p. 2811, 1988.
- [102] G. R. Speich, J. A. Gula, and R. M. Fisher, *The electron Microprobe*. Wiley, New York, 1966.
- [103] S. J. Rothman, N. L. Peterson, C. M. Walter, and L. J. Nowicki, “The diffusion of copper in iron,” *J. Appl. Phys.*, vol. 39, p. 5041, 1968.
- [104] V. A. Lazarev and V. M. Golikov, “Diffusion of copper in iron and its alloys,” *Fiz. Metal. Metalloved.*, vol. 29, p. 598, 1970.
- [105] G. Salje and M. Feller-Knieppmeier, “The diffusion and solubility of copper in iron,” *J. Appl. Phys.*, vol. 48, p. 1833, 1977.

-
- [106] J. Kucera, B. Million, and J. Ruzickova, “Magnetic anomalies of ^{59}Fe and ^{60}Co diffusion in iron and of ^{48}V diffusion in cobalt,” *Phys. Stat. Solidi A*, vol. 96, p. 177, 1986.
- [107] S. Huang, D. L. Worthington, M. Asta, V. Ozolins, G. Gosh, and P. K. Liaw, “Calculation of impurity diffusivities in $\alpha\text{-Fe}$ using first-principles methods,” *Acta Mater.*, vol. 58, p. 1982, 2010.
- [108] H. Ding, V. I. Razumovskiy, and M. Asta, “Self diffusion anomaly in ferromagnetic metals: A density-functional-theory investigation of magnetically ordered and disordered Fe and Co,” *Acta Mater.*, vol. 70, p. 130, 2014.
- [109] N. Sandberg, Z. Chang, L. Messina, P. Olsson, and P. Korzhavyi, “Modeling of the magnetic free energy of self-diffusion in bcc Fe,” *Phys. Rev. B*, vol. 92, p. 184102, 2015.
- [110] H. Wen and C. Woo, “Quantum statistics in the spin-lattice dynamics simulation of formation and migration of mono-vacancy in bcc iron,” *J. Nucl. Mater.*, vol. 470, p. 102, 2016.
- [111] L. Messina, M. Nastar, T. Garnier, C. Domain, and P. Olsson, “Exact ab initio transport coefficients in bcc Fe- X (X= Cr, Cu, Mn, Ni, P, Si) dilute alloys,” *Phys. Rev. B*, vol. 90, no. 10, p. 104203, 2014.
- [112] C. Versteyleen, N. Van Dijk, and M. Sluiter, “First-principles analysis of solute diffusion in dilute bcc Fe-X alloys,” *Phys. rev. B*, vol. 96, no. 9, p. 094105, 2017.
- [113] L. Ruch, D. R. Stains, H. L. Yeh, and L. A. Girifalco, “Analysis of diffusion in ferromagnets,” *J. Phys. Chem. Solids*, vol. 37, p. 469, 1976.
- [114] L. Girifalco, “Vacancy concentration + diffusion in order-disorder alloys,” *J Phys. Chem. Solids*, vol. 25, no. 3, p. 323, 1964.
- [115] A. D. Le Claire, “Solute diffusion in dilute alloys,” *J. Nucl. Mater*, vol. 69, p. 70, 1978.
- [116] J. R. Manning and L. Bruner, “Diffusion kinetics for atoms in crystals,” *Am. J. Phys.*, vol. 36, no. 10, pp. 922–923, 1968.
- [117] H. Takeuchi, Y. Yogo, T. Hattori, T. Tajima, and T. Ishikawa, “High-temperature magnetization characteristics of steels,” *ISIJ Inter.*, vol. 57, no. 10, pp. 1883–1886, 2017.

- [118] S. Boeck, C. Freysoldt, A. Dick, L. Ismer, and J. Neugebauer, “The object-oriented DFT program library S/PHI/nX,” *Comput. Phys. Commun.*, vol. 182, no. 3, pp. 543–554, 2011.
- [119] P. E. Blochl, “Projector augmented-wave method,” *Phys. Rev. B*, vol. 50, p. 17953, 1994.
- [120] G. Kresse and J. Joubert, “From ultrasoft pseudopotentials to the projector augmented-wave method,” *Phys. Rev. B*, vol. 59, p. 1758, 1999.
- [121] N. Mousseau and G. Barkema, “Traveling through potential energy landscapes of disordered materials: The activation-relaxation technique,” *Phys. Rev. E*, vol. 57, no. 2, p. 2419, 1998.
- [122] G. Gottstein and L. S. Shvindlerman, *Grain boundary migration in metals: thermodynamics, kinetics, applications*. CRC press, 2009.
- [123] A. K. Da Silva, R. D. Kamachali, D. Ponge, B. Gault, J. Neugebauer, and D. Raabe, “Thermodynamics of grain boundary segregation, interfacial spinodal and their relevance for nucleation during solid-solid phase transitions,” *Acta Mater.*, vol. 168, pp. 109–120, 2019.
- [124] M. Guttman, P. Krahe, F. Abel, G. Amsel, M. Bruneaux, and C. Cohen, “Temper embrittlement and intergranular segregation of antimony: A quantitative analysis performed with the backscattering of energetic ions,” *Metall. Trans.*, vol. 5, no. 1, pp. 167–177, 1974.
- [125] Z. Yu, P. R. Cantwell, Q. Gao, D. Yin, Y. Zhang, N. Zhou, G. S. Rohrer, M. Widom, J. Luo, and M. P. Harmer, “Segregation-induced ordered superstructures at general grain boundaries in a nickel-bismuth alloy,” *Science*, vol. 358, no. 6359, pp. 97–101, 2017.
- [126] R. Kirchheim, B. Somerday, and P. Sofronis, “Chemomechanical effects on the separation of interfaces occurring during fracture with emphasis on the hydrogen-iron and hydrogen-nickel system,” *Acta Mater.*, vol. 99, pp. 87–98, 2015.
- [127] D. McLean, “Grain boundaries in metals, oxford univ,” 1957.
- [128] M. Seah and E. Hondros, “Grain boundary segregation,” *Proc. Math. Phys. Eng. Sci.*, vol. 335, no. 1601, pp. 191–212, 1973.
- [129] R. Fowler, “u. ea guggenheim: Statistical thermodynamics,” 1939.

-
- [130] M. Guttman, “The role of residuals and alloying elements in temper embrittlement,” *Philos. Trans. Royal Soc. A*, vol. 295, no. 1413, pp. 169–196, 1980.
- [131] Z. Xu, S. Tanaka, and M. Kohyama, “Grain-boundary segregation of 3d-transition metal solutes in bcc fe: ab initio local-energy and d-electron behavior analysis,” *J. Phys. Condens. Matter*, vol. 31, no. 11, p. 115001, 2019.
- [132] V. Anisimov, V. Antropov, A. Liechtenstein, V. Gubanov, and A. Postnikov, “Electronic structure and magnetic properties of 3d impurities in ferromagnetic metals,” *Phys. Rev. B*, vol. 37, no. 10, p. 5598, 1988.
- [133] Y. A. Du, L. Ismer, J. Rogal, T. Hickel, J. Neugebauer, and R. Drautz, “First-principles study on the interaction of H interstitials with grain boundaries in α - and γ -Fe,” *Phys. Rev. B*, vol. 84, no. 14, p. 144121, 2011.
- [134] D. Gupta, “Influence of solute segregation on grain-boundary energy and self-diffusion,” *Metallurgical Transactions A*, vol. 8, no. 9, pp. 1431–1438, 1977.
- [135] A. Schneider, C.-C. Fu, S. Waseda, T. Hickel, and C. Barreteau, “Ab initio based models for temperature-dependent magnetochemical interplay in bcc Fe-Mn alloys,” *Phys. Rev. B*, vol. 103, p. 024421, 2021.
- [136] H. Yamauchi, H. Watanabe, Y. Suzuki, and H. Saito, “Magnetization of α -phase Fe-Mn alloys,” *J. Phys. Soc. Japan*, vol. 36, no. 4, pp. 971–974, 1974.
- [137] K. Ito, H. Sawada, and S. Ogata, “First-principles study on the grain boundary embrittlement of bcc-Fe by Mn segregation,” *Phys. Rev. Materials*, vol. 3, no. 1, p. 013609, 2019.
- [138] E. J. McEniry, T. Hickel, and J. Neugebauer, “Ab initio simulation of hydrogen-induced decohesion in cementite-containing microstructures,” *Acta Mater.*, vol. 150, pp. 53–58, 2018.
- [139] J. Coey, “Permanent magnet applications,” *J. Magn. Magn. Mater.*, vol. 248, no. 3, pp. 441–456, 2002.
- [140] J. J. Croat, J. F. Herbst, R. W. Lee, and F. E. Pinkerton, “High-energy product Nd-Fe-B permanent magnets,” *Appl. Phys. Lett.*, vol. 44, no. 1, pp. 148–149, 1984.
- [141] G. Kresse and J. Furthmüller, “Efficient iterative schemes for ab initio total-energy calculations using a plane-wave basis set,” *Phys. Rev. B*, vol. 54, no. 16, p. 11169, 1996.

- [142] M. Methfessel and A. Paxton, “High-precision sampling for brillouin-zone integration in metals,” *Phys. Rev. B*, vol. 40, no. 6, p. 3616, 1989.
- [143] A. Edström, J. Chico, A. Jakobsson, A. Bergman, and J. Ruzs, “Electronic structure and magnetic properties of L10 binary alloys,” *Phys. Rev. B*, vol. 90, no. 1, p. 014402, 2014.
- [144] J. Liu, H. Sepehri-Amin, T. Ohkubo, K. Hioki, A. Hattori, T. Schrefl, and K. Hono, “Effect of Nd content on the microstructure and coercivity of hot-deformed Nd-Fe-B permanent magnets,” *Acta Mater.*, vol. 61, no. 14, pp. 5387–5399, 2013.
- [145] B. Grabowski, L. Ismer, T. Hickel, and J. Neugebauer, “Ab initio up to the melting point: Anharmonicity and vacancies in aluminum,” *Phys. Rev. B*, vol. 79, no. 13, p. 134106, 2009.
- [146] B. Grabowski, T. Hickel, and J. Neugebauer, “Ab initio study of the thermodynamic properties of nonmagnetic elementary fcc metals: Exchange-correlation-related error bars and chemical trends,” *Phys. Rev. B*, vol. 76, no. 2, p. 024309, 2007.
- [147] F. Körmann, A. Dick, B. Grabowski, B. Hallstedt, T. Hickel, and J. Neugebauer, “Free energy of bcc iron: Integrated ab initio derivation of vibrational, electronic, and magnetic contributions,” *Phys. Rev. B*, vol. 78, no. 3, p. 033102, 2008.
- [148] T. Frolov, D. L. Olmsted, M. Asta, and Y. Mishin, “Structural phase transformations in metallic grain boundaries,” *Nat. Commun.*, vol. 4, no. 1, pp. 1–7, 2013.
- [149] S. Korte-Kerzel, T. Hickel, L. Huber, D. Raabe, S. Sandlöbes-Haut, M. Todorova, and J. Neugebauer, “Defect phases—thermodynamics and impact on material properties,” *Int. Mater. Rev.*, pp. 1–29, 2021.

Acknowledgments

I am grateful to Prof. Dr. Jörg Neugebauer for accepting me as a PhD candidate in the CM department at MPIE and his constant support during my PhD. I have learnt immensely through his suggestions and profound ideas, and I am thankful for providing the opportunity to be a part of a wonderful group of scientists.

Dr. Tilmann Hickel, my guide and group leader, has my utmost admiration and appreciation. His decision to accept me in his group has been a fortunate one for me, both professionally and personally. I cherish our illuminating discussions and brainstorming sessions, through which he has inspired me throughout my PhD. He has been a great leader who leads by example. Thank you, Tilmann.

I sincerely thank Prof. Dr. Rossitza Penchenva for accepting me as a PhD student in the Physics department at the University of Duisburg-Essen. I also deeply appreciate PD Dr. Markus Gruner for the insightful discussions, and for teaching me SPR-KKR in particular. Along with Tilmann and Jörg, both Rossitza and Markus have kindly helped to plan my thesis through IMPRS-SurMat thesis advisory meetings.

I am lucky to have been a part of our CM department. I heartily thank all the CMs, be it former or current members, for creating a wonderfully scientific, supportive and informal atmosphere. I thank Mira for all her kind assistance regarding various administrative issues. I am grateful to Dr. Osamu (Sam) Waseda for the helpful discussions during the first year of my PhD. I appreciate Biswanath Da, Albert and Poulami for being kind and supportive office-mates. I am thankful that I could make some great friends during my PhD - Biswanath Da, Poulami Di, Sudarsan, Ankit bhai, Rama, Manoj, Preeti akka, Aashi, Halil, Poulami, Arul...

I gratefully acknowledge IMPRS-SurMat for the funding and Elke Gattermann for her administrative support. I was fortunate to be a part of the MAGIKID project, and thank all the members of the consortium for the insightful scientific discussions.

Bibliography

I am ever grateful to my Appa, Amma and Tangi for everything. My best friends, Abhishek and Varun, have greatly encouraged me throughout my PhD life. Finally, I am immensely lucky to share this incredible journey with Lekshmi.

Erklärung

Hiermit versichere ich, die vorliegende Dissertation selbstständig, ohne fremde Hilfe und ohne Benutzung anderer als den angegebenen Quellen angefertigt zu haben. Alle aus fremden Werken direkt oder indirekt übernommenen Stellen sind als solche gekennzeichnet. Die vorliegende Dissertation wurde in keinem anderen Promotionsverfahren eingereicht. Mit dieser Arbeit strebe ich die Erlangung des akademischen Grades Doktor der Naturwissenschaften (Dr. rer. nat.) an.

Datum

Omkar Gopalkrishna Hegde